MULTISCALE MODELING AND DESIGN OF MECHANOCHEMICALLY ACTIVE INTERFACES

A Dissertation

Presented to the Faculty of the Graduate School

of Cornell University

in Partial Fulfillment of the Requirements for the Degree of

Doctor of Philosophy

by

Meenakshi Sundaram, Manivannan

Aug 2017

MULTISCALE MODELING AND DESIGN OF MECHANOCHEMICALLY ACTIVE INTERFACES

Meenakshi Sundaram, Manivannan, Ph.D.

Cornell University 2017

Mechanochemically active systems experience chemical reactions when subjected to critical levels of mechanical force and have applications in self-healing and early warning systems. One approach towards developing such systems is the use of force responsive chemical groups called mechanophores that can be covalently bonded to polymeric systems. In the past decade a library of mechanophores have been developed - ones that change color, fluoresce, unveil cross-linking sites, and trigger catalysis when activated to force. Though mechanophores in bulk polymers have been extensively studied, the placement of mechanophores at interfaces has attracted little attention. Augmenting interfaces with covalently attached mechanophores has tremendous potential for damage management in polymer composites that fail through interfacial debonding. We refer to a polymer composite augmented with mechanophores as an Interfacial Mechanophore Augmented Composite (IMAC).

In this dissertation we investigate the multiscale physics of mechanophore activation in IMACs and capture design principles for IMACs. First, mechanophore activation at an interface is studied using a molecular dynamics (MD) interface model subjected to shear. Our simulations demonstrate that interfacial mechanophores activate starting with the mechanophores aligned along the direction of shear and progress to the the rest of the mechanophores. For interfacial mechanophores to activate the attachments to the substrate need

to withstand the force necessary for mechanophores to activate. Given strong attachment, mechanophore activation is primarily governed by interfacial displacements.

Next, inspired by our MD study, we connect the macroscopic stress state in an IMAC to mechanophore activation using an extensible link mechanophore model. The extensible link model mechanophore stretches with the attachment points, activating when a desired length change is achieved, and exerts negligible tractions on the underlying system. With this mechanophore model, mechanophore activation can be computed directly from the displacement fields in an IMAC near the interface. We demonstrate this model framework through the classical mechanics systems of (1) a circular filler particle in a planar polymer matrix subjected to remote loading and (2) a three dimensional IMAC with a dispersed, dilute volume fraction of spherical filler particles subjected to uniaxial loading. The interfacial debonding is governed by cohesive zone laws. Our simulations show the interplay between debonding mechanics and mechanophore activation. Mechanophore activation relative to debond depends on two crucial non-dimensional parameters - the length change required to activate relative to critical interface debond length scale and the critical interface debond stress relative to matrix Young's modulus. We compute design maps to showcase the zone where mechanophores can be expected to activate during debond. We also compute the impact of other material parameters and volume fraction of filler particles on mechanophore activation.

Lastly, we answer a fundamental question of how the force dependent rate of a mechanophore reaction is affected by the environment in which it is placed. We use a 1D transition state theory approach for the computing reaction rates, with a sinusoidal potential representing the environment superimposed on a

mechanophore double-well potential. We find that reaction rates are significantly affected by the addition of the potentials via changes in energy barriers and the creation of metastable states.

BIOGRAPHICAL SKETCH

Meenakshi Sundaram, Manivannan was born in Chennai, Tamil Nadu, India from where he graduated in 2007 with a Bachelors in Mechanical Engineering from Anna University. Then he specialized in Computational Science with a Masters from Indian Institute of Science (IISc) Bangalore, India in 2009 following which he continued to work in IISc as a researcher in areas of topology optimization, inverse problems, and finite elements. He came to Ithaca in fall of 2011 to pursue his doctoral studies in Mechanical Engineering and completed it in summer of 2017. He will be joining Intel's Defect Metrology group as a Technology Development Engineering in Portland starting September 2017. Outside of academics, Meenakshi explores Indian spirituality rooted in the principles of yoga and meditation, Indian classical music, and digital photography.

To wisdom that flows across human existence

ACKNOWLEDGEMENTS

My PhD has been a cherishable intense learning experience and I thank my thesis chair Prof. Meredith Silberstein for her valuable guidance and patience through this time. Her focused direction, positivity, and research acumen has been an inspiration. Next, I would like to thank my thesis committee members Prof. Chung-Yuen Hui and Prof. Derek Warner who offered support and direction to my thesis. I would also like to acknowledge the training in atomistic and computational modeling in Prof. Nicholas Zabaras's group for the first two years of my PhD without which I would not have found a clear directive in my PhD and in my later job search. This work would not have been possible without funding from the National Science Foundation, Sibley School of Mechanical and Aerospace Engineering, and the computational resources of Extreme Science and Engineering Discovery Environment.

My experience would not have been complete without friendships built both within and beyond the lab: Peng Chen, Jesper Kristensen, Sanjeev Rao, Nenuca Syquia, Sachi Horibata, Florio Arguillias, Kevin Luke, Yan Jian, Jeff Damian, Naigeng Chen, Suwon Bae, Simge Uzun, Pankaj Singh, Apoorva, Abhishek Shrivastava, Jiakun Liu, Duhan Zhang, Anirudh Ashok, Garima Singh, Venkatraman, Ru Wan, Priti Narayanan, and Harika Tankasala. Each one of them have in someway walked me through good and difficult times in Ithaca and I am grateful for their presence.

My family deserves a special mention here for I am indebted to them in many ways - my mother Meena, my father Manivannan, my grandmother Sulochana. Their constant nourishing love and wisdom has been a great cushion for all highs and lows of graduate school. I would also like to thank my wife Lakshmi Lakshmanan, for her patience understanding and moral support.

Lastly, I am grateful for the spiritual direction that came into my life during my PhD through my spiritual Guru his Holiness Sri Sri Ravi Shankar, the Art of Living chapter in Ithaca, and the Cornell Consciousness Club.

TABLE OF CONTENTS

Biographical Sketch . . . iii
Dedication . . . iv
Acknowledgements . . . v
Table of Contents . . . vii
List of Tables . . . viii
List of Figures . . . ix

1 Introduction **1**

2 Molecular Interfacial Mechanophore Activation **5**
2.1 Introduction . . . 5
2.2 Methods . . . 6
2.3 Results and Discussion . . . 19
2.3.1 Kinematic Model . . . 19
2.3.2 Molecular Dynamics Model . . . 21
2.4 Conclusion . . . 25

3 Continuum Modeling of Mechanophores on Debonding in Polymer Composites **27**
3.1 Introduction . . . 27
3.2 IMAC Mechanochemical Model . . . 28
3.3 Material Properties . . . 36
3.4 Results and Discussion . . . 38
3.5 Application to Uniaxial Tension of Particle Filled Composite . . . 50
3.6 Conclusion . . . 52
3.7 Appendix A: Elasticity Solutions . . . 55
3.7.1 Equibiaxial loading scenario . . . 55
3.7.2 Generic loading scenario . . . 56
3.7.3 IMAC with spherical filler particles . . . 63
3.8 Appendix B: Additional Discussion of 2D Uniaxial Results . . . 65

4 Rate of Mechanophore Reactions **71**
4.1 Introduction . . . 71
4.2 Model, Theory, and Methods . . . 72
4.2.1 Model system . . . 72
4.2.2 Theory . . . 76
4.2.3 Methods . . . 77
4.3 Results and Discussion . . . 77
4.4 Summary and Future Work . . . 84

5 Conclusion and Future Directions **86**

LIST OF TABLES

2.1 Control points for Bezier cubic spline 8
2.2 The extremal values for the cubic Bezier of the double-well and the parameters for the Morse and the Lennard-Jones potentials. . 10
2.3 MD Simulation details. 13

3.1 Property ranges for the polymer matrix, mechanophores, particle, interface, and interphase. 40
3.2 Reference composite where the filler particle is assumed rigid. . 40
3.3 Sensitivity of activation and debonding to interface cohesive law parameters demonstrated by using the reference composite with $l_{\text{na}} = 1\,\text{nm}$. 45
3.4 Properties of IMAC with spherical particles. 51
3.5 Average stress, strain, activation for critical interfacial separations. 53

4.1 Representative two bead bonded mechanophore: Mechanophore parameters, potential extrema, and force modified energy barrier 74

LIST OF FIGURES

2.1 Force modified double-well potential $V_F(\mathbf{r})$ energy curves for different forces $\mathbf{F}$ acting along the bond and $\mathbf{r}$ is varied along the double-well bond. 8

2.2 The Morse potential $V_{\text{Morse}}(\mathbf{r})$ representing the covalent mechanophore attachment in nondimensional terms, along with the half-width and the length required to break the bond. 10

2.3 Representative plot of potentials used in kinematic and MD simulations. The mechanophore double-well potential is stitched from a cubic Bezier curve (—) flanked by two Morse potentials (- -). Inset: Zoomed in view of the nonbonded interactions near the well. Note that the LJ 9-3 potential is deeper than the corresponding LJ 12-6 potential. 11

2.4 Force modified energy barriers for dissociation of the substrate attachment bond for varying depths of the Morse potential with $\alpha = 1.07$ Å^{-1}. Inset: Zoomed-in view highlighting that the barrier is comparable to thermal energy for the forces close to 1.44 nN that activates the mechanophore. 13

2.5 Substrate geometry for MD model. 13

2.6 Total energy trace for: **(a)** substrate cooling and equilibration, **(b)** interface equilibration, and **(c)** quasistatic shear equilibration. . . 16

2.7 Schematics of the two models for activation of mechanophores subjected to interfacial shear. **(a)** Kinematic model: Interface is formed by two LJ 9-3 walls with a randomly oriented coarse grained mechanophore in between. **(b)** MD model: Interface is formed by two atomistic substrates with eight randomly oriented and placed coarse grained mechanophores. 17

2.8 **(a)** Orientation defining angles for mechanophore beads. **(b)** Restriction of the elevation angle. **(c)** Random orientation of the attachment bond. 18

2.9 Results for the kinematic model with only bonded interactions. **(a)** Activation trends of mechanophores with different attachment potential depths D and $\alpha = 1.07$ Å^{-1}. Here "Inf" refers to a rigid attachment. **(b)** Orientation trends over all mechanophores and over the set of activated mechanophores when the attachments are rigid.**(c)** Dissociation trends of the mechanophores indicate that they complement the activation trends i.e., mechanophores either activate or dissociate. **(d)** The grid search over the space of the attachment potentials separates the space into two regimes — one where no mechanophores activate and one where all mechanophores activate is given sufficient interfacial displacement. 22

2.10 Results of the kinematic model with and without nonbonded (NB) interactions, and of the corresponding MD model. **(a)** Activation trends with interfacial displacement. **(b)** In the presence of NB interactions the grid search performed with the kinematic model shows a narrow band over which the transition from no activation to complete activation happens. 23
2.11 Effect of inter-substrate adhesion on mechanophore activation determined by the MD model. **(a)** The interface configuration along the XZ plane is shown. The substrates come closer and they are rougher in comparison to the case without adhesion. **(b)** The interface displacement is less than the applied boundary displacement in the presence of adhesion. **(c)** Activation trends with and without adhesion. 24

3.1 Overview of modeling framework: The displacement field including debonding for a known composite and applied stress state is used to drive a mechanochemical model based on an kinematic extensible link mechanophore concept. Mechanophore properties and placement will determine the mechanochemical response for a given displacement field. 30
3.2 The setup for a circular or spherical filler particle of within an infinite matrix subject to remote stress. Ω_m is the matrix domain, Ω_p is the particle domain, and Γ is the interface boundary. $\boldsymbol{\xi}$ represents a point on the interface Γ, $\mathbf{n}$ the normal at that point and $\mathbf{r}$ represents an arbitrary position vector in the system. 32
3.3 Modeling details. (a) Representative IMAC studied. (b) The nonlinear interface cohesive law augmented to inhibit surface penetration. (c) Illustration of the mechanophore length scales. (d) The allowable orientations for mechanophore placement. 34
3.4 Equibiaxial analysis for an IMAC with a rigid particle and no interphase: (a) Mechanics of interfacial debonding as function of increasing load. (b) The expectation of mechanophore activation with respect to increasing load for four mechanophore choices. (c) Mechanophore orientations that activate at that remote load. (d) Activation map identifying regimes where mechanophore activation is expected to complete prior to debond, occur during debond, and start after debond, shown for the reference composite with mechanophores of $L_{\text{na}} = 4/3$ and varying $\Sigma_{\max}$. Uniaxial bound for the same IMAC also shown. 42

3.5 The effect of an interphase: (a) The debonding mechanics of the reference composite (Table 3.2) are compared with two otherwise equivalent composites that have a $10\,$nm interphase, one stiff and one compliant relative to the matrix. Inset shows a zoomed in view of the radial interfacial separation prior to debond for all the composites. (b) Mechanophores with $L_{na} = 4/3$ are used to demonstrate the possible impact of the interphase on activation. Inset shows a zoomed in view of activation trends of the mechanophore with $\Delta L = 0.2$. (c) Activation map shown for all the composites with mechanophores of $L_{\text{na}} = 4/3$ and varying $\Sigma_{\max}$. 48
3.6 Example of how the debonding mechanics and activation trends depend on filler particle compliance. The IMACs have the following properties: E_m =10 GPa, $\nu_m = \nu_p = 0.3$, r_p =10 nm, $\sigma_{\max}$ =5 GPa, δ =0.75 nm, $L_{\text{na}} = 4/3$, $\Delta L = 0.8$, and $r_p - r_a$ =0.1 nm. 49
3.7 Effect of volume fraction on well dispersed rigid spherical particle filled IMAC's under uniaxial tension: (a) stress-strain response, and (b) activation response as a function of strain. 53
3.8 Geometric terms for the Greens functions $\mathbf{G}_m, \mathbf{G}_p$. 67
3.9 The allowable orientations for mechanophores placement. 67
3.10 Net interfacial separations $[D]$ and mechanophore activation $\mathcal{E}(\theta)$ considered for the reference composite subjected to different uniaxial loads. (a) $[D]$ for interface with no-slip condition. (c) $[D]$ for interface with full-slip condition. (b) $\mathcal{E}(\theta)$ for interface with no-slip condition with mechanophores of $L_{\text{na}} = 4/3$ and $\Delta L = 0.2$. (d) $\mathcal{E}(\theta)$ for the interface with full-slip condition with mechanophores of $L_{\text{na}} = 4/3$ and $\Delta L = 0.2$. (e) $\mathcal{E}(\theta)$ for the interface with full-slip condition with mechanophores of $L_{\text{na}} = 4/3$ and $\Delta L = 2.0$. 68
3.11 Influence of stress state on mechanophore selection. (a) Activation map for uniaxial loading with full-slip and no-slip interface conditions compared to the activation map for the equibiaxial load case. (b) For the case of uniaxial loading with full-slip the activation map is overlayed with the angle at which mechanophore activation is expected to start. 70

4.1 The model system of 1D mechanophore moving activating through an atomic lattice. 74
4.2 Representative mechanophore's force modified double-well potential 75
4.3 Illustrative examples of the impact that the phase of the lattice potential can have on the rate of the mechanochemical reaction. All the lattice potentials used here have $A = 10$kcal/mol, $\tau = 3$Å. 81

4.4 Illustrative examples showing impact of period of the lattice potential: (a) Force modified potential energy surfaces.(b) Reaction rate as function of the bond distance. The minimum of each graph represents the rate limiting step and is considered as the rate of the reaction. (c) The rate of the reaction as a function of the applied force. 82
4.5 Illustrative examples showing impact of amplitude of the lattice potential: (a) Force modified potential energy surfaces. (b) Rate of the reaction as a function of the applied force. 83

CHAPTER 1

INTRODUCTION

The coupling of mechanical forces and chemical reactions has potential for the development of new multifunctional materials and is the recent focus of the field of mechanochemistry [40]. The governing principle for mechanochemical systems is mechanical input performs work to lower the energy barrier for a particular chemical reaction. One popular modus for realizing force responsive chemistry in polymeric materials is through the covalent incorporation of force triggered chemical moieties called mechanophores. A library of mechanophores geared towards damage management applications such as self-reporting and self-healing polymeric materials have been created in the past decade. Fluorescent [10, 5, 82, 57, 42, 44], color changing [64, 26, 69, 80], and chemiluminescent [6] mechanophores are promising for reporting applications. Catalyst unveiling [62, 27, 18], grafting site unveiling [67, 90], and small molecule releasing [11, 33, 55] mechanophores are promising for self-healing. These mechanophores have been shown to work in a variety of polymers (e.g. silicone [16], polymethylmethacrylate [10], polyurethane [34], and epoxy [58]).

While mechanophores in bulk polymers are well studied experimentally and theoretically, mechanophores at interfaces are relatively uncharted and are the primary interest of our work. Augmenting interfaces motivated as an approach to damage management of the ubiquitous polymer composites that fail through interfacial debonding. We believe that the interface holds potential for mechanophore augmentation as the strains during debonding are localized at the interface in contrast to the bulk polymer where strain preceding damage is distributed throughout the bulk. We refer to such systems as Interfacial

Mechanophore Augmented Composites (IMAC).

To the best of our knowledge, the only experimental realizations of IMACs are epoxy matrix composites synthesized by the Bruns group [49, 46] and the Gilman group [85]. The Bruns group immobilized enhanced yellow fluorescent protein mechanophores at the interface between epoxy resin and glass/carbon fibers and demonstrated the loss of fluorescence due to debonding induced protein unfolding. The Gilman group covalently attached Rhodamine spirolactam, a mechanophore that fluoresces on activation, between silk fiber and an epoxy matrix demonstrated its activation during uniaxial loading along the fiber direction. Moore's group took steps towards an IMAC by grafting anthracene cycloadduct mechanophores at the interface between polymethacrylate and silica nanoparticles, however the particles were characterized only in solution[39, 41]. In a system similar to an IMAC, Otsuka's group studied the activation of diarylbibenzofuranone (DABBF) mechanophores contained within rigid silica networks that are introduced as hard domains inside the relatively soft poly (butyl acrylate) (PBA) matrix [32] . Although the DABBF mechanophores are distributed throughout the silica domains, the authors suggest that mechanical loading primarily activates mechanophores located at the silica/PBA interface. In order for IMACs to reach their potential, we need a framework for understanding the governing physics.

A model for a mechanochemical system inherently has to bridge two scales to connect a macroscopic observable such as displacement or stress state with the molecular concentration of mechanophores activated. In bulk polymers with mechanophores, models have connected the macroscopic observable to the force felt by the mechanophore and in turn computed the rate of the

mechanophore reactions and concentration of activated mechanophores using a kinetics approach [71, 72, 81, 73]. Similarly for an IMAC we present how the two scales can be bridged in Chapters 2 and 3.

In Chapter 2 we study the molecular scale by constructing two models: a molecular dynamics (MD) idealized interface system with covalently bonded idealized mechanophores subjected to shear and an explanatory kinematic model. In both the models, the mechanophore is idealized as a bonded two bead system undergoing a bond length extension reaction governed by a double-well potential. Relative to the MD model, the kinematic model carries simpler assumptions and the similarities and differences in the results help elucidate the governing physics. First we study the progress of mechanophore activation with shear and present the evolution of mechanophore orientation with deformation. Next, we discuss the impact of mechanophore attachment strength on mechanophore activation. We observe that if the attachment is sufficiently strong then mechanophore activation is governed by the relative displacement of the attachment points on either side of the interface. We also discuss the impact of other effects such as mechanophore-substrate cohesive interactions and substrate-substrate adhesive interactions.

In Chapter 3 we present a framework to connect the macroscopic stress state to the molecular level mechanophore activation at a debonding interface in an IMAC. Taking inspiration from work in Chapter 2 we simplify the mechanophore to an extensible link connected across the interface. The end points of the extensible link deform with the underlying system without exerting any traction on the system. We showcase this framework in two classical mechanics models: a circular particle in an infinite planar matrix and a polymer

composite with a dilute disperse set of spherical particles. The interface in both the models is governed by a cohesive zone law. The interplay between debonding mechanics and mechanophore activation is elucidated with particular focus on whether mechanophore activation relative to debonding damage occurs over a zone that is relevant for reporting or healing. The impact of different material parameters are also discussed and guidelines for mechanophore choice is also provided.

In Chapter 4 we take a closer look at a how mechanophore reaction rates are affected by the environment when the mechanophore is subjected to force. This question is studied from a fundamental statistical thermodynamic view point of the rate of chemical reactions. The mechanophore is modeled through a one-dimensional double-well potential and the environmental interactions are represented by a sinusoidal potential interactions. We describe the detailed impact of the various parameters of this representative system on modifications of mechanophore reaction rates. Lastly, we summarize the crucial results of this dissertation in Chapter 5 and discuss possible future directions that this work can be taken towards.

CHAPTER 2

MOLECULAR INTERFACIAL MECHANOPHORE ACTIVATION

2.1 Introduction

Mechanophore activation at a solid interface is a process dependent on the transmission of the macroscopic force to the mechanophore attachment points, and the interaction between the mechanophore and the substrates, and the interactions between the mechanophores. Amidst this complexity, we can choose to model a specific mechanophore-interface system and evaluate mechanophore response to macroscopic loading or in contrast a representative mechanophore model can be bonded at an ideal interface where the impact of different interactions can be evaluated. We choose the latter approach with an intent to ascertain general design guidelines.

An interface with a non-interacting set of mechanophores subjected to shear loading is considered. Such a scenario represents an interface with a sparsely dispersed population of mechanophores. We develop both a kinematic model and molecular dynamics (MD) model with coarse grained mechanophores and representative substrates. These models are used to interrogate the percentage of mechanophores activated as a function of interfacial displacement for different degrees of interactions between the mechanophore and substrate. Furthermore we examine how the presence of ambient temperature and adhesive interfacial conditions affect activation.

2.2 Methods

To build a model that captures mechanophore activation due to interfacial shear, we begin with a representative mechanophore and its interactions with a substrate. The mechanophore is simplified to two coarse grained beads bonded together. The bond potential is a double-well potential that models a reversible isomerization reaction with bond length change. This 1D potential model inspired by first principle steered molecular dynamics studies of mechanophores [60, 10], assumes that the entire reaction can be mapped onto a single reaction coordinate and that the force directed chemical reaction takes this same reaction pathway [68].

The double-well potential (Fig. 2.3) is constructed in two steps: (1) a Bezier cubic spline forming the wells of the double-well potential (2) two Morse potentials (Eq. 2.2) forming the repulsive and attractive portions either side of the constructed spline such that the second derivative is continuous with the Bezier splines. The control points of the Bezier curve are given in Table. 2.1 and the parameters for the stitched Morse potentials are given in Table. 2.2. The values were chosen to obtain extremal energy values (Table 2.2) in the range of those from quantum mechanical calculations of the mechanophore spiropyran [10]. A mechanophore is termed open (activated) if the bond length is greater than the position of the second potential minima and is termed closed otherwise.

This double-well model potential captures the basic physics seen across mechanophores: with applied force the energy barrier for the forward reaction is lowered and the energy barrier for the reverse reaction is increased. This is seen in plots of the force modified potential V_F in Fig. 2.1. The force modified

potential at point $\mathbf{r}$ is obtained by

$$V_F(\mathbf{r}) = V(\mathbf{r}) - \mathbf{F} \cdot (\mathbf{r} - \mathbf{r_0}) \tag{2.1}$$

which is the difference between the potential $V(\mathbf{r})$ and the work done by the force $\mathbf{F}$ in displacing the system. Here, r_0 is a reference point where no work is considered done.

Each bead of the mechanophore is covalently bonded to a substrate. The covalent substrate attachment is modeled with a Morse potential that captures the anharmonicities of the bond away from equilibrium [52] and the dissociation of the bond [19] with a finite energy. The Morse potential V^{Morse} as a function of bond length r is

$$V^{\text{Morse}} = D\left[e^{-2\alpha(r-r_0)} - 2e^{-\alpha(r-r_0)}\right] \tag{2.2}$$

where r_0 is the equilibrium bond length at absolute 0, D is the energy required to break the bond, and α is inversely proportional to the half-width of the potential well (see Fig. 2.2). The bond stiffness (k^{Morse}) of the bond at r_0 is directly related to α and D:

$$k^{\text{Morse}} = 2\alpha^2 D. \tag{2.3}$$

The half-width $w_{1/2}^{\text{Morse}}$ is defined as the distance from the equilibrium point r_0 at which the applied force dV^{Morse}/dr is maximum ($F_{\text{max}}^{\text{Morse}}$). The maximum force and half-width are related to the Morse potential parameters by:

$$F_{\text{max}}^{\text{Morse}} = \frac{\alpha D}{2} \tag{2.4}$$

$$w_{1/2}^{\text{Morse}} = \frac{\ln(2)}{\alpha}. \tag{2.5}$$

For the interpretation of results, we define a finite bond break off point $r_{\text{break}}^{\text{Morse}}$:

$$r_{\text{break}}^{\text{Morse}} = r_0 + 3w_{1/2}^{\text{Morse}}. \tag{2.6}$$

Table. 2.1. Control points for Bezier cubic spline

Distance (Å)	4	4.5	6	9	10	11.5	12.5
Potential (kcal/mol)	-10	-30	-60	-52	-30	0	0

Distance (Å)	12.6	13.5	15	17
Potential (kcal/mol)	-58	-55	-45	-25

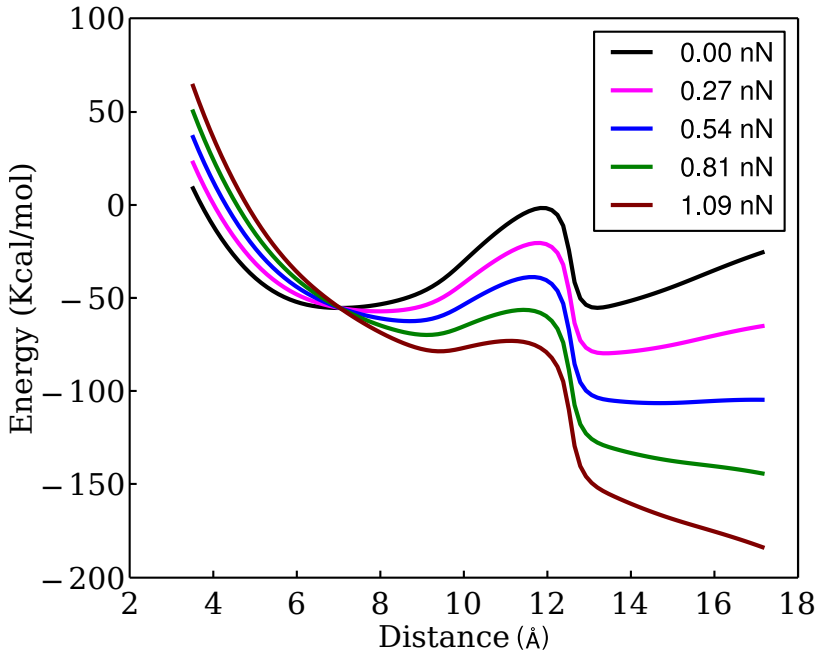

Fig. 2.1. Force modified double-well potential $V_F(\mathbf{r})$ energy curves for different forces $\mathbf{F}$ acting along the bond and $\mathbf{r}$ is varied along the double-well bond.

A mechanophore is termed detached if one of the attachment bonds extend beyond $r_{\text{break}}^{\text{Morse}}$. The ranges of attachment bond parameters used in this study are given in Table 2.2.

The idealized substrates can interact with each other and with the mechanophore beads through nonbonded interactions. The nonbonded interactions are modeled with Lennard-Jones (LJ) potentials (Fig. 2.3) — in the molecular dynamics model we use an LJ 12-6 potential for each particle, in the kinematic model we use an LJ 9-3 potential [48] which is an integration of the LJ 12-6 over the substrate. These LJ potentials are given by:

$$V^{\text{LJ } 12-6} = 4\epsilon \left[\left(\frac{\sigma}{r}\right)^{12} - \left(\frac{\sigma}{r}\right)^{6} \right] \tag{2.7}$$

$$V^{\text{LJ } 9-3} = \frac{2}{3}\pi\epsilon n\sigma^3 \left[\frac{2}{15}\left(\frac{\sigma}{z}\right)^{9} - \left(\frac{\sigma}{z}\right)^{3} \right] \tag{2.8}$$

where ϵ is the depth of the potential, σ is the length scale associated with the potential, n is the number density of the substrate, and r and z are the distances from the substrate particle and the substrate plane respectively. These parameter values are listed in Table 2.2.

The kinematic model is a potential energy minimization based analysis developed here to study the effect of interfacial shear on mechanophore activation. We lump each substrate forming a side of the interface into a rigid wall. The walls are positioned 4.71 Å apart and a mechanophore is placed in a particular orientation between the substrates. Each mechanophore bead is bonded to a point on the closer wall at the equilibrium attachment bond length. A detailed discussion of the manner in which mechanophore orientation and attachment is setup will be discussed after presenting both the models. The walls are tangentially displaced in 400 equally spaced steps until the maximum distance necessary to either activate or detach the mechanophore system. At each

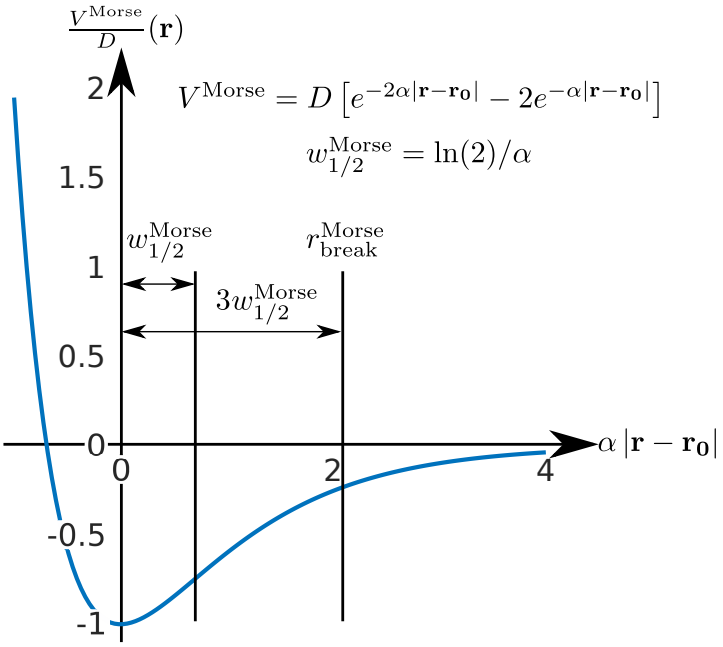

Fig. 2.2. The Morse potential $V_{\text{Morse}}(\mathbf{r})$ representing the covalent mechanophore attachment in nondimensional terms, along with the half-width and the length required to break the bond.

Table. 2.2. The extremal values for the cubic Bezier of the double-well and the parameters for the Morse and the Lennard-Jones potentials.

Double-well cubic Bezier

	Minima 1	Minima 2	Maxima
Distance (Å)	7.03	13.19	11.89
Potential (kcal/mol)	-55.37	-55.30	-1.69

Morse potentials

	Double-well		Attachment
D (kcal/mol)	61.03	50.79	$[8, 140]$
α (Å^{-1})	0.17	0.36	$[0.2, 1.4]$
r_0 (Å)	7.69	13.73	4.0
Range (Å)	$(0, 4.67)$	$(15.08, \infty)$	–

Lennard-Jones potentials

	Substrate-mechanophore	Intra-substrate	Inter-substrate
ϵ (kcal/mol)	1.23	12.31	6.16
σ (Å)	3.12	2.57	5.14
n (Å^{-3})	0.06	0.06	–

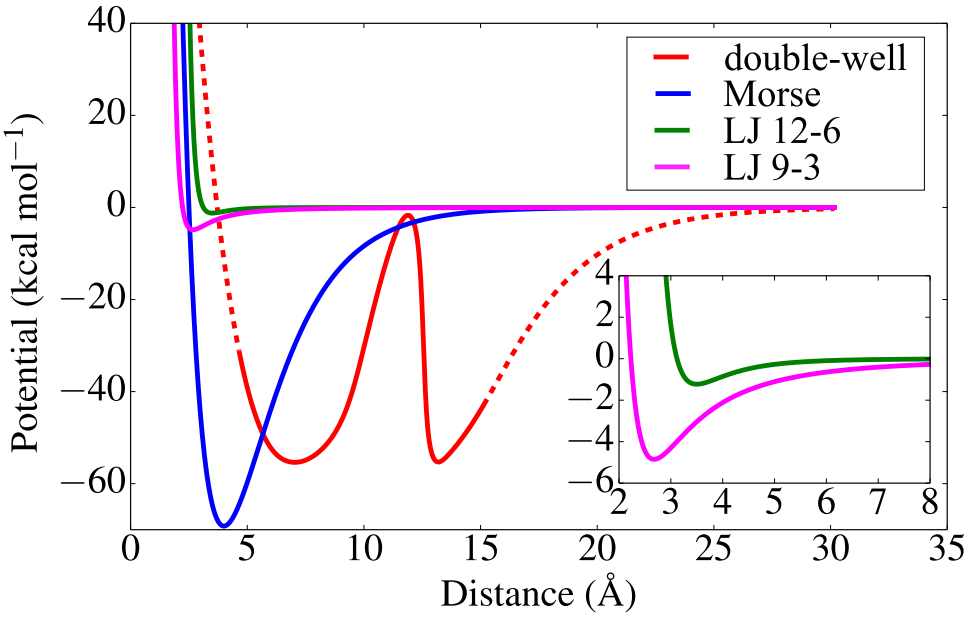

Fig. 2.3. Representative plot of potentials used in kinematic and MD simulations. The mechanophore double-well potential is stitched from a cubic Bezier curve (—) flanked by two Morse potentials (- -). Inset: Zoomed in view of the nonbonded interactions near the well. Note that the LJ 9-3 potential is deeper than the corresponding LJ 12-6 potential.

step the potential energy, comprised of bonded attachments, nonbonded interactions, and the mechanophore double-well bond, is minimized. A single result is comprised of an average over 128 uniformly distributed mechanophore orientations.

An MD model is developed in LAMMPS [63] to study the impact of discrete substrate particles and intersubstrate interaction at room temperature on mechanophore activation. Though computationally expensive the MD approach can capture effects such as adhesion, substrate elasticity, and thermal perturbations. The energy barriers for the bonds are high relative to thermal energy from room temperature, but the force applied by the shear interface displacement performs work on the bonds and reduces the barrier to the regime for which thermal effects can be influential (Fig. 2.4).

In the MD model each substrate consists of Lennard-Jones particles arranged in a face centered cubic (FCC) lattice. The LJ parameters are set to gold [88] (Table 2.2). The simulation box is periodic in $\mathbb{X}$ and $\mathbb{Y}$ and with an LJ 9-3 wall adjacent and parallel to one $\mathbb{X} - \mathbb{Y}$ face emulating bulk and vacuum on the opposite face creating a free surface. The $\langle 111 \rangle$ direction of the FCC crystal is aligned with the $\mathbb{Z}$-axis. Each substrate is approximately 80 Å wide in the $\mathbb{X}$- and $\mathbb{Y}$- directions and approximately 15 Å deep in the $\mathbb{Z}$-direction. Care must be taken to slightly adjust the $\mathbb{X}$, $\mathbb{Y}$, and $\mathbb{Z}$ boundaries to reflect the periodic continuation of the crystal, and the equilibrium position of the LJ 9-3 wall to avoid inducing edge dislocations during equilibration (Fig. 2.5).

The substrate equilibration starts with potential energy minimization, followed by step cooling in 10 equally spaced temperature stages from 1000 K to 300 K. For each stage we equilibrate at stage temperature using Noose Hoover

Table. 2.3. MD Simulation details.

Gold mass	196.97 amu
Mechanophore bead mass	196.97 amu
Timestep	1 fs
Substrate potential cutoff	7.22 Å
Substrate-mechanophore potential cutoff	8.75 Å
NVT/NPT dynamics	Noose Hoover thermostat/barostat
Total energy convergence requirement	Standard deviation $\leq$ 0.2 % Mean

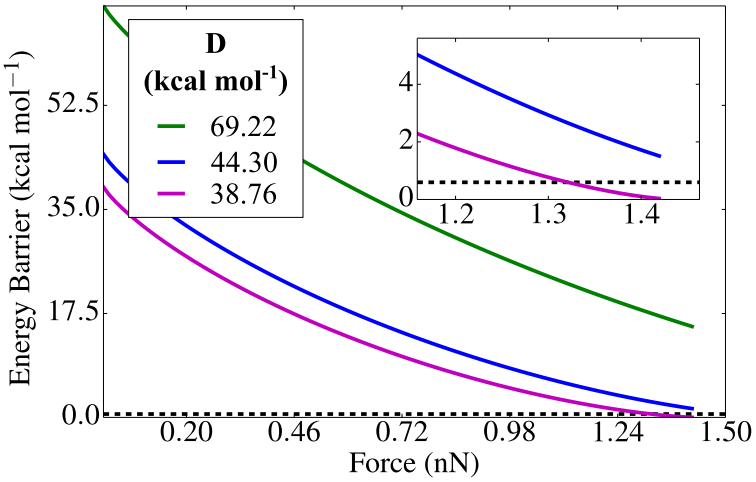

Fig. 2.4. Force modified energy barriers for dissociation of the substrate attachment bond for varying depths of the Morse potential with $\alpha = 1.07$ Å^{-1}. Inset: Zoomed-in view highlighting that the barrier is comparable to thermal energy for the forces close to 1.44 nN that activates the mechanophore.

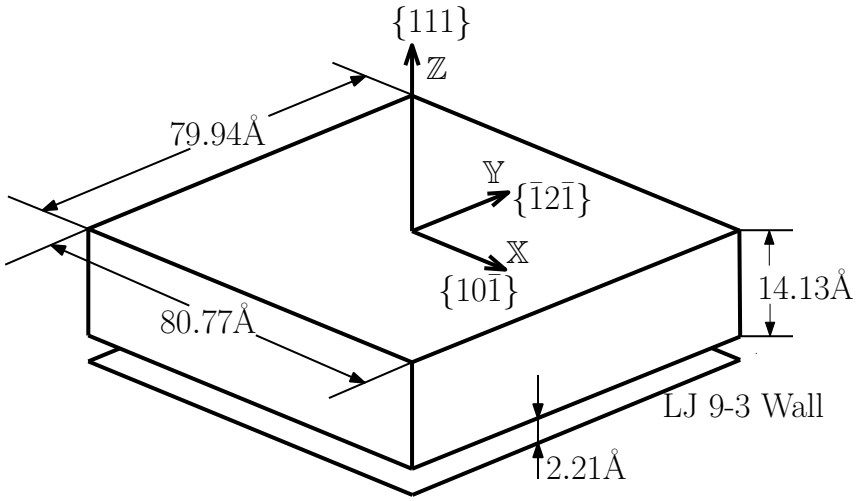

Fig. 2.5. Substrate geometry for MD model.

NPT dynamics (a statistical ensemble at which number of particles, pressure, and temperature are kept constant) at 1 atm for 40000 steps with 100 fs damping factor and then cool to the next lower temperature stage in 10000 steps with 1000 fs damping factor. The total energy trace for the NPT equilibration steps is shown in Fig. 2.6a.

Two substrate snapshots 20000 timesteps apart in the final substrate equilibration MD run at 300 K are assembled such that the free surfaces previously exposed to vacuum form the interface (Fig. 2.7b). They are separated by 4.71 Å (twice the distance between two $\{111\}$ substrate atomic layers) and the entire system is flanked by LJ 9-3 walls that emulate bulk substrates. The substrates interact through an LJ 12-6 potential (Table 2.2) that was turned on and off to study effects of adhesion between the substrates. We randomly place and orient 8 mechanophores such that the centre of mass of mechanophores are at least 14 Å apart. Each mechanophore bead is attached to the nearest substrate atom. In the cases for which adhesion is turned on, the interface is equilibrated after the substrates are assembled but prior to the insertion of mechanophores (for the cases without adhesion this equilibration would be redundant since the substrates do not interact). The interface equilibration begins with a potential energy minimization, followed by an Noose Hoover NVT (a statistical ensemble at which number of particles , volume, and temperature are kept constant) equilibration run for 40000 timesteps with a damping factor of 100 timesteps. The total energy trace is shown in Fig. 2.6b.

Quasistatic shear is simulated by displacing only a single atom thick layer on the bulk end of each substrate in opposite directions along the x-axis by a finite distance. This approach of imparting shear allows the rest of the substrate

to reconfigure and provides the mechanophore beads time to also adjust. The quasistatic shear is done in 40 stages where each stage starts with a displacement of 0.45 Å on the last layer of atoms close to the bulk end. The system, barring the displaced layers, are equilibrated at 300 K in the NVT ensemble for 10000 steps. The mechanophore attachment bonds or the double-well bond, are set to break when the bond length extends beyond three times the halfwidth of the Morse potential or the flanking Morse potential respectively. A representative total energy trace is shown in Fig. 2.6c for one stage. We present results for each shear increment by burning-in the first 3000 steps and averaging out observations such as bond length over the remaining 7000 steps of a simulation and over 25 independent simulations. For all the MD simulations refer to Table 2.3 for details of mass, timestep, cutoff, and convergence criterion used.

The mechanophore orientations in both the analytical model and the MD model are sampled within the range found by the geometric constraint that both mechanophore beads must be placed between the substrate. If the distance between the substrates is d_{int}, and the equilibrium distance between the mechanophore beads when the mechanophore is closed is denoted by $b_{\text{eq-cl}}$, we can find the range of mechanophore orientations governed by the azimuthal angle ϕ and the elevation angle θ (see Figs. 2.8a, 2.8b) as

$$\theta \in \begin{cases} \left[0, \sin^{-1}\left(\frac{d_{\text{int}}}{b_{\text{eq-cl}}}\right)\right] & b_{\text{eq-cl}} > d_{\text{int}} \\ [0, 2\pi] & b_{\text{eq-cl}} \leq d_{\text{int}} \end{cases} \tag{2.9}$$

$$\phi \in [0, 2\pi] \quad . \tag{2.10}$$

In the analytical model we first orient the mechanophore beads about the central axis and subsequently take each bead and compute its vertical distance from the nearest substrate point $(d_{\text{me-sub}})$. Next we choose a direction along the

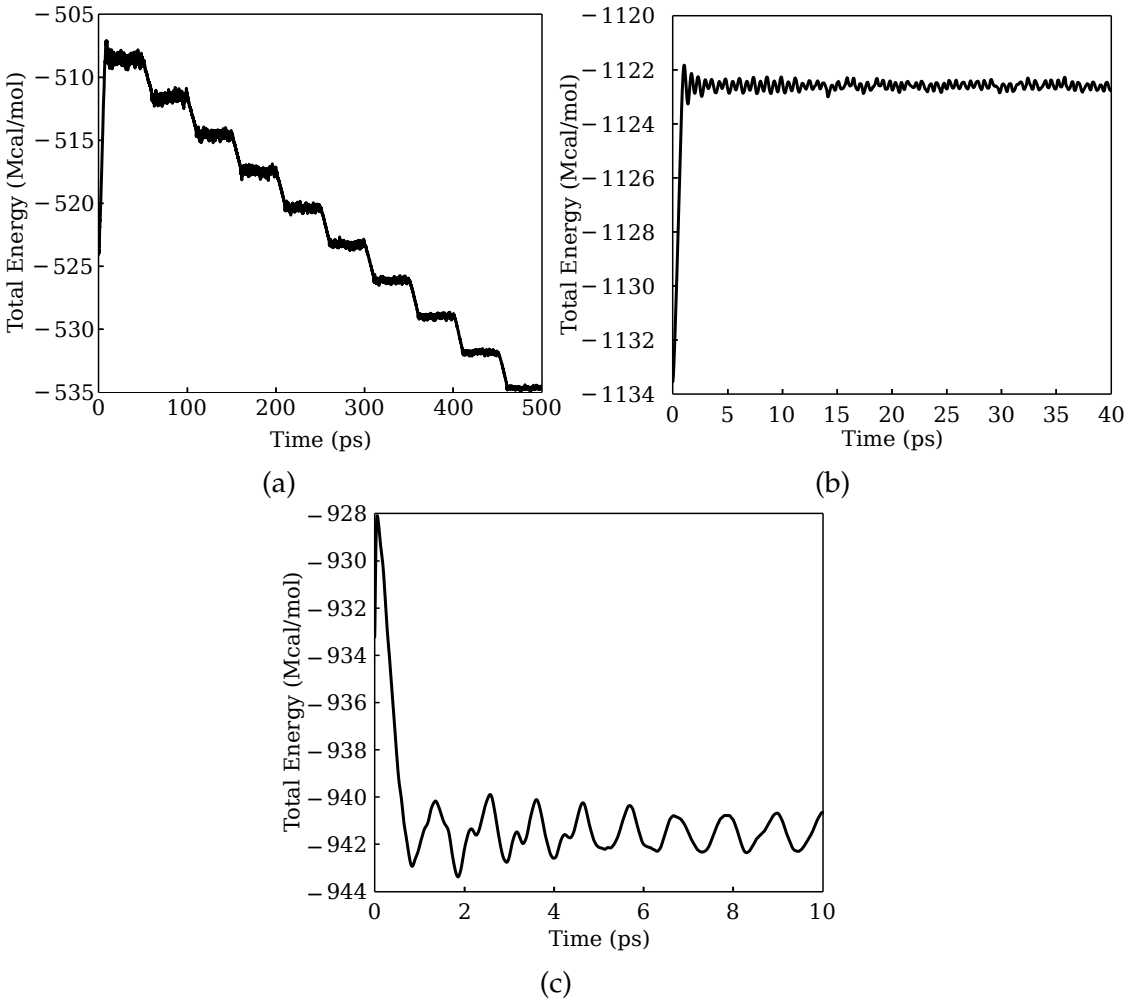

Fig. 2.6. Total energy trace for: **(a)** substrate cooling and equilibration, **(b)** interface equilibration, and **(c)** quasistatic shear equilibration.

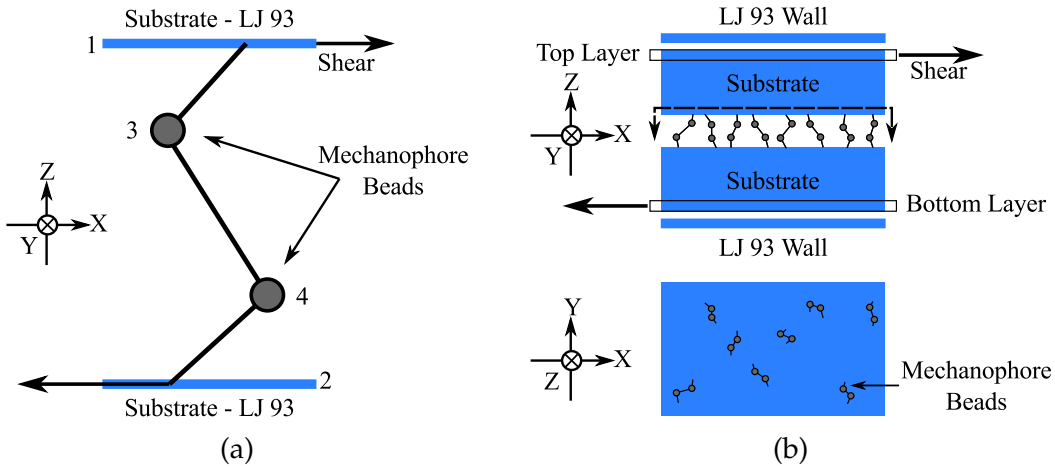

Fig. 2.7. Schematics of the two models for activation of mechanophores subjected to interfacial shear. **(a)** Kinematic model: Interface is formed by two LJ 9-3 walls with a randomly oriented coarse grained mechanophore in between. **(b)** MD model: Interface is formed by two atomistic substrates with eight randomly oriented and placed coarse grained mechanophores.

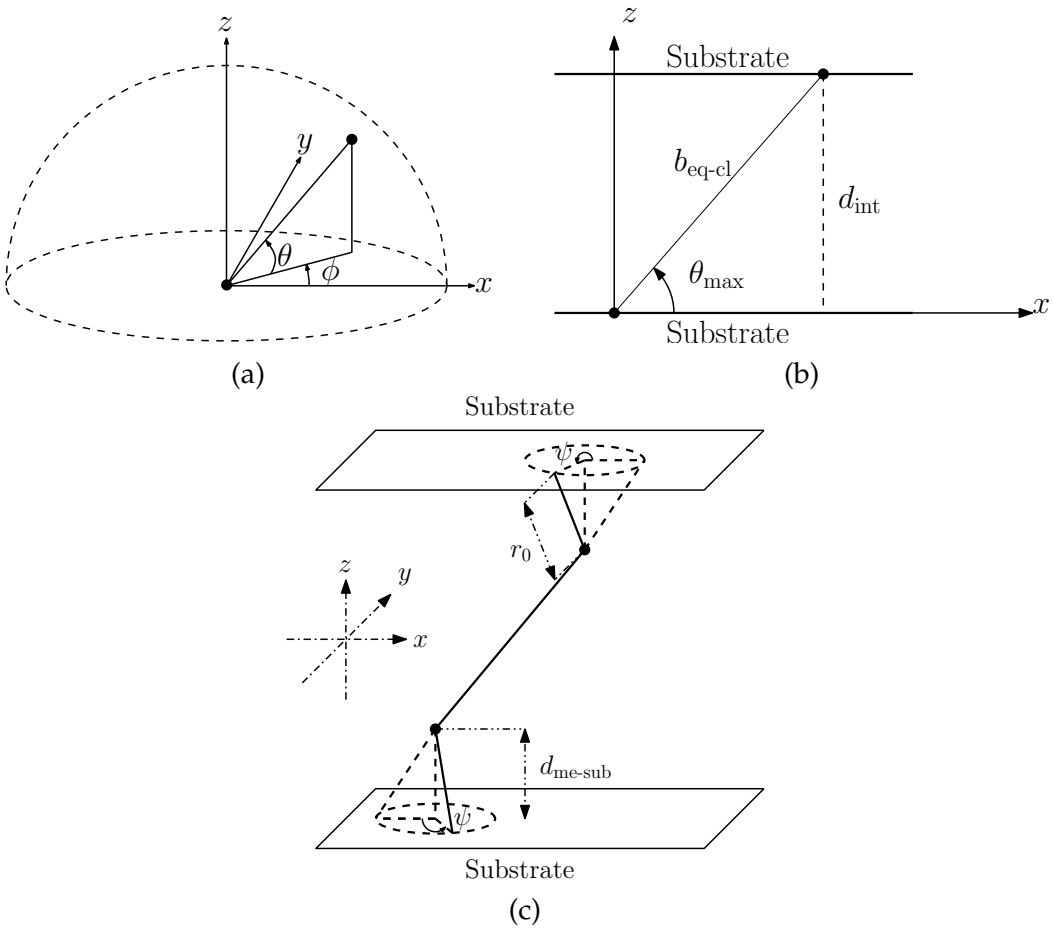

Fig. 2.8. **(a)** Orientation defining angles for mechanophore beads. **(b)** Restriction of the elevation angle. **(c)** Random orientation of the attachment bond.

surface of a cone with height $d_{\text{me-sub}}$ and slant height r_0 (see Fig. 2.8c). The choice of direction is made by picking a uniform random number for the angle $\psi \in [0, 2\pi]$. This fixes the point to which the mechanophore bead is bonded.

2.3 Results and Discussion

2.3.1 Kinematic Model

When mechanophores are rigidly attached to rigid substrates all mechanophores will progressively activate with interfacial displacement (Fig. 2.9a). Activation initiates at an interfacial distance close to the distance between the two minima of the double-well potential (slightly reduced due to the inclination of the mechanophore). Mechanophores that are oriented along the direction of shear activate first. To quantify mechanophore orientation we use the second order Legendre polynomial (P_2):

$$P_2 = \frac{3\langle \cos^2(\theta) \rangle - 1}{2} \tag{2.11}$$

where θ, is the angle with the direction of shear and $\langle \quad \rangle$ represents an average over a set of mechanophores. This function takes the value 1 for perfect alignment along the direction of shear, 0 for uniform random distributed orientations, and -0.5 for alignment perpendicular to the direction of shear. All mechanophores align themselves along the direction of shear given sufficient interfacial displacement, as indicated by the evolution of P_2 from 0.2 to 1 with interfacial displacement. The first mechanophores to open are those that are highly oriented along the shearing direction (Fig. 2.9b). Note that perfect alignment (P_2 =1) is not necessary for activation, and that the details of the progres-

sion of activation with interface displacement is a consequence of the choice of uniform random mechanophore orientations.

For non-rigid mechanophore to substrate attachments two kinds of behavior are observed. In Fig. 2.9a the progression of activation is plotted for three different bond potentials of the same α (α =1.07 Å^{-1}) and different D. When D equals 69.22 kcal mol^{-1} (case 1) and 44.30 kcal mol^{-1} (case 2) activation coincides with the rigid attachment scenario with all mechanophores activating as the shear progresses. For D equals 38.76 kcal mol^{-1} (case 3) no mechanophores activate with applied interfacial displacement. For case 3 all of the mechanophores detach from the substrate due to the weak substrate attachment (Fig. 2.9c), thereby removing the driving force for activation.

To identify the range of parameters of the attachment potential that enable mechanophore activation, we performed a grid search over α and D — the parameters for the Morse potential, and evaluated what percent of mechanophores activated at each combination of parameters. As seen in Fig. 2.9d there are two distinct regimes — one for which 100% of the mechanophores activate and one for which 0% of mechanophores activate. The former regime occurs when the attachment potential is deep and narrow, while the latter regime occurs when the attachment potential is shallow and wide. The curve that separates the two regimes coincides with a rectangular hyperbola

$$F_{\text{max}}^{\text{Morse}} = \frac{\alpha D}{2} = 1.44 \text{ nN} = F_{\text{Activate}}^{\text{Me}} \tag{2.12}$$

where the left hand side is the maximum force that can be exerted by the Morse potential and the right hand side is the force required to activate the mechanophore (derived from the double-well potential). For this scenario with perfectly flat substrates and only bonded interactions, the mechanophore-

substrate attachment bond must be capable of transmitting the force required to activate the mechanophores in order for any of the mechanphores to activate.

The presence of nonbonded interactions between the substrates and mechanophores perturbs the mechanophore response to interfacial shear (Fig. 2.10a). This perturbation is most apparent for case 2, which reaches only 3% activation when nonbonded interactions are present as compared to 100% activation with only bonded interactions. Revisiting the grid search now with nonbonded interactions present, we notice a narrow band over which the transition from 2% activation to 98% activation occurs (Fig. 2.10b). Some activation occurs for attachments with $F_{\text{max}}^{\text{Morse}} < F_{\text{Activate}}^{\text{Me}}$ and some detachment occurs with $F_{\text{max}}^{\text{Morse}} > F_{\text{Activate}}^{\text{Me}}$. To enable significant activation, the attachment potential needs to be reasonably stronger than the minimal requirement given by the force required to activate the mechanophore.

2.3.2 Molecular Dynamics Model

The presence of discrete substrate particles and ensemble dynamics as captured by the MD model does not significantly alter activation behavior (Fig. 2.10a). The substrate is effectively rigid as no substrate disintegration or shape change is observed during the MD simulation. Hence here too there are only two mechanisms at play, activation and detachment. There is a secondary thermal effect in case 2 for which activation reaches 5% with the total applied interfacial displacement instead of 3% predicted by the kinematic model.

Intersubstrate adhesion significantly influences mechanophore activation. Adhesion changes the configuration of the substrate atoms, resulting in sub-

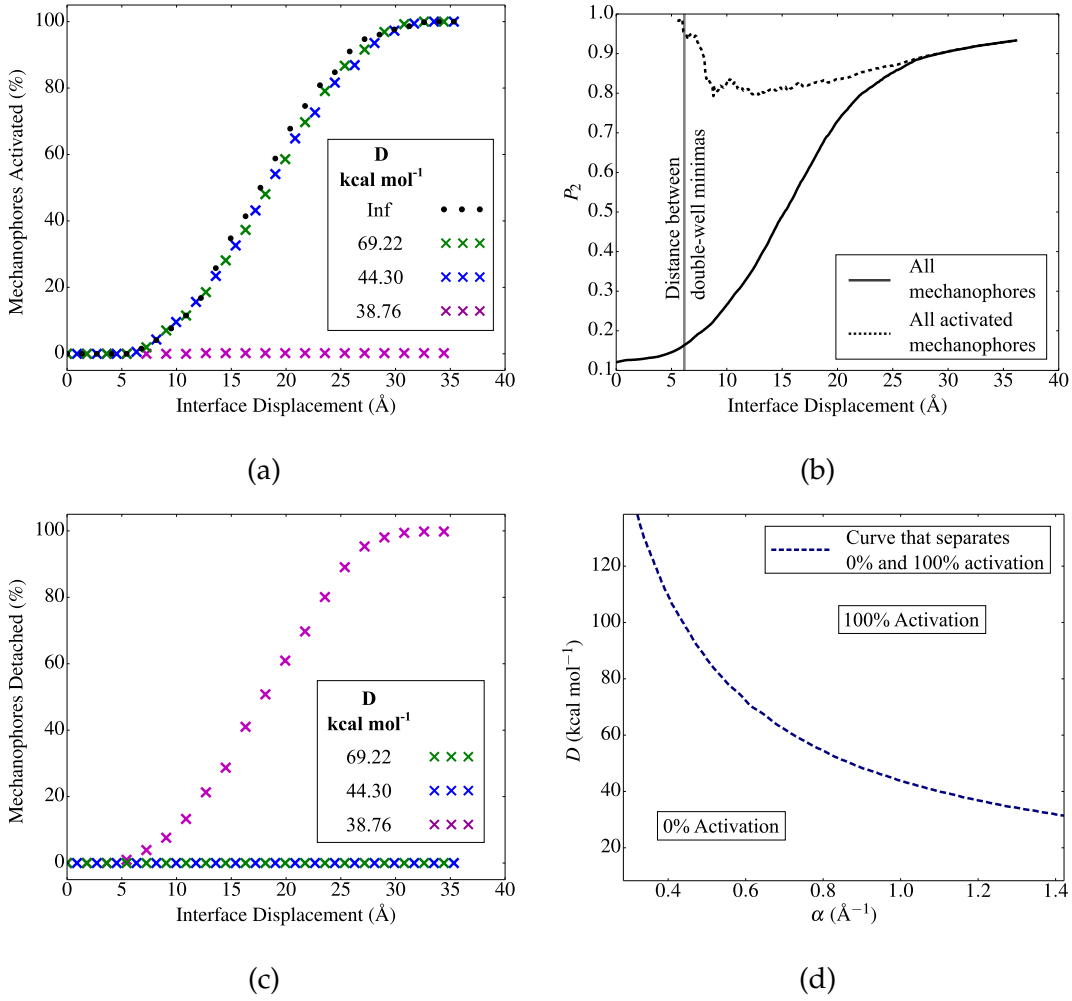

Fig. 2.9. Results for the kinematic model with only bonded interactions. **(a)** Activation trends of mechanophores with different attachment potential depths D and $\alpha = 1.07$ Å^{-1}. Here "Inf" refers to a rigid attachment. **(b)** Orientation trends over all mechanophores and over the set of activated mechanophores when the attachments are rigid.**(c)** Dissociation trends of the mechanophores indicate that they complement the activation trends i.e., mechanophores either activate or dissociate. **(d)** The grid search over the space of the attachment potentials separates the space into two regimes — one where no mechanophores activate and one where all mechanophores activate is given sufficient interfacial displacement.

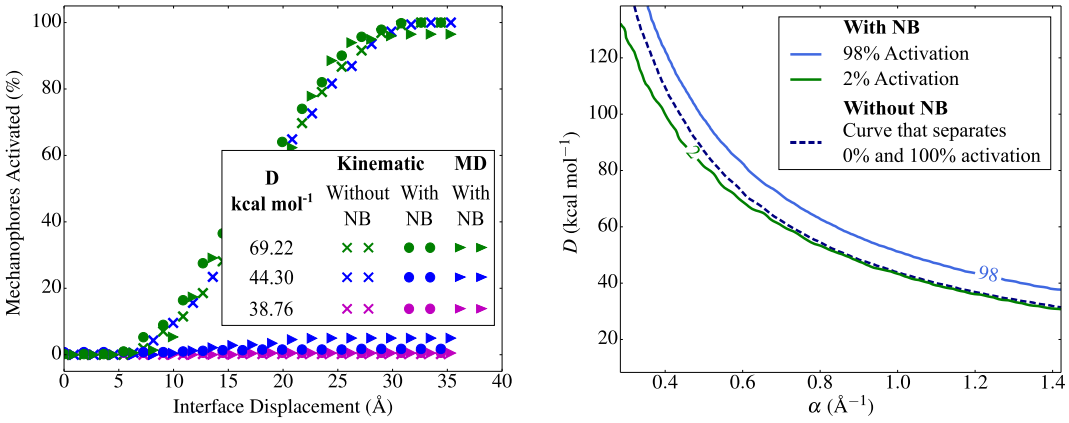

(a) (b)

Fig. 2.10. Results of the kinematic model with and without nonbonded (NB) interactions, and of the corresponding MD model. **(a)** Activation trends with interfacial displacement. **(b)** In the presence of NB interactions the grid search performed with the kinematic model shows a narrow band over which the transition from no activation to complete activation happens.

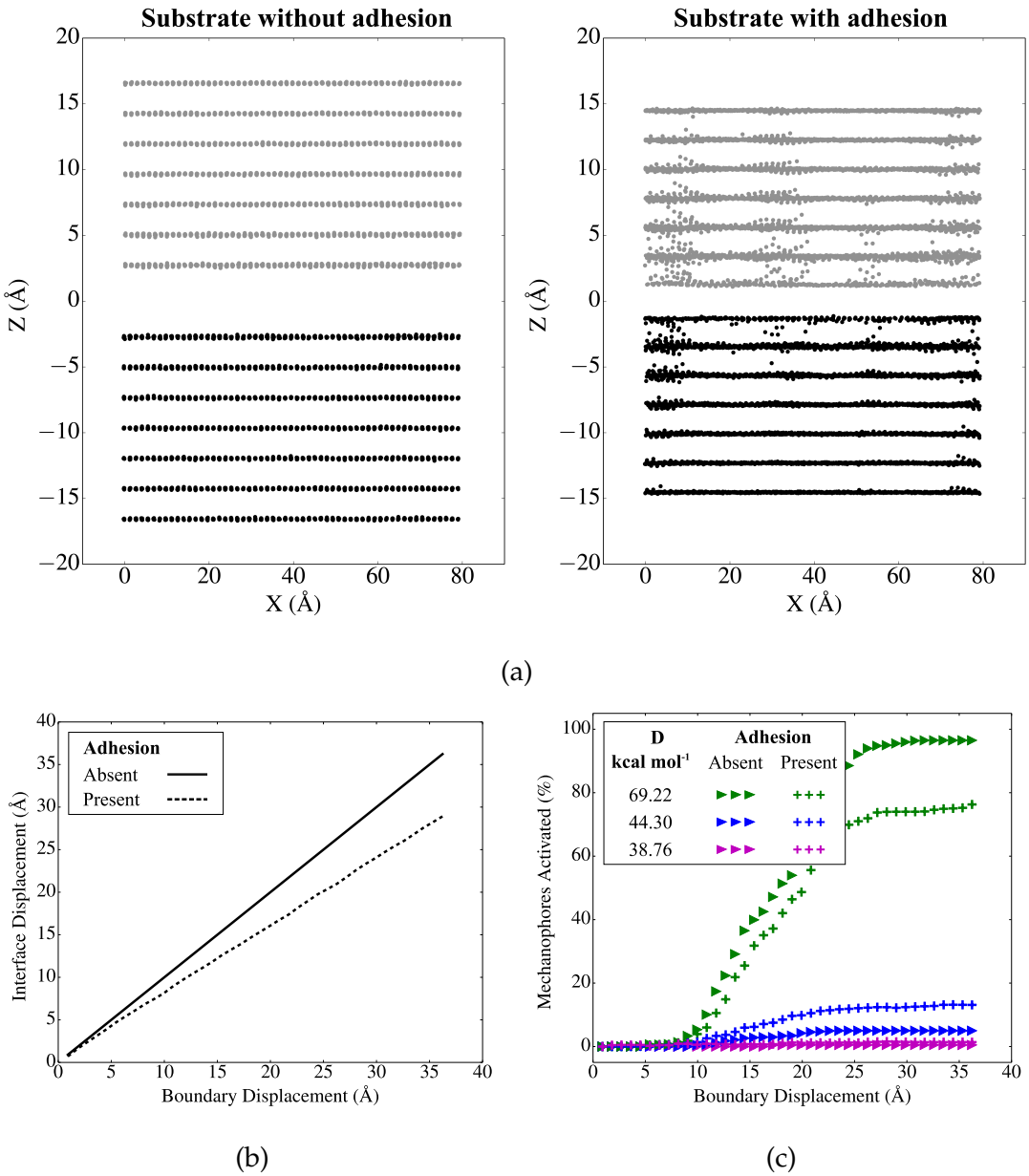

Fig. 2.11. Effect of inter-substrate adhesion on mechanophore activation determined by the MD model. **(a)** The interface configuration along the XZ plane is shown. The substrates come closer and they are rougher in comparison to the case without adhesion. **(b)** The interface displacement is less than the applied boundary displacement in the presence of adhesion. **(c)** Activation trends with and without adhesion.

strates that are rougher and on average close together (Fig. 2.11a). In contrast to the previously studied scenarios, adhesion retards the interface displacement in relation to the prescribed shear boundary displacement (Fig. 2.11b). As most clearly evident in case 1, the reduced interface displacement reduces the mechanophore activation at a given boundary displacement. Furthermore, the more closely interacting substrates aids in both activation and detachment of the mechanophores as can be seen in the simulated cases. This adhesion study illustrates that atomistic details of the substrates play an important role in altering the progression of mechanophore activation.

2.4 Conclusion

We have constructed a kinematic model and a molecular dynamics model to simulate mechanophore activation at an interface subjected to shear. Our investigation reveals that mechanophore activation happens progressively with interfacial displacement starting with the mechanophores aligned along the direction of shear. The onset of activation happens when the interfacial distance nearly equals the distance between two equilibrium states of the mechanophore. If only limited interfacial displacement is expected in the composite or coating failure, then the distance between equilibrium states of a potential mechanophore may limit its utility. Our analysis highlights that one critical aspect of interface design is to use mechanophore to substrate bonds that can survive forces larger than the mechanophore triggering force. However, some limited activation can occur even for weaker attachment bonds. Nonbonded interactions, temperature, and adhesion all contribute to both activation and detachment of mechanophores. If there is strong adhesion between the

substrates, the conformation of the substrates changes and the transmission of shear through the substrates is delayed, reducing the degree of activation for a given applied boundary displacement. This study offers insight for designing mechanophore functionalized self-healing and self-reporting interfaces for effective damage management. Future work is needed to investigate the effect of specific substrates for prospective applications.

CHAPTER 3

CONTINUUM MODELING OF MECHANOPHORES ON DEBONDING IN POLYMER COMPOSITES

3.1 Introduction

Polymer composites with fibrillar and particulate fillers offer a large range of physical properties that find widespread civil and industrial applications [70, 25]. Common fillers include alumina, silica, carbonates, carbon black, rubber, glass, and carbon nanotubes. These fillers range from the nanoscale to the microscale and their effect on composite properties depends on the filler mechanical properties, size, composition, spatial distribution, and interfacial adhesion [75, 15, 84]. The failure of these composites incur repair, replacement, and disposal costs during their lifecycle. Interface debonding is a common mode of damage in polymer composites [35, 30, 23, 86]. Composite interfaces are therefore a promising location to augment with an early-warning and/or a healing functionality in order to extend composite durability and life cycle management. An early warning or healing function can be added by placing mechanophores, chemical units designed to perform a specific chemical transformation in response to mechanical work at the interface. These mechanophores could be covalently bonded between the filler particle and the matrix to create interfacial mechanophore augmented composites (IMAC) that respond strategically to the debonding failure mode.

In this chapter we generate the framework for quantifying IMAC mechanochemistry and then apply this framework to the linear-elastic-interface damage regime of typical composites. Potential for mechanophore response is

analyzed based on an extensible link mechanophore model that ties into the mechanical deformation of the composite. We present the model in the next section, followed by a discussion of the pertinent material property ranges, and then our results. We utilize the classical 2D plane strain scenario of a circular particle (fiber) within an infinite matrix to understand the governing physics and map out the design space. We then demonstrate the facility of our approach by applying the framework to a 3D analysis of a low filler volume fraction spherical particle composite.

3.2 IMAC Mechanochemical Model

A mechanochemical model for a material needs to predict both the deformation response and the mechanophore response to an applied stress field. The key output of interest in an IMAC is the relative progression of debonding and mechanophore activation. The novelty of this work is in the prediction of the aggregate mechanophore response within the IMAC using an extensible link approximation of the mechanophore. This approximation of the mechanophore establishes the mechanophore-mechanics connection using the deformation field, while neglecting the influence of the mechanophore on the mechanics of the composite. There is an extensive composites literature concerned with the deformation response to stress and we choose a few mechanics models from the literature to demonstrate our approach. Although we will limit ourselves here to a few examples, the framework can readily be applied to any combination of loading mode, material constitutive behavior, and interface law for which the displacement fields can be solved. Specifically, this framework takes mechanics solutions for composite displacement fields in response to far

field stress and uses them to predict the mechanophore states based on their based on their location along the matrix/particle interface, orientation, and not-activated and activated lengths (Fig. 3.1). For linear elastic constituent materials, the matrix (m) and the circular particle (p) have Young's modulus E_m, E_p and Poisson's ratio ν_m, ν_p. The interface is governed by a nonlinear cohesive law relating the traction at the interface $\boldsymbol{\sigma}_{\text{int}}$ (interfacial traction) and the displacement between co-located points $[\mathbf{u}]$ (interfacial displacement) as,

$$\boldsymbol{\sigma}_{\text{int}} = \mathbf{f}\left([\mathbf{u}]\right). \tag{3.1}$$

The governing equations for the mechanics of a dilute composite with circular (2D) or spherical (3D) particles (Fig. 3.2) are summarized here (for a detail discussion see [38, 36, 37]). First the displacement field should satisfy the interface separation condition

$$[\mathbf{u}] = \mathbf{u}(\boldsymbol{\xi}^+) - \mathbf{u}(\boldsymbol{\xi}^-) \qquad \boldsymbol{\xi} \in \Gamma, \tag{3.2}$$

where $\mathbf{u}(\boldsymbol{\xi}^+)$ and $\mathbf{u}(\boldsymbol{\xi}^-)$ are the values of the displacement field on the interface point $(\boldsymbol{\xi})$ deforming with the matrix and deforming with the particle respectively. This is an implicit equation as the displacement fields in the matrix and the particle are created by the interfacial traction $\boldsymbol{\sigma}_{\text{int}}$, which in turn is dependent on the interfacial separation $[\mathbf{u}]$. Next, the interface tractions need to satisfy the balance of linear and angular momentum,

$$\int_\Gamma \boldsymbol{\sigma}_{\text{int}} \partial\Gamma = \mathbf{0} \tag{3.3}$$

$$\int_\Gamma \boldsymbol{\xi} \times \boldsymbol{\sigma}_{\text{int}} \partial\Gamma = \mathbf{0}. \tag{3.4}$$

The displacement field $\mathbf{u}(\mathbf{r})$ can be either found through setting up differential equations for the given boundary conditions or expressed using Greens func-

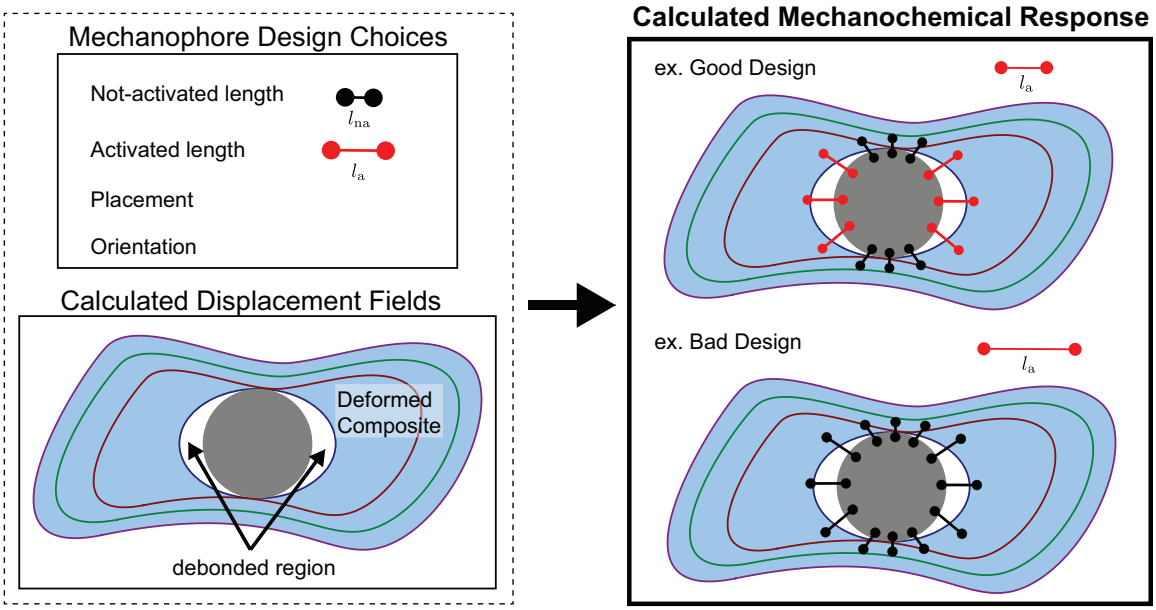

Fig. 3.1. Overview of modeling framework: The displacement field including debonding for a known composite and applied stress state is used to drive a mechanochemical model based on an kinematic extensible link mechanophore concept. Mechanophore properties and placement will determine the mechanochemical response for a given displacement field.

tions $\mathbf{G}_m(\mathbf{r}, \boldsymbol{\xi})$ and $\mathbf{G}_p(\mathbf{r}, \boldsymbol{\xi})$ for the matrix and particle side respectively as,

$$\begin{aligned} \mathbf{u}(\mathbf{r}) &= \boldsymbol{\varepsilon}_\infty \mathbf{r} + \int_\Gamma \mathbf{G}_m(\mathbf{r}, \boldsymbol{\xi}) \mathbf{T}_m(\boldsymbol{\xi}) \partial\Gamma \qquad && \boldsymbol{\xi} \in \Gamma, \mathbf{r} \in \Omega_m \\ \mathbf{u}(\mathbf{r}) &= \int_\Gamma \mathbf{G}_p(\mathbf{r}, \boldsymbol{\xi}) \mathbf{T}_p(\boldsymbol{\xi}) \partial\Gamma \qquad && \boldsymbol{\xi} \in \Gamma, \mathbf{r} \in \Omega_p. \end{aligned} \tag{3.5}$$

Here, $\boldsymbol{\varepsilon}_\infty$ is the remote strain in the matrix corresponding to the remote stress $\boldsymbol{\sigma}_\infty$, $\mathbf{T}_m(\boldsymbol{\xi})$ and $\mathbf{T}_p(\boldsymbol{\xi})$ are tractions exerted at the interface point $\boldsymbol{\xi}$ on the matrix side and the particle side respectively given by:

$$\begin{aligned} \mathbf{T}_m(\boldsymbol{\xi}) &= \boldsymbol{\sigma}_\infty \mathbf{n} - \boldsymbol{\sigma}_{\text{int}} \\ \mathbf{T}_p(\boldsymbol{\xi}) &= \boldsymbol{\sigma}_{\text{int}}. \end{aligned} \tag{3.6}$$

Here, $\mathbf{n}$ is the outward normal at the interface Γ between the particle and the matrix. While the above is general to particles with radial symmetry, for the remainder of the methods section we will focus on the case of circular particle bonded within a 2D infinite matrix under plane strain and far field stress.

We prescribe the particle/matrix interface cohesive law Eq. 3.1 as in [14],

$$\sigma_{\text{int}} = \sigma_{\max} \frac{[u]}{\delta} \exp\left(1 - \frac{[u]}{\delta}\right), \tag{3.7}$$

where σ_{int}, is the radial component of the interfacial traction, $[u] = u(r_p^+) - u(r_p^-)$ is the radial component of the interfacial displacement, $\sigma_{\max}$ is the interface strength i.e., maximum radial interfacial traction that the interface can resist to avoid debonding, and δ is the critical radial distance corresponding to $\sigma_{\max}$. A point on the interface is considered debonded if $[u] \geq \delta$ as any further increase in $[u]$ comes at a reduced interfacial traction. In a generic loading condition, to avoid penetration of the matrix surface into the particle surface we augment the cohesive law with a negative exponential portion when $[u] < 0$

$$\sigma_{\text{int}} = \sigma_{\max} \frac{\exp(1)}{\beta} \left(1 - \exp\left(-\frac{[u]\,\beta}{\delta}\right)\right), \tag{3.8}$$

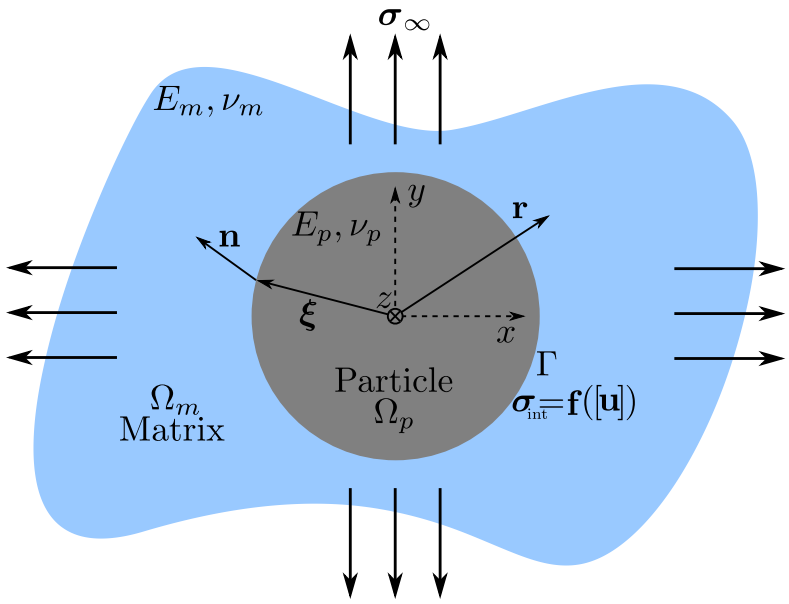

Fig. 3.2. The setup for a circular or spherical filler particle of within an infinite matrix subject to remote stress. Ω_m is the matrix domain, Ω_p is the particle domain, and Γ is the interface boundary. $\boldsymbol{\xi}$ represents a point on the interface Γ, $\mathbf{n}$ the normal at that point and $\mathbf{r}$ represents an arbitrary position vector in the system.

where β is a positive constant chosen as 25, large enough to prevent the penetration of the surfaces and to aid the convergence of solutions. The augmented interface cohesive zone traction model is shown in Fig. 3.3b.

The novelty of this framework lies in the mechanophore model and how it couples with the mechanics of the composite. Mechanophores are modeled as an extensible link, with end points rigidly attached to the matrix and particle, that deforms with these attached points (Fig. 3.3a). This extensible link model is a valid approximation of the full atomistic behavior as long as the mechanophore is strongly attached to two points and the mechanophores do not influence one another [50]. The mechanophore is characterized by l_{na}, the distance between the points of attachment of the mechanophore at the matrix and the particle prior to activation, and l_{a} is the same distance measured at activation (Fig. 3.3c). Before the composite is loaded, the mechanophore is in its not-activated state. The mechanophore links are assumed to exert negligible force on the matrix and the particle, thereby decoupling the elasticity solution from the mechanophore response. The particle end of the link is positioned at a radius $r_a \sim r_p$ at an angular position $\theta \in (0, 2\pi)$. The matrix end of the link is placed at a distance of l_{na} from the particle end along an orientation $\phi \in [-\phi_{\max}, \phi_{\max}]$, where

$$\phi_{\max} = \cos^{-1}\left(\frac{r_p^2 - r_a^2 - l_{\text{na}}^2}{2 r_a l_{\text{na}}}\right) \tag{3.9}$$

is the limiting angle found by the requirement to bond with the matrix (Fig. 3.3a, 3.3d). For each angular position we calculate an expectation $\mathcal{E}(\theta)$ that mechanophores will activate based on an averaging of the state of activation (1 - activated, 0 - not activated) over a random sampling of 128 allowable orientations (ϕ). Similarly expectation $\mathcal{E}$ that a mechanophore anywhere will activate is found by averaging $\mathcal{E}(\theta)$ over a random set of 128 angular positions $\theta \in [0, 2\pi]$.

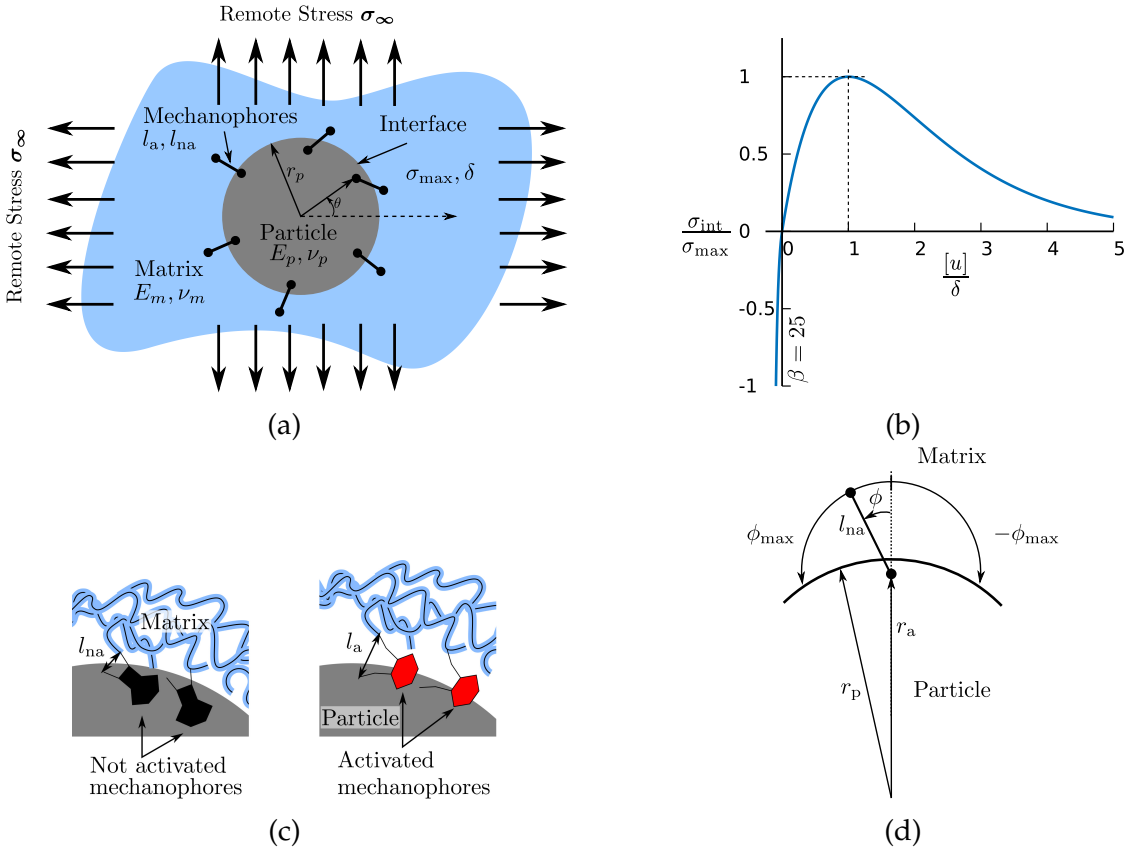

Fig. 3.3. Modeling details. (a) Representative IMAC studied. (b) The nonlinear interface cohesive law augmented to inhibit surface penetration. (c) Illustration of the mechanophore length scales. (d) The allowable orientations for mechanophore placement.

The mechanophore activation relative to the progress of interfacial separation is critical in an IMAC for self-healing and self-reporting functionality. Mechanophore activation well before debond would provide false alarms and mechanophore activation after debond may lead to ineffective healing due to large interfacial separation. In our representative system we monitor interfacial debonding and mechanophore activation while applying an increasing quasi-static load. We examine two commonly seen experimental loading scenarios: equibiaxial tension and uniaxial tension. For equibiaxial tension, the response is axisymmetric ($\mathcal{E} = \mathcal{E}(\theta)$); so we simply monitor a single angular location. For uniaxial tension we monitor both $\mathcal{E}(\theta)$ for the angular activation and $\mathcal{E}$ for the overall activation.

Solutions for the particle and matrix displacements (driving mechanophore length change) for equibiaxial loading are obtained from the work of [91]. When a remote equibiaxial stress σ_∞ is applied the radial displacement field $u(r)$ takes the form given by:

$$\begin{aligned} u(r) &= r\sigma_{\text{int}}\frac{(1-2\nu_p)(1+\nu_p)}{E_p} && r \le r_p \\ u(r) &= C_1 r + \frac{C_2}{r} && r \ge r_p \end{aligned} \tag{3.10}$$

for the particle and matrix respectively, where C_1, C_2 are

$$\begin{aligned} C_1 &= \frac{\sigma_\infty(1-2\nu_m)(1+\nu_m)}{E_m}, \\ C_2 &= \frac{r_p^2(\sigma_\infty - \sigma_{\text{int}})(1+\nu_m)}{E_m}. \end{aligned} \tag{3.11}$$

Equation 3.10 is implicit because σ_{int} is a function of $[u]$ as given by Eqs. 3.7 and 3.8. These displacement fields can now be plugged into Eq. 3.2 to obtain a single nonlinear univariate root finding problem. The axisymmetry guarantees that the other two governing equations Eqs. 3.3 and 3.4 are automatically satisfied.

This equibiaxial model can also account for an interphase with matrix Young's modulus $E(r)$ varying according to a powerlaw with index n, radius r and outer edge of the interphase r_m as,

$$E(r) = E_m \left(\frac{r}{r_m} \right)^n \qquad r_p < r \leq r_m. \tag{3.12}$$

The displacement field when an interphase is present is provided in the Appendix.

The solution for the case of uniaxial tension is derived from the general scenario by reducing the governing equations to a nonlinear multivariate algebraic equation in terms of the Fourier coefficients of the $[\mathbf{u}]$ as discussed in [38, 36, 37]. The shear component of interfacial traction is governed by the scenario of no-slip. The interfacial shear tractions τ_{int} are found by setting the tangential component of interfacial displacement $[v]$ to 0. The mechanics solution for this case is detailed in Appendix A of this chapter.

3.3 Material Properties

We choose material properties for our analysis from common composites for which debonding is the dominant failure mechanism. Since rubbery filler particles and matrices typically fail by cavitation-type damage [45, 20, 89], they are excluded from our parameter space. In industrial applications the non-rubbery filler sizes range from nanoscale to microscale and are usually stiffer than their corresponding matrix (Table 3.1). The existence of an interphase surrounding particles in a nanocomposite is now well established in the nanocomposite literature, however the extent and stiffness of this region is debated in the literature

[8, 3, 7]. We characterize the range in possible interphase parameters by thickness $r_m - r_p$, and the ratio of matrix Young's modulus just at the filler particle to the bulk matrix properties $E_{\text{rel}} = \frac{E(r_p^+)}{E_m}$ (Table 3.1). The index of the power law n in Eq. 3.12 is computed from the interphase stiffness ratio.

Interface properties are critical to the progression of interface separation with stress. We considered both experimental and simulation sources of interface parameters for typical composites. There have been a number of experiments that obtain cohesive zone strength and critical length from combined force and displacement field measurements, however this parameter estimation is limited by the micrometer length scales at which observations are typically made [12, 53, 21]. While these parameters are useful for making subsequent bulk behavior predictions, they are unrealistic for our work for which the debond length scale strongly impacts mechanophore activation. Estimates of cohesive law parameters from molecular dynamics simulations of graphene and carbon nanotube based polymer composites give nanometer scale debond lengths and GPa level strengths [29, 1, 28, 43]. We assume that cohesive zone parameters also apply to other types and scales of interface between filler particles and matrices. We will assess the sensitivity to this assumption in the results section.

Mechanophores are described in this work by not-activated and activated attachment point distances. These length scales have been chosen to span from current published covalent mechanophores through proteins that could effectively act as mechanophores. Mechanophore covalent attachment to the filler is assumed to happen quite close to the surface of the filler so an attachment depth of a few Å is chosen.

3.4 Results and Discussion

To illustrate the connection between the debonding mechanics and mechanophore activation we start by exploring the scenario of a rigid particle within a matrix without an interphase that is subjected to equibiaxial loading. This simple scenario also serves as a platform for investigating the selection of mechanophores. We then make modifications to this IMAC to look at the impact of each material property on the interplay of mechanics and activation.

We begin by identifying key non-dimensional quantities. Expanding Eq. 3.2 for a rigid filler particle we get the nonlinear equation,

$$\frac{[u]}{r_p} = 2\frac{\sigma_\infty}{E_m}(1-\nu_m^2) - \frac{\sigma_{\max}}{E_m}(1+\nu_m)\frac{[u]}{\delta}\exp\left(1-\frac{[u]}{\delta}\right) \tag{3.13}$$

which equates the interfacial hoop strain to the difference between the hoop strain of a free void under remote load and the hoop strain due to the interfacial traction. Non-dimensionalizing lengths by δ and stresses by E_m we obtain that the normalized interface separation $[U] = \frac{[u]}{\delta}$ depends upon the Poisson's ratio of the matrix ν_m, the normalized particle radius $R_p = \frac{r_p}{\delta}$, the normalized remote stress $\Sigma_\infty = \frac{\sigma_\infty}{E_m}$, and the normalized interface strength $\Sigma_{\max} = \frac{\sigma_{\max}}{E_m}$. This interface separation is critical because it is the chief quantity driving mechanophore activation. The mechanophore initial length and required length change for activation are also non-dimensionalized by the debond length as $L_{\text{na}} = \frac{l_{\text{na}}}{\delta}$ and $\Delta L = \frac{l_{\text{na}} - l_{\text{a}}}{\delta}$ respectively.

Debonding of the composite depends on $\Sigma_{\max}$, ν_m, and R_p. We illustrate the dependence by comparing a reference composite (Table 3.2) with three composites each differing by one of these parameters (Fig. 3.4a). As the remote load

(Σ_∞) is increased from zero, the interfacial separation ($[U]$) gradually increases with interface tractions resisting debond until the interface reaches its critical normalized displacement $[U] = 1$ and simultaneously the normalized interface stress reaches $\Sigma_{\max}$. With further increase in Σ_∞, interface separation jumps as the interface tractions drop to zero, asymptotically reaching the linear elastic displacement of a void within an infinite matrix. The remote stress at which the interface debonds is greater for greater interfacial traction resisting debond ($\Sigma_{\max}$). This greater resistance also lowers the initial separation versus stress slope and increases the jump required to reach the void deformation regime relative to the reference composite. For a larger matrix Poisson's ratio, at the same remote load the void hoop strain decreases, in turn increasing the interface hoop strain. Therefore the remote stress at which debond occurs is higher for a larger Poisson's ratio. In case of a larger particle radius, the remote stress at which the interface debonds is lower than for a smaller particle because the interface hoop strain associated with critical displacement is lower.

Extensible link mechanophores are stretched according to the composite displacement fields near the interface. The change in length required for mechanophore activation selects the interfacial separation regime where mechanophores are expected to activate (Fig. 3.4b). For the set of matrix, particle, and interface properties prescribed in the reference composite, mechanophores with $\Delta L = 0.2$ are expected to complete activation prior to debond (false alarm), mechanophores with $\Delta L = 2.0$ are expected to start activation after debond (where sensing damage may loose relevance), and mechanophores with $\Delta L = 0.8$ are expected to activate during debond (desirable). The other mechanophore length scale, L_{na}, effectively sets how deep into the matrix the mechanophore can attach and what range of orientations

Table. 3.1. Property ranges for the polymer matrix, mechanophores, particle, interface, and interphase.

Polymer matrix		**Mechanophore**	
Youngs modulus (E_m)	0.1-10 GPa	Activated length (l_{a})	0.5-3 nm
		Not activated length (l_{na})	0.1-3 nm
Poisson's ratio (ν_m)	0.3-0.45	Attachment ($r_p - r_a$)	0.0-0.2 nm
References	Young and Lovell [87] Granta Design Ltd. [17]	References	Davis et al. [10] Klukovich et al. [31]

Filler particle	**Nanoscale**	**Microscale**
Youngs modulus (E_p)	70-1000 GPa	70-380 GPa
Poisson's ratio (ν_p)	0.2-0.3	0.2-0.3
Radius (r_p)	1-100 nm	1-100 µm
References	Bernardo et al. [3] Odegard et al. [59] Cho et al. [9] Hua et al. [24] Murín et al. [54]	Cho et al. [9] Tsui et al. [76] Rothon [70]

Interface		**Interphase**	
Strength ($\sigma_{\max}$)	0.1-5 GPa	Width ($r_m - r_p$)	2-100 nm
Critical length (δ)	0.5-5 nm	E_{rel}	0.75-2.3
References	Jiang et al. [29] Awasthi et al. [1] Li and Seidel [43] Jiang [28]	References	Cheng et al. [8] Bernardo et al. [3] Cheng et al. [7]

Table. 3.2. Reference composite where the filler particle is assumed rigid.

Reference composite					
E_m	ν_m	δ	$r_p - r_a$	r_p	$\Sigma_{\max}$
800 MPa	0.3	0.75 nm	0.1 nm	10 nm	0.15

it can take. For a greater L_{na} the IMAC is expected to start activation at a lower remote stress and end activation at a greater remote stress (Fig. 3.4b). Mechanophore activation originates with the mechanophores aligned closest to the radial direction and progresses to the farthest from aligned ones (Fig. 3.4c). Therefore the broadening of the activation stress range with greater L_{na} is attributed to greater displacement from matrix deformation for the most aligned mechanophores ($\phi = 0$) and greater limiting angle $\phi_{\max}$ (some mechanophores start off further from radially aligned).

To identify and design the system so that mechanophores activate at an optimal point, we study the interplay between two crucial quantities: $\Sigma_{\max}$ and ΔL. While the former affects the debonding behavior, the latter selects the interface separation regime over which activation is expected to occur. The remote stress at which activation is expected to start ($\mathcal{E} \rightarrow 0^+$), and end ($\mathcal{E} \rightarrow 1$) are denoted by Σ_{start} and Σ_{end} respectively; the remote stress at which the interface debonds is denoted by Σ_{debond}. For each $\Sigma_{\max}$ and ΔL we compute whether the mechanophores are expected to complete activation prior to debond, start activation prior to and complete after debond, or start activation after debond. This result is presented in an activation map (Fig. 3.4d). The regime where activation completes before debond, the zone of false alarm, is bounded on one side by the line $\Sigma_{\text{debond}} = \Sigma_{\text{end}}$ that is independent of $\Sigma_{\max}$. This bound is set by the furthest from aligned mechanophore ($\phi = \pm\phi_{\max}$) activating at debond ($[U] = 1$). This purely geometric quantity is

$$\Delta L = \sqrt{(1 + R_p + L_{\text{na}}^2) - \frac{R_a^2}{R_p} + \frac{L_{\text{na}}^2}{R_p}} - L_{\text{na}} \tag{3.14}$$

where $R_a = \frac{r_a}{\delta}$ is the non-dimensionalized mechanophore attachment radius.

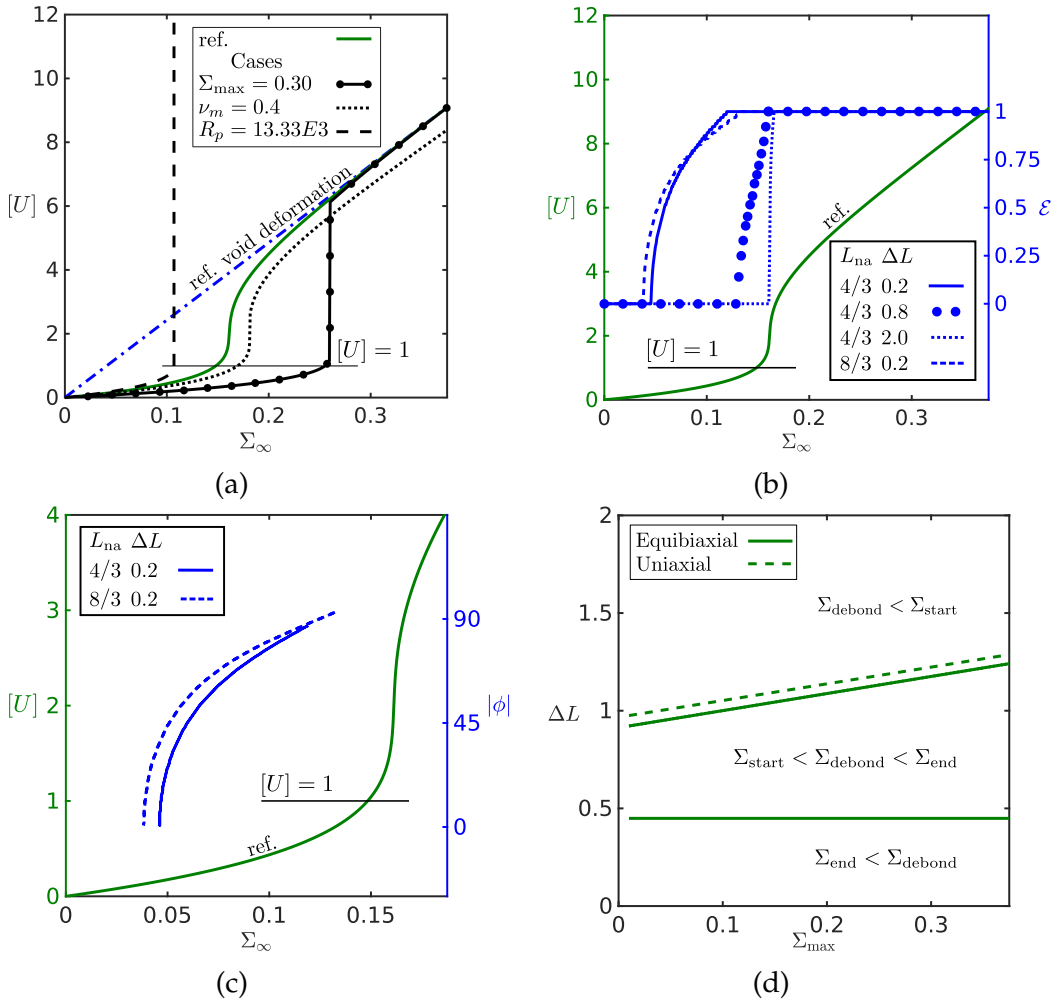

Fig. 3.4. Equibiaxial analysis for an IMAC with a rigid particle and no interphase: (a) Mechanics of interfacial debonding as function of increasing load. (b) The expectation of mechanophore activation with respect to increasing load for four mechanophore choices. (c) Mechanophore orientations that activate at that remote load. (d) Activation map identifying regimes where mechanophore activation is expected to complete prior to debond, occur during debond, and start after debond, shown for the reference composite with mechanophores of $L_{\text{na}} = 4/3$ and varying $\Sigma_{\max}$. Uniaxial bound for the same IMAC also shown.

The regime where activation starts after debond, the zone where damage detection/healing may loose relevance, is bounded on one side by the line $\Sigma_{\text{debond}} = \Sigma_{\text{start}}$, which is derived from the condition that the radially aligned mechanophore ($\phi = 0$) activates at debond i.e.,

$$\Delta L = \left.\frac{u\left(r_a + l_{na}\right)}{\delta}\right|_{\frac{\sigma_\infty}{E_m}=\Sigma_{\text{debond}}}. \tag{3.15}$$

Substituting into Eq. 3.10 we get,

$$\begin{aligned}\Delta L =& \frac{1}{2R_p}\left(\left(\frac{1-2\nu_m}{1-\nu_m}\right)\left(R_a + L_{\text{na}}\right) + \left(\frac{R_p^2}{R_a + L_{\text{na}}}\right)\left(\frac{1}{1-\nu_m}\right)\right) \\ &+ \frac{\Sigma_{\max}}{2}\frac{(1-2\nu_m)(1+\nu_m)}{(1-\nu_m)}\left(\left(R_a + L_{\text{na}}\right) - \frac{R_p^2}{R_a + L_{\text{na}}}\right).\end{aligned} \tag{3.16}$$

This bound is affected by $\Sigma_{\max}$ since at $\phi = 0$ both matrix deformation and interface separation contribute to mechanophore activation. Greater $\Sigma_{\max}$ corresponds to greater Σ_{debond} and matrix deformation at debond, which implies that a larger mechanophore length change is required to start activation after debonding. From the perspective of designing IMACs, the range of possible mechanophore length scales that will activate during debonding increases with increasing interface strength relative to matrix elastic modulus.

At this juncture we underscore the sensitivity of the model to the choice of interface parameters $\sigma_{\max}$ and δ since these are the material parameters with the greatest uncertainty. To reach a given radial interfacial separation $[u]$, the remote stress σ_∞ increases linearly with respect to $\sigma_{\max}$. This in turn implies that mechanophores are expected to start and end activation at larger remote stresses with larger $\sigma_{\max}$ as can be seen in the Table 3.3. From the activation map in Fig. 3.4d, we can directly see the impact of $\sigma_{\max}$ - larger $\sigma_{\max}$ implies greater choice of desirable mechanophores.

The dependence of debond and activation on δ is more complex than that

of $\sigma_{\max}$. Radial interfacial separation $[u]$ is inversely proportional to δ prior to debond and directly proportional to δ after debond. This in turn implies that mechanophores that complete activation before debond are expected to start and end activation at lower remote stresses with greater δ and mechanophores that start activation after debond are expected to start and end activation at higher remote stresses with greater δ. In Table 3.3 we show these differing trends for the examples of δl =0.15 nm (before debond) and δl =1.5 nm (after debond) as δ is doubled. With regards to the selection of desirable mechanophores, a mechanophore that activates after debond will tend towards activating during debond as the choice of δ increases and with further increase in δ will activate well before debond. This shift in the selection regions can be inferred from the dimensional forms of equations 3.14 and 3.16.

The uniaxial stress IMAC mechanochemical response is analyzed as an example alternate loading mode. For simplicity we present a no-slip analysis at the interface, a more comprehensive analysis is presented in Appendix B of this chapter. Under uniaxial stress the response is no longer axisymmetric with interface separation largest along the axis of loading ($\theta = 0^o$) and near zero at points perpendicular to the axis of loading ($\theta = 90^o$). Activation trends follow interfacial separation just as in the equibiaxial case, with mechanophore change in length relative to debond length as the critical design parameter. In contrast to the equibiaxial case, activation will not complete until long after debond because of the off loading axis mechanophores. In Fig. 3.4d we compare the start activation after debond bound with that for equibiaxial loading. The bound is shifted slightly up because there is more matrix displacement at $\phi = 0$, $\theta = 0$ for a given interface separation than for equibiaxial loading. It should be noted that the aggregate signal intensity for a given far field stress and quantity of

Table. 3.3. Sensitivity of activation and debonding to interface cohesive law parameters demonstrated by using the reference composite with $l_{\text{na}} = 1\,\text{nm}$.

$\Sigma_{\max}$	$\delta l = 0.15\,\text{nm}$		$\delta l = 1.5\,\text{nm}$		Σ_{debond}
	Σ_{start}	Σ_{end}	Σ_{start}	Σ_{end}	
0.15	0.046	0.120	0.161	0.166	0.149
0.30	0.070	0.214	0.260	0.260	0.256
0.45	0.087	0.309	0.366	0.366	0.363

δ(nm)	$\delta l = 0.15\,\text{nm}$		$\delta l = 1.5\,\text{nm}$		Σ_{debond}
	Σ_{start}	Σ_{end}	Σ_{start}	Σ_{end}	
0.50	0.057	0.131	0.139	0.139	0.135
0.75	0.046	0.120	0.161	0.166	0.149
1.00	0.040	0.107	0.180	0.191	0.163

mechanophores will in general be lower for uniaxial than equibiaxial because a more limited set of angular (θ) locations will be activated.

While our discussion until now has focused on a system with no interphase, the impact of an interphase on debonding and activation is relevant from a practical stand point. In the void displacement regime, we find that a stiff interphase $E_{\text{rel}} > 1$ will experience smaller radial interfacial separation $[u]$ in comparison with a homogeneous matrix for the same remote stress. In contrast, well before debond a composite with a stiff interphase has greater radial interfacial separation relative to the homogeneous matrix for the same remote stress. The converse is true for a compliant interphase in both the post and prior to debond ranges. This complex interphase effect is attributed to the lack of monotonicity in stress states with respect to radial distance in the interphase (see [22]) and the presence or absence of radial interfacial tractions. However, within the range of interphase parameters found in the literature (Table 3.1) we see negligible change in $[U]$ prior to debond for a composite with an interphase in comparison to one without an interphase (Fig. 3.5a).

Based on the above discussion we may anticipate that for a stiff interphase mechanophore activation prior to debond will happen at a lower remote stress compared to a composite with a homogeneous matrix. But this need not be true because of the non-monotonic stress state along the radial direction within the interphase. For example in the inset of Fig. 3.5b greater remote stress is required to activate mechanophores having $\Delta L = 0.2$ in a stiff interphase relative to the reference composite. Within the material range considered, for mechanophores that activate prior to debond the activation trends do not differ significantly. In Fig. 3.5b the relative difference between the activation curves

for the mechanophore that activates prior to debond does not exceed 4.16% for response integrated until Σ_{debond} for the reference composite. On the other hand, for mechanophores that activate after debond there is a significant difference in activation trends with interphase changes as seen in Fig. 3.5b. For the stiff interphase the mechanophores activate at greater remote stress than the reference composite, and for the compliant interphase the mechanophores activate at a lower remote stress than the reference composite. Considering the choice of desirable mechanophores in the activation map, the presence of an interphase does not affect the bound $\Sigma_{\text{debond}} = \Sigma_{\text{end}}$ (purely geometric), but it does shift the bound $\Sigma_{\text{debond}} = \Sigma_{\text{start}}$, which is related to matrix pliability (Fig. 3.5c). In summary the change in compliance of the matrix adjacent to the interface alters debonding mechanics and mechanophore activation slightly.

Another feature of practical relevance is the elasticity of the filler particle. The hoop strain of the filler particle influences the debonding mechanics and is given by:

$$\frac{u(r)}{r} = \sigma_{\max}\frac{[u]}{\delta}\exp\left(1-\frac{[u]}{\delta}\right)\frac{(1-\nu_p)}{E_p}. \tag{3.17}$$

Accounting for a deformable particle, the relation for $[u]$ in Eq. 3.13 becomes,

$$\frac{[u]}{r_p} = 2\frac{\sigma_\infty}{E_m}(1-\nu_m^2) - \sigma_{\max}\frac{[u]}{\delta}\exp\left(1-\frac{[u]}{\delta}\right)\left(\frac{1+\nu_m}{E_m}+\frac{1-\nu_p}{E_p}\right) \tag{3.18}$$

where we have additionally subtracted the hoop strain of the particle. When the particle is compliant it reduces $[u]$ for a given remote stress in comparison with a particle that is rigid. This reduction implies that activation will begin and complete at a greater remote stress for a compliant particle compared to a rigid particle. For example, in Fig. 3.6 results are presented for IMACs with the

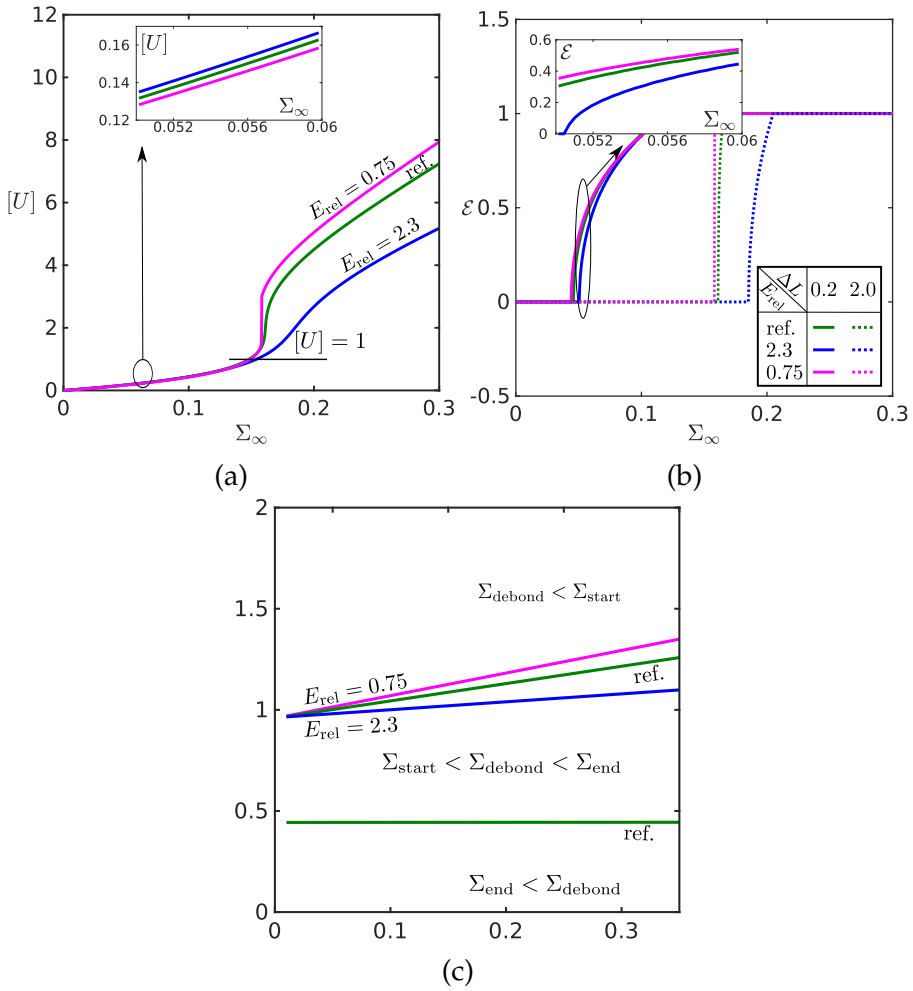

Fig. 3.5. The effect of an interphase: (a) The debonding mechanics of the reference composite (Table 3.2) are compared with two otherwise equivalent composites that have a $10\,\text{nm}$ interphase, one stiff and one compliant relative to the matrix. Inset shows a zoomed in view of the radial interfacial separation prior to debond for all the composites. (b) Mechanophores with $L_{na} = 4/3$ are used to demonstrate the possible impact of the interphase on activation. Inset shows a zoomed in view of activation trends of the mechanophore with $\Delta L = 0.2$. (c) Activation map shown for all the composites with mechanophores of $L_{\text{na}} = 4/3$ and varying Σ_{max}.

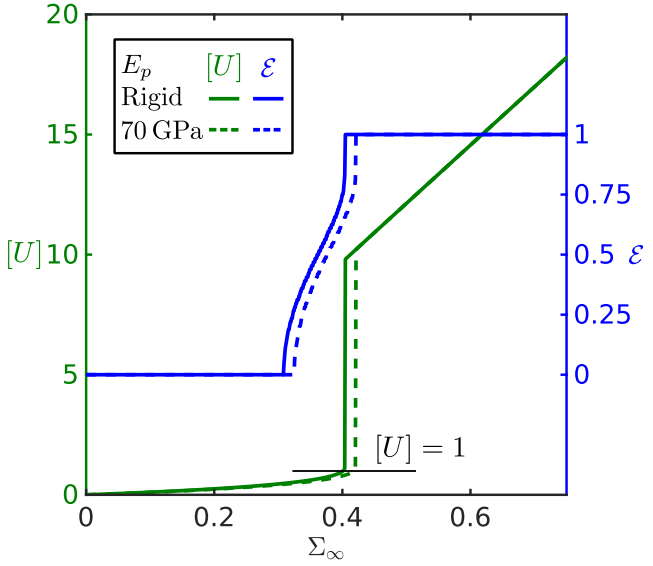

Fig. 3.6. Example of how the debonding mechanics and activation trends depend on filler particle compliance. The IMACs have the following properties: E_m =10 GPa, $\nu_m = \nu_p = 0.3$, r_p =10 nm, $\sigma_{\max}$ =5 GPa, δ =0.75 nm, $L_{\text{na}} = 4/3$, $\Delta L = 0.8$, and $r_p - r_a$ =0.1 nm.

stiffest possible matrix, interfaces of the maximal interfacial strength, and two extremal filler particles - one at the compliant end of the likely particle properties and the other rigid (Table 3.1). The relative difference of the interfacial separation and activation prior to debonding between these two scenarios are 1.55% and 2.47% respectively, indicating that a rigid particle assumption is reasonable for the typical non-rubbery composite.

3.5 Application to Uniaxial Tension of Particle Filled Composite

Here we apply the IMAC analysis framework to uniaxial loading of a linear elastic matrix with a low volume fraction of well dispersed effectively rigid spherical particles. The interface is governed by a nonlinear cohesive law [77] that includes a normal σ_{int} and a shear component τ_{int} given by,

$$\begin{aligned}
\sigma_{\text{int}} &= \left(\frac{\phi_n\,[u]}{\delta_n^2}\right)\exp\left(-\frac{[u]}{\delta_n}\right)\exp\left(-\frac{[v]^2}{\delta_t^2}\right) && [u]\geq 0\\
\sigma_{\text{int}} &= \left(\frac{\phi_n}{\beta\delta_n}\right)\exp\left(1-\frac{[v]^2}{\delta_t^2}\right)\left(1-\exp\left(-\frac{[u]\,\beta}{\delta_n}\right)\right) && [u]<0\\
\tau_{\text{int}} &= 2\left(\frac{\phi_t\,[v]}{\delta_t^2}\right)\left(1.0+\frac{[u]}{\delta_n}\right)\exp\left(-\frac{[v]^2}{\delta_t^2}\right)\exp\left(-\frac{[u]}{\delta_n}\right). && (3.19)
\end{aligned}$$

Here, ϕ_n, ϕ_t is the work of separation along the normal and the tangential directions and δ_n, δ_t are the critical length scales for debond along the normal and tangential directions. The portion of the normal law when $[u] < 0$ is augmented to prevent interpenetration of the matrix and the particle, where β is set to 25.

The mechanics solution is obtained from [74] and is based on the construction of a representative volume element (RVE) with an effective matrix and a

single spherical particle loaded remotely. This assumption represents the IMAC when particles are well dispersed and dilute. The displacement solution for the uniaxially loaded RVE follows the methodology outlined through Eqs. 3.2 - 3.4 and displacement solutions from [47]. Using rotational symmetry along the loading axis and expressing the interfacial displacements in terms of a Legendre polynomial expansion in spherical coordinates we reduce the equations into a nonlinear set of algebraic equations. From the solution of the RVE the average uniaxial strain $\bar{\epsilon}$ for the average uniaxial stress $\bar{\sigma}$ is computed (Appendix A).

To obtain the mechanochemical activation we need to only consider the RVE. Here extensible link mechanophores are placed at a radius r_a within the filler particle, and randomly oriented into the matrix. Expectation for activation $\mathcal{E}(\theta)$ is calculated using 128 randomly oriented mechanophores where θ is the angle relative to the loading direction. The overall expectation for activation $\mathcal{E}$ in the IMAC is computed by averaging $\mathcal{E}(\theta)$ over the sphere.

We present the impact of volume fraction on IMAC response with increasing strains for an IMAC with rigid particles and properties shown in Table 3.4. In

Table. 3.4. Properties of IMAC with spherical particles.

E_m	ν_m	ϕ_n	ϕ_t	δ_n
800 MPa	0.3	$0.123\,\mathrm{Jm}^{-2}$	$0.123\,\mathrm{Jm}^{-2}$	0.75 nm
δ_t	$r_p - r_a$	r_p	l_{na}	l_{a}
0.75 nm	0.1 nm	10 nm	1 nm	1.6 nm

Fig. 3.7a we illustrate the mechanical response of the IMAC with change in filler volume fraction (v_f). The interface separation model here has two critical length scales δ_n and δ_t. When both of these are crossed the interface starts to separate. Prior to interfacial separation the stiffness of the composite increases with increasing volume fraction. After interfacial separation, the higher volume

fraction composites have lower stiffness. We show the average stresses and strains required for reaching δ_n and δ_t in Table 3.5.

In Fig. 3.7b we present the expected mechanophore activation response which is uniform for all volume fractions when viewed in terms of stress. Mechanophores are expected to start activation after δ_t is reached in this particular composite for all volume fractions. In terms of strain, activation will progress slowest for the highest filler volume fraction.

3.6 Conclusion

In this work we propose a framework for modeling the mechanochemical response of IMACs. We connect mechanochemical response to mechanical response by assuming that the mechanophores are extensible links that deform with their attachment points without exerting any traction on the interface. We find that mechanophore activation is governed by mechanophore length scales relative to critical interface length scales, interfacial strength relative to the matrix stiffness, matrix Poisson's ratio, the size of the particle, and the type of loading. The interfacial strength relative to the matrix stiffness predominantly controls the mechanics of the system with greater strength leading to greater strain and far field stress at which the interface debonds. The mechanophore length scales select the interfacial separation over which the mechanophores activate. Larger change in length with activation relative to the debond length scale leads to activation at larger stresses. Similarly to in elastomers, mechanophore orientation is important for the progression of activation. For equibiaxial loading, radially oriented mechanophores activate first. For non-axisymmetric loading

Table. 3.5. Average stress, strain, activation for critical interfacial separations.

Condition	$\bar{\sigma}$ (MPa)	$\bar{\epsilon}$			$\mathcal{E}$
		$v_f = 0.01$	$v_f = 0.05$	$v_f = 0.10$	
$\max([u]) = \delta_n$	79.370	0.099	0.095	0.090	0.000
$\max([v]) = \delta_t$	122.835	0.154	0.157	0.160	0.076

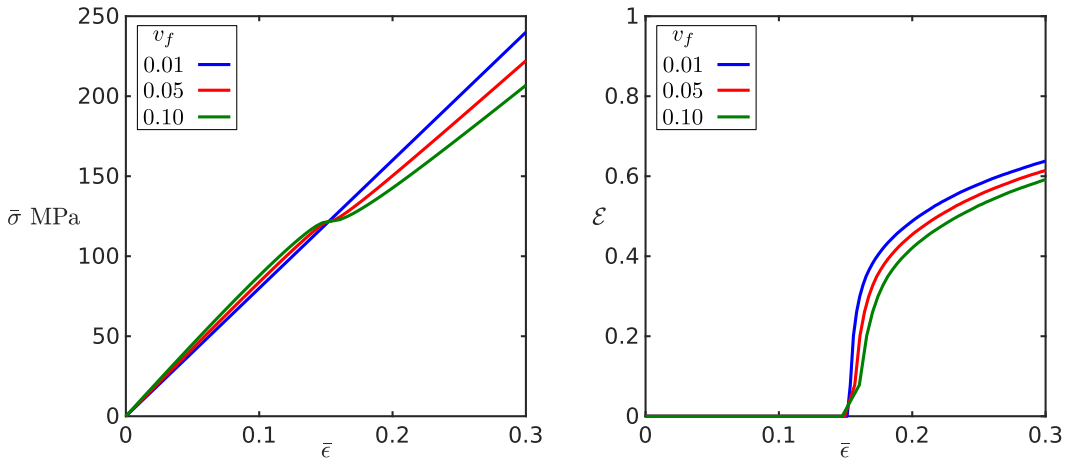

(a) (b)

Fig. 3.7. Effect of volume fraction on well dispersed rigid spherical particle filled IMAC's under uniaxial tension: (a) stress-strain response, and (b) activation response as a function of strain.

angular location will also govern the response since interface separation varies with angle relative to the loading direction.

Our practical objective is that material designers will be able to select their composite following their typical decision criterion and then select an appropriate mechanophore to place at the interface to augment the composite with self-reporting or self-healing capabilities. To this end, we created sample activation maps to succinctly display the zone of useful mechanophores in terms of activation length relative to the debonding length and composite interface strength relative to matrix elastic modulus. These two normalized parameters were found to be the most critical in determining expected mechanophore activation. Further, we showed that this design guideline is nearly independent of loading mode.

The model of an IMAC formulated in this paper is the first step towards modeling a complex material system and the results must be carefully viewed in the context of the target polymer composite. For example, most polymeric matrices have nonlinear aspects of their constitutive behavior, which would in turn affect the debonding mechanics and mechanophore activation in accordance with the modified strain field. Realistic interfaces will have behavior for interfacial shear intermediate to the extremal cases considered in this work. If the angular overlap of activation and debonding is important then the relation between the normal and shear interfacial strength will have to be measured. Real composites consist of a finite number of particles in a non-infinite matrix. As a step towards more realistic composites we provided predictions for stress and activation as a function of strain for a composite with a low volume fraction of well dispersed spherical filler particles. More generally, neighboring particles

may serve as stress concentrators/relievers depending on their individual properties and proximity. Each of these factors can be accounted for by porting our debond and extensible mechanophore concept into a finite element framework, significantly extending the applicability of the framework presented here.

3.7 Appendix A: Elasticity Solutions

3.7.1 Equibiaxial loading scenario

For the equibiaxial case, with an interphase whose Young's modulus varies according to the powerlaw (Eq. 3.12), displacements can be obtained from [91] under plane stress conditions as:

$$\begin{aligned} u(r) &= r\sigma_{\text{int}}(1-\nu_p)/(E_p) && r < r_p \\ u(r) &= r^{-n/2}\left(A_1 r^{k/2} + A_2 r^{-k/2}\right) && r_p < r \leq r_m \\ u(r) &= C_1 r + C_2/r && r_m \leq r \end{aligned} \tag{3.20}$$

where the index k is given by,

$$k = \sqrt{n^2 + 4(1 - n\nu_m)},$$

and the integration constants A_1, A_2, C_1, C_2 are given by,

$$
\begin{aligned}
A_2 &= \frac{\begin{bmatrix} r_m^{(n+k)/2-1} 2\sigma_{\text{int}}(1-\nu_m^2)(k-n+2) \\ \quad - r_p^{(n+k)/2-1} 4\sigma_\infty(1-\nu_m)(k-n+2\nu_m) \end{bmatrix}}{E(r_p^+)\begin{bmatrix} r_p^{-(n+k)/2-1} r_m^{(n+k)/2-1}(-k-n+2\nu_m)(k-n+2) \\ \quad - r_p^{(-n+k)/2-1} r_m^{(n-k)/2-1}(k-n+2\nu_m)(-k-n+2) \end{bmatrix}}, \\
A_1 &= \frac{4r_p^n\sigma_\infty(1-\nu_m) - E(r_p^+)A_2 r_m^{(n-k)/2-1}(-k-n-2)}{E(r_p^+)r_m^{(n+k)/2-1}(k-n+2)}, \\
C_1 &= \frac{\sigma_\infty(1-\nu_m)}{E_m}, \\
C_2 &= \frac{r_m^2(\sigma_\infty - \sigma_{\text{int1}})(1+\nu_m)}{E_m} \\
\sigma_{\text{int1}} &= \frac{E(r_p^+)r_m^{n/2-1}}{2r_p^n(1-\nu_m^2)}\begin{bmatrix} A_1 r_m^{k/2}(k-n+2\nu_m) \\ \quad + A_2 r_m^{-k/2}(-k-n+2\nu_m) \end{bmatrix}.
\end{aligned}
\tag{3.21}
$$

By expanding out $[u] = u(r_p^+) - u(r_p^-)$, substituting Eq. 3.20 and Eq. 3.7 we get a nonlinear equation in terms of $[u]$ which we solve using the MATLAB numerical root finding technique 'fsolve'. All this work can be adjusted for the case of plane strain by replacing E and ν with $\frac{E}{1-\nu^2}$ and $\frac{\nu}{1-\nu}$ respectively.

3.7.2 Generic loading scenario

The solution in plane strain conditions for the full-slip condition is detailed in [38, 36] while the generic interfacial shear case is discussed in [37]. For a remote stress of $\boldsymbol{\sigma}_\infty$ the displacement field $\mathbf{u}(\mathbf{r})$ at position $\mathbf{r}$ can be found by reducing Eq. 3.5 to

$$
\begin{aligned}
\mathbf{u}(\mathbf{r}) &= \boldsymbol{\varepsilon}_\infty \mathbf{r} + \int_{\theta'} \mathbf{G}_m(\mathbf{r},\theta')\mathbf{T}_m d\theta' \qquad |\mathbf{r}| \geq r_p \\
\mathbf{u}(\mathbf{r}) &= \int_{\theta'} \mathbf{G}_p(\mathbf{r},\theta')\mathbf{T}_p d\theta' \qquad |\mathbf{r}| \leq r_p
\end{aligned}
\tag{3.22}
$$

The Green's functions $\mathbf{G}_m, \mathbf{G}_p$ are the displacement fields caused by a point load acting at a point on circular surface in the matrix and particle respectively. These are given by,

$$\begin{aligned}\mathbf{G}_p(\mathbf{r},\theta') = &- r_p\left[\frac{\lambda_p+2\mu_p}{2\pi\mu_p\left(\lambda_p+\mu_p\right)}\log\left(\frac{l}{r_p}\right)+\frac{1}{4\pi\mu_p}\right]\mathbf{I}\\ &- r_p\frac{1}{2\pi\mu_p}\boldsymbol{\chi}\mathbf{l}\otimes\boldsymbol{\chi}\mathbf{l}+r_p\frac{1}{2\pi\left(\lambda_p+\mu_p\right)}\Theta^{-}\boldsymbol{\chi}-\frac{1}{4\pi\left(\lambda_p+\mu_p\right)}\mathbf{r}\otimes\mathbf{n} \quad (3.23)\\ \mathbf{G}_m(\mathbf{r},\theta') = &- r_p\left[\frac{\lambda_m+2\mu_m}{2\pi\mu_m\left(\lambda_m+\mu_m\right)}\log\left(\frac{l}{r_p}\right)+\frac{1}{4\pi\mu_m}\right]\mathbf{I}\\ &- r_p\frac{1}{2\pi\mu_m}\boldsymbol{\chi}\mathbf{l}\otimes\boldsymbol{\chi}\mathbf{l}+r_p\frac{1}{2\pi\left(\lambda_m+\mu_m\right)}\Theta^{+}\boldsymbol{\chi}+\frac{r_p^2}{4\pi\mu_m}\frac{\mathbf{r}}{r^2}\otimes\mathbf{n}. \quad (3.24)\end{aligned}$$

where, the geometric parameters are shown in Fig. 3.8, $\boldsymbol{\chi}$ is given by

$$\boldsymbol{\chi} = \begin{bmatrix} 0 & 1 \\ -1 & 0 \end{bmatrix} \quad (3.25)$$

and λ_m, μ_m are the Lame parameters for the matrix and λ_p, μ_p are the Lame parameters for the particle.

The kinematic constraint results in the following integral equation

$$[\mathbf{u}](\theta) = r_p\mathbf{R}_\theta\boldsymbol{\mathcal{A}}\,\mathbf{r}\big|_{r_p,\theta} + r_p\int_{\theta'}\boldsymbol{\mathcal{K}}(\theta,\theta')\boldsymbol{\sigma}_{\text{int}}\left([\mathbf{u}](\theta')\right)d\theta' \quad (3.26)$$

where the Kernel $\mathcal{K}$ is given by,

$$\boldsymbol{\mathcal{K}}(\theta,\theta') = -\frac{1}{r_p}\left(\mathbf{G}^{+}\left(\mathbf{r}\big|_{r=r_p},\theta'\right)+\mathbf{G}^{-}\left(\mathbf{r}\big|_{r=r_p},\theta'\right)\right) \quad (3.27)$$

and can be expanded out as

$$\begin{aligned}
\begin{bmatrix} \mathcal{K}_{rr} & \mathcal{K}_{r\theta} \\ \mathcal{K}_{\theta r} & \mathcal{K}_{\theta\theta} \end{bmatrix} =& \left[\frac{\lambda_m + 2\mu_m}{4\pi\mu_m\left(\lambda_m + \mu_m\right)} + \frac{\lambda_p + 2\mu_p}{4\pi\mu_p\left(\lambda_p + \mu_p\right)}\right] \log(1 - \cos(\psi))\mathbf{R}_\psi \\
&+ \left[\frac{\lambda_p + 2\mu_p}{4\pi\mu_p\left(\lambda_p + \mu_p\right)}\right] \begin{bmatrix} 1 & 0 \\ 0 & 0 \end{bmatrix} \\
&+ \frac{1}{4\pi}\left(\frac{1}{\lambda_m + \mu_m} - \frac{1}{\lambda_p + \mu_p}\right) 2\Theta^- \boldsymbol{\chi}\mathbf{R}_\psi \\
\psi =& \theta - \theta' \\
\mathbf{R}_\psi =& \begin{bmatrix} \cos(\psi) & \sin(\psi) \\ -\sin(\psi) & \cos(\psi) \end{bmatrix} \\
\mathbf{R}_\theta =& \begin{bmatrix} \cos(\theta) & \sin(\theta) \\ -\sin(\theta) & \cos(\theta) \end{bmatrix} \\
2\Theta^- =& \begin{cases} \psi - \pi & 0 \leq \psi \leq 2\pi \\ \psi + \pi & -2\pi \leq \psi \leq 0. \end{cases}
\end{aligned}$$

The components of $\boldsymbol{\mathcal{A}}$ are given through the equations

$$\begin{aligned}
2\mu_m\left(\lambda_m + \mu_m\right)\mathcal{A}_{11} =& \left(\lambda_m + 2\mu_m\right)\left(\lambda_m + 3\mu_m\right)\varepsilon_{\infty 11} \\
&+ \left(\lambda_m - \mu_m\right)\left(\lambda_m + 2\mu_m\right)\varepsilon_{\infty 22} \\
\left(\lambda_m + \mu_m\right)\mathcal{A}_{12} =& \left(\lambda_m + \mu_m\right)\mathcal{A}_{21} \\
=& 2\left(\lambda_m + 2\mu_m\right)\varepsilon_{\infty 12} \\
2\mu_m\left(\lambda_m + \mu_m\right)\mathcal{A}_{22} =& \left(\lambda_m + 2\mu_m\right)\left(\lambda_m + 3\mu_m\right)\varepsilon_{\infty 22} \\
&+ \left(\lambda_m - \mu_m\right)\left(\lambda_m + 2\mu_m\right)\varepsilon_{\infty 11}.
\end{aligned} \tag{3.28}$$

The Fourier expansion of the $\mathcal{K}$ is given by

$$\begin{aligned}
\mathcal{K}_{rr} &= \mathcal{K}_{\theta\theta} = \sum_{i=1} \xi_i(\theta)\,\xi_i(\theta')\,\frac{1}{\lambda_i} \\
\mathcal{K}_{r\theta} &= -\mathcal{K}_{\theta r} = \sum_{i=1} \xi_{2i+1}(\theta)\,\xi_{2i}(\theta')\,\frac{1}{\gamma_{2i}} - \xi_{2i}(\theta)\,\xi_{2i+1}(\theta')\,\frac{1}{\gamma_{2i+1}} \\
\xi_1 &= \frac{1}{\sqrt{2\pi}}, \xi_{2i} = \frac{\cos(i\theta)}{\sqrt{\pi}}, \xi_{2i+1} = \frac{\sin(i\theta)}{\sqrt{\pi}} \\
\lambda_1 &= \frac{1}{A}, \lambda_2 = \lambda_3 = \frac{1}{B}, \lambda_{2i} = \lambda_{2i+1} = -\frac{i^2-1}{(iC_1 + C_2)} \\
\gamma_2 &= \gamma_3 = -\frac{1}{B}, \gamma_{2i} = \gamma_{2i+1} = -\frac{i^2-1}{(C_1 + iC_2)}
\end{aligned} \tag{3.29}$$

where,

$$\begin{aligned}
A = -\frac{1}{2}\left(\frac{1}{\mu_m} + \frac{1}{\lambda_p + \mu_p}\right) \quad B &= -\frac{1}{8}\left(\frac{1}{\mu_p}\left(\frac{\lambda_p + 3\mu_p}{\lambda_p + \mu_p}\right) + \frac{1}{\mu_m}\right) \\
C_1 &= \frac{1}{2}\left(\frac{\lambda_m + 2\mu_m}{\mu_m(\lambda_m + \mu_m)} + \frac{\lambda_p + 2\mu_p}{\mu_p(\lambda_p + \mu_p)}\right) \\
C_2 &= \frac{1}{2}\left(\frac{1}{\lambda_m + \mu_m} - \frac{1}{\lambda_p + \mu_p}\right).
\end{aligned} \tag{3.30}$$

When we have a full-slip scenario the cohesive zone traction vector is,

$$\boldsymbol{\sigma}_{\text{int}} = \begin{pmatrix} \sigma_{\text{int}} \\ 0 \end{pmatrix} \tag{3.31}$$

where σ_{int} is found from the radial interfacial separation $[u]$ as a function of θ' using Eqs. 3.7,3.8. This simplifies the integral equation Eq. 3.26 to:

$$\begin{aligned}
\frac{[u](\theta)}{r_p} =& \sqrt{2\pi}\frac{(\mathcal{A}_{11} + \mathcal{A}_{22})}{2} + \sqrt{2\pi}\frac{(\mathcal{A}_{11} - \mathcal{A}_{22})}{2}\xi_4(\theta) + \sqrt{2\pi}\mathcal{A}_{12}\xi_5 \\
&+ \sum_{i=1}\frac{1}{\lambda_i}\xi_i(\theta)\int_{\theta'}\xi_i(\theta')\sigma_{\text{int}}([u](\theta'))\,d\theta'
\end{aligned} \tag{3.32}$$

Also in the full-slip condition the equilibrium condition Eq. 3.4 is trivially satisfied, and we are left just with Eq. 3.3, which translates to

$$\begin{aligned}
\int_{\theta'}\xi_2(\theta')\sigma_{\text{int}}([u](\theta'))\,d\theta' = 0 \\
\int_{\theta'}\xi_3(\theta')\sigma_{\text{int}}([u](\theta'))\,d\theta' = 0.
\end{aligned} \tag{3.33}$$

By expressing $[u]$ in terms of the Fourier basis

$$[u](\theta) = \sum_{i=1} \hat{u}_i \xi_i(\theta) \tag{3.34}$$

we can reduce Eqs. 3.32, 3.33 to a set of algebraic equations using the orthogonality of the Fourier basis functions as,

$$\begin{aligned}
\frac{\hat{u}_1}{r_p} &= \sqrt{2\pi}\left(\frac{\mathcal{A}_{11}+\mathcal{A}_{22}}{2}\right) + \frac{1}{\lambda_1}\int_{\theta'} \xi_1 \sigma_{\text{int}}([u](\theta'))d\theta' \\
\hat{u}_2 &= \hat{u}_3 = 0 \\
\frac{\hat{u}_4}{r_p} &= \sqrt{2\pi}\left(\frac{\mathcal{A}_{11}-\mathcal{A}_{22}}{2}\right) + \frac{1}{\lambda_4}\int_{\theta'} \xi_4 \sigma_{\text{int}}([u](\theta'))d\theta' \\
\frac{\hat{u}_5}{r_p} &= \sqrt{2\pi}\mathcal{A}_{12} + \frac{1}{\lambda_5}\int_{\theta'} \xi_5 \sigma_{\text{int}}([u](\theta'))d\theta' \\
\frac{\hat{u}_i}{r_p} &= \frac{1}{\lambda_i}\int_{\theta'} \xi_i \sigma_{\text{int}}([u](\theta'))d\theta' \quad i = 6, 7, \cdots .
\end{aligned} \tag{3.35}$$

We truncate the number of Fourier modes at 35 where the relative error by introducing one additional mode is less than 0.01% . The solutions for these coefficients are found using a root finding numerical technique 'fsolve' in MATLAB.

We reduce the generic interfacial condition presented in Levy [37], for the specific case of the no-slip condition by setting the tangential interfacial separation $[v] = 0$. The cohesive zone traction vector is denoted by

$$\boldsymbol{\sigma}_{\text{int}} = \begin{pmatrix} \sigma_{\text{int}} \\ \\ \tau_{\text{int}} \end{pmatrix} \tag{3.36}$$

where τ_{int} needs to be found. The integral equation Eq. 3.26 can be reduced to two equations one for the radial interfacial separation $[u]$ and the other for the

tangential interfacial separation $[v]$

$$\begin{aligned}\frac{1}{r_p}[u](\theta) =& \sqrt{2\pi}\frac{(\mathcal{A}_{11}+\mathcal{A}_{22})}{2} + \sqrt{2\pi}\frac{(\mathcal{A}_{11}-\mathcal{A}_{22})}{2}\xi_4(\theta) + \sqrt{2\pi}\mathcal{A}_{12}\xi_5 \\ &+ \sum_{i=1}\frac{1}{\lambda_i}\xi_i(\theta)\int_{\theta'}\xi_i(\theta')\sigma_{\text{int}}([u](\theta'))\,d\theta' \\ &+ \sum_{i=1}\frac{1}{\gamma_{2i}}\xi_{2i+1}(\theta)\int_{\theta'}\xi_{2i}(\theta')\,\tau_{\text{int}}d\theta' \\ &- \sum_{i=1}\frac{1}{\gamma_{2i+1}}\xi_{2i}(\theta)\int_{\theta'}\xi_{2i+1}(\theta')\,\tau_{\text{int}}d\theta' \end{aligned} \tag{3.37}$$

$$\begin{aligned}\frac{1}{r_p}[v](\theta) = 0 =& \sqrt{2\pi}\mathcal{A}_{12}\xi_4(\theta) + \sqrt{2\pi}\frac{(\mathcal{A}_{22}-\mathcal{A}_{11})}{2}\xi_5(\theta) + \\ &+ \sum_{i=1}\frac{1}{\lambda_i}\xi_i(\theta)\int_{\theta'}\xi_i(\theta')\tau_{\text{int}}d\theta' \\ &- \sum_{i=1}\frac{1}{\gamma_{2i}}\xi_{2i+1}(\theta)\int_{\theta'}\xi_{2i}(\theta')\,\sigma_{\text{int}}([u](\theta'))\,d\theta' \\ &+ \sum_{i=1}\frac{1}{\gamma_{2i+1}}\xi_{2i}(\theta)\int_{\theta'}\xi_{2i+1}(\theta')\,\sigma_{\text{int}}([u](\theta'))\,d\theta'. \end{aligned} \tag{3.38}$$

The equilibrium equations reduce to

$$\begin{aligned}\int_{\theta'}\xi_2(\theta')\sigma_{\text{int}}([u](\theta'))\,d\theta' + \int_{\theta'}\xi_3(\theta')\tau_{\text{int}}d\theta' &= 0 \\ -\int_{\theta'}\xi_3(\theta')\sigma_{\text{int}}([u](\theta'))\,d\theta' + \int_{\theta'}\xi_2(\theta')\tau_{\text{int}}d\theta' &= 0 \\ \int_{\theta'}\tau_{\text{int}}\xi_1(\theta')d\theta' &= 0. \end{aligned} \tag{3.39}$$

Expressing the tangential interfacial traction τ_{int} in terms of the Fourier basis

$$\tau_{\text{int}} = \sum_{i=1}\hat{\tau}_i\xi_i(\theta) \tag{3.40}$$

we can find the Fourier coefficients $\hat{\tau}_i$ in terms of the Fourier coefficients of $[u]$

using the above Eqs. 3.38, 3.39

$$
\begin{aligned}
\hat{\tau}_1 &= 0 \\
\hat{\tau}_2 &= \int_{\theta'} \xi_3(\theta')\sigma_{\text{int}}\left([u]\left(\theta'\right)\right) d\theta' \\
\hat{\tau}_3 &= -\int_{\theta'} \xi_2(\theta')\sigma_{\text{int}}\left([u]\left(\theta'\right)\right) d\theta' \\
\hat{\tau}_4 &= -\frac{\lambda_4}{\gamma_5}\int_{\theta'} \xi_5(\theta')\sigma_{\text{int}}\left([u]\left(\theta'\right)\right) d\theta' - \sqrt{2\pi}\lambda_4\mathcal{A}_{12} \\
\hat{\tau}_5 &= \frac{\lambda_5}{\gamma_4}\int_{\theta'} \xi_4(\theta')\sigma_{\text{int}}\left([u]\left(\theta'\right)\right) d\theta' + \sqrt{2\pi}\lambda_5\frac{\mathcal{A}_{11}-\mathcal{A}_{22}}{2} \\
\hat{\tau}_{2i} &= -\frac{\lambda_{2i}}{\gamma_{2i+1}}\int_{\theta'} \xi_{2i+1}(\theta')\sigma_{\text{int}}\left([u]\left(\theta'\right)\right) d\theta' \quad i = 3, 4, \cdots \\
\hat{\tau}_{2i+1} &= \frac{\lambda_{2i+1}}{\gamma_{2i}}\int_{\theta'} \xi_{2i}(\theta')\sigma_{\text{int}}\left([u]\left(\theta'\right)\right) d\theta' \quad i = 3, 4, \cdots .
\end{aligned} \tag{3.41}
$$

Substituting these back into Eqs. 3.37, 3.39 we get the algebraic equations in terms of the Fourier coefficients of $[u]$ using the orthogonality of the Fourier basis functions as,

$$
\begin{aligned}
\frac{\hat{u}_1}{r_p} &= \sqrt{2\pi}\left(\frac{\mathcal{A}_{11}+\mathcal{A}_{22}}{2}\right) + \frac{1}{\lambda_1}\int_{\theta'} \xi_1(\theta')\sigma_{\text{int}}([u]\left(\theta'\right))d\theta' \\
\hat{u}_2 &= \hat{u}_3 = 0 \\
\frac{\hat{u}_4}{r_p} &= \sqrt{2\pi}\left(1-\frac{\lambda_5}{\gamma_5}\right)\left(\frac{\mathcal{A}_{11}-\mathcal{A}_{22}}{2}\right) + \left(\frac{1}{\lambda_4}-\frac{\lambda_5}{\gamma_5\gamma_4}\right)\int_{\theta'} \xi_4(\theta')\sigma_{\text{int}}([u]\left(\theta'\right))d\theta' \\
\frac{\hat{u}_5}{r_p} &= \sqrt{2\pi}\left(1-\frac{\lambda_4}{\gamma_4}\right)\mathcal{A}_{12} + \left(\frac{1}{\lambda_5}-\frac{\lambda_4}{\gamma_5\gamma_4}\right)\int_{\theta'} \xi_5(\theta')\sigma_{\text{int}}([u]\left(\theta'\right))d\theta' \\
\frac{\hat{u}_{2i}}{r_p} &= \left(\frac{1}{\lambda_{2i}}-\frac{\lambda_{2i+1}}{\gamma_{2i+1}\gamma_{2i}}\right)\int_{\theta'} \xi_{2i}(\theta')\sigma_{\text{int}}([u]\left(\theta'\right))d\theta' \quad i = 3, 4, \cdots \\
\frac{\hat{u}_{2i+1}}{r_p} &= \left(\frac{1}{\lambda_{2i+1}}-\frac{\lambda_{2i}}{\gamma_{2i+1}\gamma_{2i}}\right)\int_{\theta'} \xi_{2i+1}(\theta')\sigma_{\text{int}}([u]\left(\theta'\right))d\theta' \quad i = 3, 4, \cdots .
\end{aligned} \tag{3.42}
$$

Like the full-slip condition, here too we truncate the number of Fourier modes at 35 where the relative error by introducing one additional mode is less than 0.01% . The solutions for these coefficients are found using the root finding numerical technique 'fsolve' in MATLAB.

Once we have the Fourier coefficients for both the interface conditions $\hat{u}_i$, we can compute $\boldsymbol{\sigma}_{\text{int}}$ and substitute this into Eq. 3.22 to get displacements at any location.

3.7.3 IMAC with spherical filler particles

We focus on an IMAC in uniaxial tensile loading with a dilute, dispersed set of rigid spherical filler particles occupying a volume fraction of v_f. A detailed solution of this can be inferred from [74] and we summarize the procedure here. A representative volume element (RVE) with a single particle in an infinite matrix subjected to uniaxial remote stress equaling the average stress experienced by the composite $\bar{\sigma}$ is considered. The solution for the RVE follows Eqs. 3.2-3.4 and the displacement field detailed in [47]. The solution takes advantage of the fact that the loading is rotationally symmetric about the axis of loading.

The matrix displacement field is given by the series expansion:

$$\begin{aligned} u &= \sum_{n=1} \left[\frac{A_n}{r^n} n \left(n + 3 - \frac{4}{\nu_m} \right) - B_n \frac{(n+1)}{r^{n+2}} \right] P_n(\mu) \\ v &= \sum_{n=1} \left[\frac{A_n}{r^n} \left(-n + 4 - \frac{4}{\nu_m} \right) + \frac{B_n}{r^{n+2}} \right] \frac{dP_n(\mu)}{d\theta} \end{aligned} \tag{3.43}$$

where $\mu = cos(\theta)$ and $P_n(\mu)$ refers to Lengendre polynomials of the first kind expanded on μ. A_n, B_n are constants that can be found as follows.

$$\begin{aligned} A_1 &= 0 \\ B_1 &= -\frac{\bar{\sigma} r_p^3}{12 G_m} + \frac{\sigma_1 r_p^3}{4 G_m} \end{aligned} \tag{3.44}$$

and for $n > 1$

$$\begin{pmatrix} A_n \\ B_n \end{pmatrix} = \begin{pmatrix} a_n \\ b_n \end{pmatrix} + \frac{1}{2G_m} \begin{pmatrix} -\frac{(n-1)((n-1)(n+2)-2\nu_m)}{r_p^n} & \frac{n(n+1)}{r_p^(n+2)} \\ \frac{(n-1)^2-2+2\nu_m}{r_p^n} & -\frac{n+1}{r_p^{n+2}} \end{pmatrix}^{-1} \begin{pmatrix} \sigma_n \\ \tau_n \end{pmatrix}$$

$$\begin{aligned} a_3 &= \frac{5\bar{\sigma} r_p^3}{12G_m(7-5\nu_m)} \\ b_3 &= \frac{\bar{\sigma} r_p^5}{2G_m(7-5\nu_m)} \\ a_n &= b_n = 0 \quad n \neq 3. \end{aligned} \tag{3.45}$$

where, G_m is the shear modulus of the matrix. The quantities σ_n, τ_n are coefficients for the expansion of the interfacial tractions given by,

$$\begin{aligned} \sigma_{\text{int}} &= \sum_{n=1} \sigma_n P_n(\mu) \\ \tau_{\text{int}} &= \sum_{n=1} \tau_n \frac{dP_n(\mu)}{d\theta} \\ \sigma_n &= \frac{2n+1}{2} \int_0^\pi \sigma_{\text{int}} \sin(\theta) P_n(\mu) d\theta \\ \tau_n &= \frac{2n+1}{2n(n+1)} \int_0^\pi \tau_{\text{int}} \sin(\theta) \frac{dP_n(\mu)}{d\theta} d\theta. \end{aligned} \tag{3.46}$$

The interfacial tractions are expressed in terms of interfacial displacements $[u], [v]$ expanded out in series as,

$$\begin{aligned} [u] &= \sum_{n=1} [u_n] P_n(\mu) \\ [v] &= \sum_{n=1} [v_n] \frac{dP_n(\mu)}{d\theta}. \end{aligned} \tag{3.47}$$

Substituting the displacement field from Eq. 3.43 into Eq. 3.2 and setting $\mathbf{u}\left(\boldsymbol{\xi}^-\right) = \mathbf{0}$ as the particle is rigid we get the following nonlinear multivariate algebraic equation,

$$\begin{aligned} \left[\frac{A_n}{r^n} n \left(n + 3 - \frac{4}{\nu_m}\right) - B_n \frac{(n+1)}{r^{n+2}}\right] - [u_n] = 0 \qquad n = 1, 2, \cdots \\ \left[\frac{A_n}{r^n} \left(-n + 4 - \frac{4}{\nu_m}\right) + \frac{B_n}{r^{n+2}}\right] - [v_n] = 0 \qquad n = 1, 2, \cdots . \end{aligned} \tag{3.48}$$

We solve the algebraic equation for $[u_n], [v_n]$ using the MATLAB numerical root finding technique 'fsolve' and truncate the solution to $n = 16$ in the series as any further increase in n results in a relative change of less than 0.01% in the displacement solution. These coefficients provide the displacement field via Eq. 3.43, and can be used for evaluating mechanophore response. The mechanophore orientations bounds $[-\phi_{\max}, \phi_{\max}]$ are identical to those derived in the two-dimensional scenario but in addition it is rotationally symmetric as shown in Fig. 3.9.

The average strain for the IMAC corresponding to average stress of $\bar{\sigma}$ can be found by averaging the strain over the RVE [74] as,

$$\begin{aligned}
\bar{\epsilon} &= \frac{\bar{\sigma}}{E_m} - v_f \left[\frac{\sigma_{\text{p}}}{2G_m} + \frac{\nu_m}{E_m}\sigma_{\text{ph}} - \epsilon_{\text{int}} \right] \\
\sigma_{\text{p}} &= \sigma_1 + \frac{2}{5}\left(\sigma_3 + 3\tau_3\right) \\
\sigma_{\text{ph}} &= 3\sigma_1 \\
\epsilon_{\text{int}} &= \frac{[u_1]}{r_p} + \frac{2\left([u_3] + 3\,[v_3]\right)}{5r_p}.
\end{aligned} \tag{3.49}$$

3.8 Appendix B: Additional Discussion of 2D Uniaxial Results

While the discussion in the main text considered one extremal condition of interfacial shear response to debonding where no-slip was permitted, here we present a detailed discussion of the other extremal condition of full-slip response and compare it with the no-slip response. First we will discuss the interfacial debonding mechanics during uniaxial loading for both the extremal cases. In the no-slip scenario the net interface separation $[D] = [U]$ as $[V] = 0$, and $[D]$ is largest along the loading direction ($\theta = 0^\circ$) as shown in Fig. 3.10a. In contrast

in the full-slip scenario, $[D]$ is largest at non radial angular positions $\theta \approx \pm 45^\circ$ during initial loading and then at $\theta \approx 0^\circ$ as remote load increases and debonding occurs (Fig. 3.10c). The contribution to the initial separation along $\theta \approx \pm 45^\circ$ stems from tangential displacement. The interface separation along $\theta = \pm 90^\circ$ in both scenarios is close to zero. The no-slip condition lowers the magnitude of net interface separation for a given θ and a given remote load in comparison to the case with full-slip. It must be noted that these two interfacial slip conditions are extremal scenarios and typical displacements will lie within these bounds.

Next we will discuss the mechanophore activation for the two extremal cases. In the no-slip scenario, $[D]$ is composed only of radial interfacial displacement $[U]$. Since $[U]$ is maximum along $\theta = 0^\circ$ mechanophore activation is expected to originate along $\theta = 0^\circ$ and eventually spreads to other angles (Fig. 3.10b). Interestingly, in the full-slip scenario, mechanophore activation can originate both along an inclined direction (Fig. 3.10d shows an example)and along the axis of loading (Fig. 3.10e shows an example). The angular location of mechanophores that activate could be important in self-healing systems because mechanophore activation should be proximal to the zone of damage.

Activation maps for uniaxial loading are shown in Fig. 3.11a. We presented the activation map for the no-slip case in Section. 3.4. For the full-slip scenario the bound increases nonlinearly with a marked change in slope as activation shifts from originating along $\theta = 0^\circ$ to originating along an inclined direction as $\Sigma_{\max}$ is increased (Fig. 3.11b). Lastly we also note that if mechanophores are expected to start activation after debond then they will start activation along $\theta = 0^\circ$. For mechanophores to activate during debonding the choice of mechanophores is much larger for the full-slip case than the no-slip

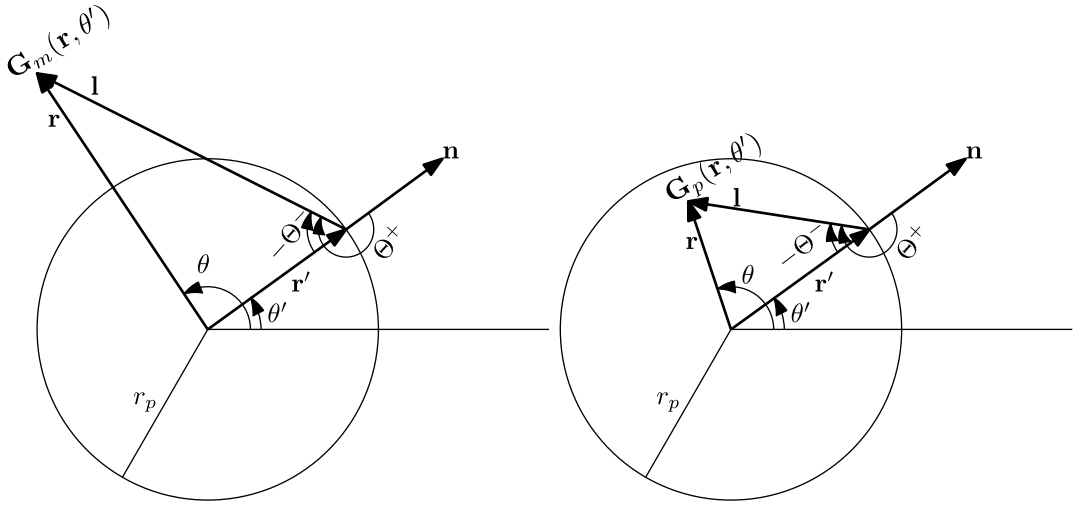

Fig. 3.8. Geometric terms for the Greens functions $\mathbf{G}_m, \mathbf{G}_p$.

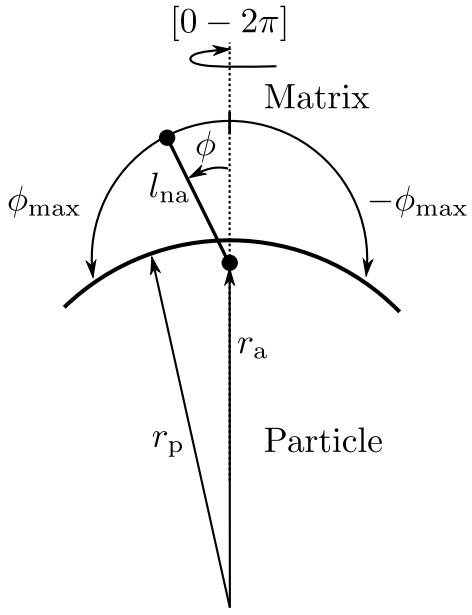

Fig. 3.9. The allowable orientations for mechanophores placement.

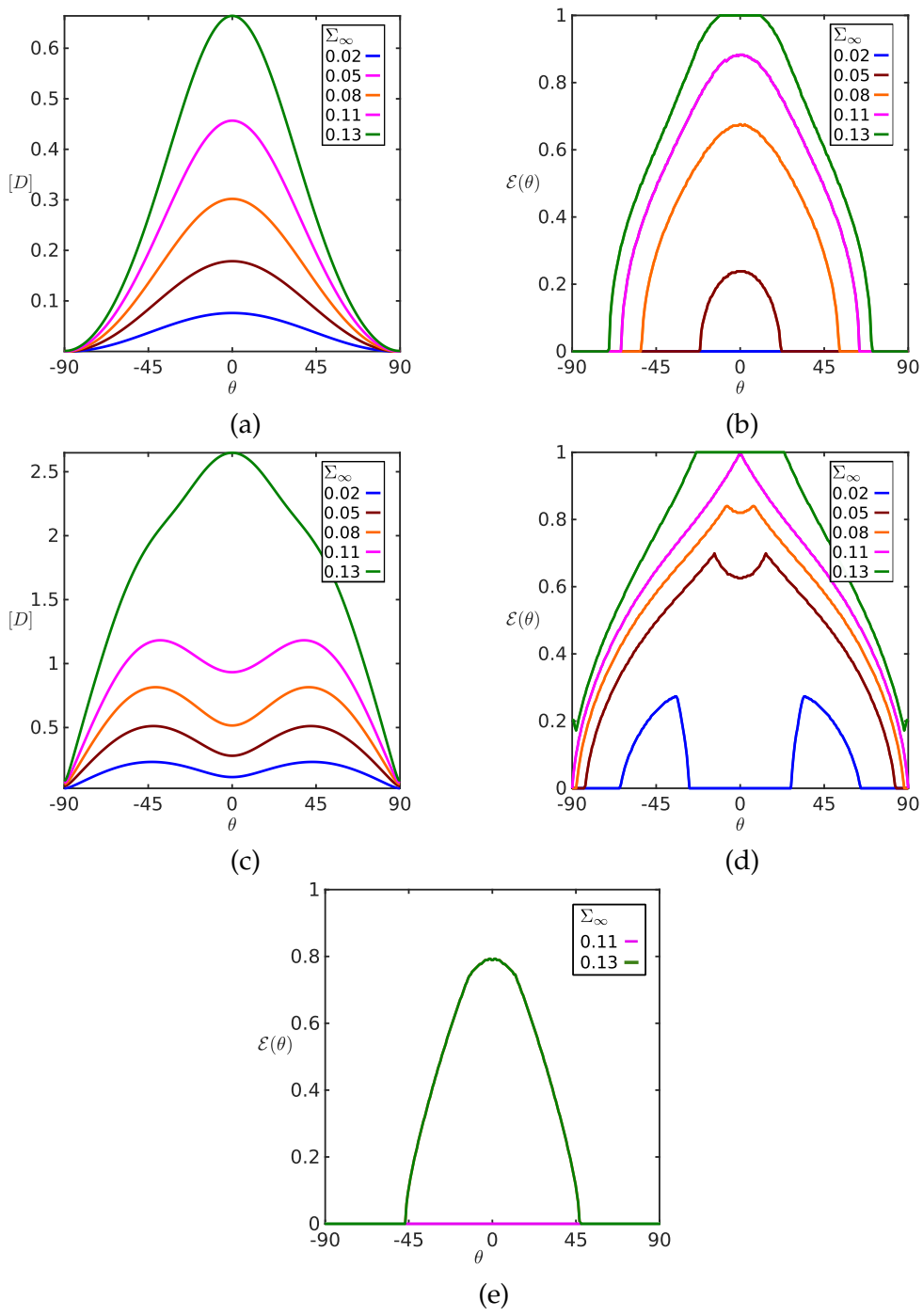

Fig. 3.10. Net interfacial separations $[D]$ and mechanophore activation $\mathcal{E}(\theta)$ considered for the reference composite subjected to different uniaxial loads. (a) $[D]$ for interface with no-slip condition. (c) $[D]$ for interface with full-slip condition. (b) $\mathcal{E}(\theta)$ for interface with no-slip condition with mechanophores of $L_{\text{na}} = 4/3$ and $\Delta L = 0.2$. (d) $\mathcal{E}(\theta)$ for the interface with full-slip condition with mechanophores of $L_{\text{na}} = 4/3$ and $\Delta L = 0.2$. (e) $\mathcal{E}(\theta)$ for the interface with full-slip condition with mechanophores of $L_{\text{na}} = 4/3$ and $\Delta L = 2.0$.

case with the caveat that mechanophores may not activate at the angular location of debond. A mechanophore with length chosen with the equibiaxial equations should perform well for both self-reporting and self-healing IMACs.

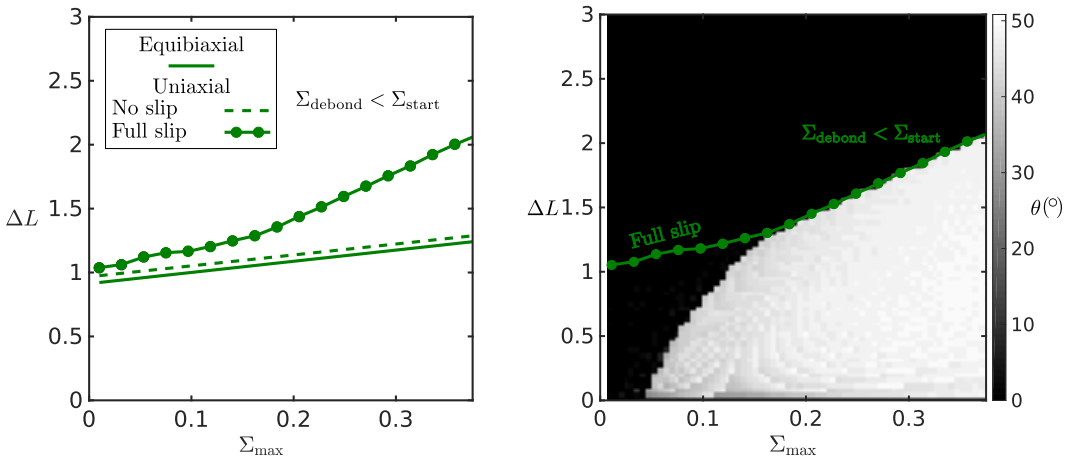

(a) (b)

Fig. 3.11. Influence of stress state on mechanophore selection. (a) Activation map for uniaxial loading with full-slip and no-slip interface conditions compared to the activation map for the equibiaxial load case. (b) For the case of uniaxial loading with full-slip the activation map is overlayed with the angle at which mechanophore activation is expected to start.

CHAPTER 4

RATE OF MECHANOPHORE REACTIONS

4.1 Introduction

In Chapters 2 and 3 we motivate a modeling approach of capturing interfacial mechanophore chemical reactions via length change of the end points of the mechanophore. This approach cleanly couples the mechanical displacements with chemical activation. However, this kinematic approximation is an approximation to the true reaction for the case where there is relatively little interaction between mechanophores and the substrates. On the other hand in bulk mechanochemical systems rates of chemical reactions are coupled to the stress/strain states [71, 72, 81, 73]. Both scenarios involve parameter choices for the reactions that are derived from simulations and experiments all of which were conducted in vacuum, air or solution. However it is not clear whether these parameters are transferable from one environment to another. In this chapter we address this open question by considering how a mechanochemical reaction is influenced by environmental potentials.

Computational studies of mechanochemical reactions of mechanophores in vacuum typically use:(1) Steered Molecular Dynamics (SMD) where an external force is applied and the evolution of the mechanophore configurations and the potential energy surfaces are mapped, [60, 61] or (2) Constrained Geometric optimizations for simulating External Force (CoGEF) [4]. SMD and CoGEF generate force modified potential energy surfaces from which reaction rates can be inferred using Arrhenius activation theory coupled with the Bell's/Eyring's ansatz [2, 13] for energy barriers for varying forces. Recent literature also fo-

cuses on developing techniques to track mechanophore reaction pathways for varying forces in multi dimensions to find accurate energy barriers [65, 66] and in turn reaction rates.

In this work, we capture the basic physics of mechanophores interacting with the environment. We use a simple one-dimensional model with a classical force field (as opposed to quantum) for the mechanophore moving through an atomic lattice. Using a statistical mechanics based transition state theory approach we compute reaction rates.

In this chapter we start by presenting the model system, the theory, and methods for our approach to computing the energy barriers and reaction rates. Then we present and discuss the impact of different environmental features on the force-driven reactions. Finally we will summarize our findings and present future directions.

4.2 Model, Theory, and Methods

4.2.1 Model system

We examine a one-dimensional model of a mechanophore activated through a one-dimensional atomic lattice when subjected to a force. The mechanophore is represented by two beads bonded together, one of the mechanophore beads is held fixed at the origin, and the other bead moves along the x-axis subject to a force F along the x-axis (see Fig. 4.1). The entire system is at an ambient temperature of $T = 300$K.

The mechanophore bond is governed by a double-well potential given by:

$$V_{me}(x) = \left(\frac{x-a}{c}\right)^2 \left(\frac{x-b}{c}\right)^2 + \left(\frac{c}{x}\right)^2 + \left(\frac{c}{a+b-x}\right)^2 \qquad b > a > 0, c > 0 \tag{4.1}$$

where x is the bond length, c is a scaling factor, a and b set the minimum well positions corresponding to the two states of the mechanophore namely the closed/not activated and the open/activated state. The potential reaches the maximum at $\frac{a+b}{2}$ and shoots to infinity at both $x = 0$ and $a + b$. The representative system that we chose and its properties are tabulated in Table 4.1. When force F is applied on the mechanophore the potential gets decreased by the work done i.e., $V_{me}(x) - F(x - a)$. The graph of the potential and the effect of force on it are shown in Fig. 4.2 and the energy barriers for the forward and reverse reaction are tabulated in Table 4.1.

The atomic lattice is modeled as a periodic potential V_p (see Fig. 4.1) given by

$$V_p(x) = A\cos\left(\frac{x+\phi}{\tau}\pi\right) \tag{4.2}$$

where A is the amplitude of the potential, ϕ is the phase shift of the potential, and τ is the period of the potential. We note that the periodic cosine potential can also form the Fourier basis for any other continuous potential.

The net potential energy $V(x)$ of the model system is found by superposing $V_{me}(x) - F(x - a)$ and $V_p(x)$ as:

$$V(x) = V_{me}(x) - F(x-a) + V_p(x) \tag{4.3}$$

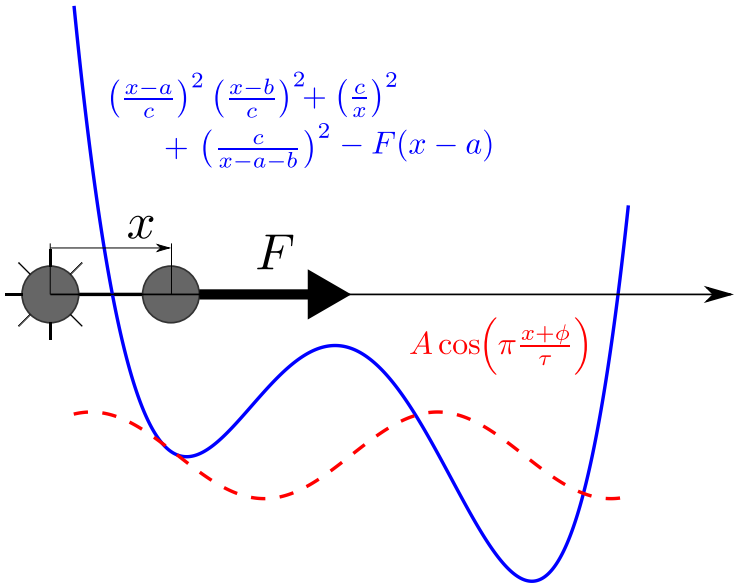

Fig. 4.1. The model system of 1D mechanophore moving activating through an atomic lattice.

Table. 4.1. Representative two bead bonded mechanophore: Mechanophore parameters, potential extrema, and force modified energy barrier

Parameters

Mass g/mol	a Å	b Å	c
1	3	9	1.2

Potential extrema

Type	x Å	V kcal/mol
Minima	3.003	0.178
Maxima	6.000	39.143
Minima	8.997	0.178

Force modified energy barrier

Force (nN)	Energy barrier (kcal/mol)	
	Forward	Reverse
0.0	38.965	38.965
0.5	19.710	62.741
1.0	6.246	91.003

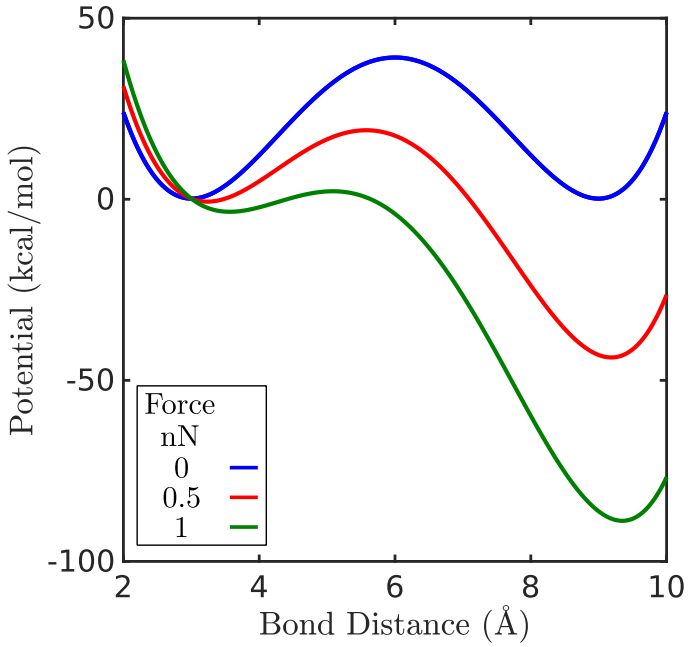

Fig. 4.2. Representative mechanophore's force modified double-well potential

4.2.2 Theory

A chemical reaction is a reconfiguration of atomic positions of reactants to form products. The flux of atomic trajectories leaving the reactants to the products gives the rate of the reaction from reactants to products. Transition state theory assumes that there exists a partitioning surface between the two states in configuration space. The average absolute velocity of the system normal to the dividing surface weighed by the equilibrium probabilities gives the rate of the reaction across that partitioning surface [56]. Among all possible partitioning surfaces we are interested in the one that has the minimum rate as the slowest rate is the rate limiting surface for the reaction.

In configuration space, if $\mathcal{L}_D$ is the separating surface between $\mathcal{R}$ the space of reactants and $\mathcal{P}$ the space of products in configuration space of an NVT system, the rate $k_{rp}\left[\mathcal{L}_D\right]$ at which the system transitions from r to p is expressed as [78],

$$\begin{aligned} k_{rp}\left[\mathcal{L}_D\right] &= \sqrt{\frac{k_B T}{2m\pi}} \mathcal{Z}_{\mathcal{R}}^{-1} \int_{\mathcal{L}_D} e^{-\frac{V(\mathbf{x})}{k_B T}} d\mathbf{x} \\ \mathcal{Z}_{\mathcal{R}} &= \int_r e^{-\frac{V(\mathbf{x})}{k_B T}} d\mathbf{x} \end{aligned} \tag{4.4}$$

where k_B is the Boltzmann's constant, T is the temperature, m is the effective mass and $V(\mathbf{x})$ is the potential energy of the system at configuration x. $\mathcal{Z}_{\mathcal{R}}$ is the partition function over the configuration space of reactants $\mathcal{R}$ in the NVT ensemble. The overall reaction rate of the reaction for the reaction is given by

$$k_{rp} = \min_{\forall \mathcal{L}_D} k_{rp}\left[\mathcal{L}_D\right]. \tag{4.5}$$

4.2.3 Methods

As the model system is one-dimensional the reaction path is along the $\mathbb{X}$-axis and planes $\mathcal{L}_D$ dividing any two regions are all points on the $\mathbb{X}$-axis. The reaction rate $k[x = r]$ for the forward reaction (closed to open state) at any dividing plane at $x = r$ from Eq. 4.4 is given by

$$k[x = r] = \sqrt{\frac{k_B T}{2m\pi}} \frac{e^{-\frac{V(r)}{k_B T}}}{\int_0^r e^{-\frac{V(t)}{k_B T}} dt} \tag{4.6}$$

where the integration over the plane $\mathcal{L}_D$ reduces to just the evaluation of $e^{-\frac{V(r)}{k_B T}}$ at $x = r$. We compute $k[x = r]$ using numerical integration. To find the governing rate of the reaction, we discretize the reaction path into 128 linearly spaced dividing planes and among all the planes considered we choose the one with the least rate as the rate of the reaction k i.e.,

$$k = \min_{\forall r} k[x = r]. \tag{4.7}$$

We discretize the reaction path into 128 linearly spaced dividing planes for this calculation. For every force considered we have to perform these calculations. To compute the variation of the reaction rate with force we vary forces from $0 - 1$nN using 128 linearly spaced samples.

4.3 Results and Discussion

The mechanophore in the absence of the lattice will be our reference system. For the reference system the rate of the mechanophore reaction initially increases exponentially with increase in applied force (see reference curve in Fig. 4.3).

This exponential increase is exactly what we might expect from Bell's ansatz [2] which postulates that the forces decreases the energy barrier of the reaction ΔV by the work done $(F\Delta x)$ and in turn the rate of the reaction increases exponentially with increase in force as,

$$k \propto e^{-\frac{\Delta V - F\Delta x}{k_B T}}. \tag{4.8}$$

When the force reaches the critical force at which the energy barrier for the reaction becomes zero, also known as barrier breakdown point, (BBP) [66] the reaction rate changes slope (see reference curve in Fig. 4.3) as the potential is dominated by the work done. This BPP is given by,

$$\begin{aligned} \frac{d^2 V_{me}}{dx^2} = 0 \qquad & x < \frac{(a+b)}{2} \\ F = 1.391 \text{ nN} \qquad & x = 4.269\text{Å}. \end{aligned} \tag{4.9}$$

This change in slope cannot be explained by the Bell's approach and must be evaluated through Eq. 4.6. In subsequent paragraphs we will discuss the effects of each of the three physically relevant lattice potential parameters (ϕ,τ,A) on the mechanophore reactions.

The phase shift of the lattice potential ϕ determines where on the lattice the mechanophore is localized. Phase plays an important role in determining whether the potentials add up constructively i.e., the rising portion of the double-well matches the rising portion of the lattice potential or destructively i.e., the rising portion of the double-well matches the falling portion of the lattice potential. We illustrate the importance of phase with three lattice potentials: $\tau = 3$Å, $A = 10$ kcal/mol and $\phi = 0$Å ,1Å, 3Å (see Fig. 4.3). The period of all the potentials approximately matches the spacing between the extrema of the double-well. The potential with $\phi = 0$Å constructively adds up with the double-well, increasing the energy barrier. We see the constructive effect reflected as a

reduction in rate of the mechanophore reaction in comparison with the reference rate. The reaction rate differs by nearly ten orders of magnitude for forces less than 1 nN. Also, the BBP is shifted to larger forces for this lattice potential. We can see the opposite effect for the potential with $\phi = 3$Å that has destructive addition. The cases $\phi = 0, 3$Å are extreme scenarios and other phases will result in regions of partial constructive and destructive addition with the double-well. $\phi = 1$Å is shown here to demonstrate intermediate behavior — it has rates that are higher than the reference case for low forces and lower than the reference case for high forces.

The period of the lattice potential is indicative of the spacing of the lattice, smaller periods imply a closely spaced lattice and larger periods imply a widely spaced lattice. If the period of the lattice potential is larger than the distance between the extremums of the double-well potential the extremums shift position and change magnitude. On the other hand if the period of the lattice potential is smaller than the distance between the extremums of the double-well potential, there could be shifts in extremum positions, changes in barrier magnitudes, or even additional extremums marking the presence of metastable states. We illustrate these effects by considering two lattice potentials with $A = 10$kcal/mol, $\phi = 1.5$Å and $\tau = 1.5$Å, 4.5Å. For the case of $\tau = 1.5$Å a metastable state exists (see Fig. 4.4a) and the rate limiting step is to reach the metastable state from the closed state of the mechanophore (see Fig. 4.4b). With increase in force, the energy barrier to transition from the metastable state to the open state of the mechanophore decreases faster than the energy barrier to transition from the closed to the metastable state as it is farther from the closed sate. For the case of $\tau = 4.5$Å the extremums are slightly shifted and the magnitudes are modified (see Fig. 4.4a) and only one maximum exists and limits the rate of the reaction

(see Fig. 4.4b). In both these scenarios the rate of the reaction decreases for a given force relative to the reference scenario as the lattice potentials end up increasing the energy barrier relative to the reference case.

The amplitude of the lattice potential physically represent the strength of interaction between particles in the environment and the mechanophore. This could be brought about by the proximity of the environmental particles or strong interactions like polarization, and ionic charges. The larger the amplitude the greater the amplification of environmental effects: shift and change in magnitudes of the extremums and increased stability of any metastable state. We demonstrate this amplification through four cases: $\phi = \tau = 1.5$Å and $\phi = \tau = 3$Å with amplitudes $A = 10$, 15kcal/mol. Considering $\phi = \tau = 3$Å we can infer that the lattice potential adds destructively with the double-well potential, lowering the energy barrier for the mechanochemical reaction. With increase in amplitude the energy barrier decreases further (see Fig. 4.5a). This decrease in energy barrier is reflected in the increase in rate of the reaction for a given force (see Fig. 4.5b). Considering $\phi = \tau = 1.5$Å the addition produces a metastable state. With increase in amplitude a larger energy barrier is required to leave the metastable state to reach the open mechanophore state, thereby making the metastable state more stable (see Fig. 4.5a). The increase in energy barrier to reach the metastable state lowers the reaction rate for a given applied force (see Fig. 4.5b).

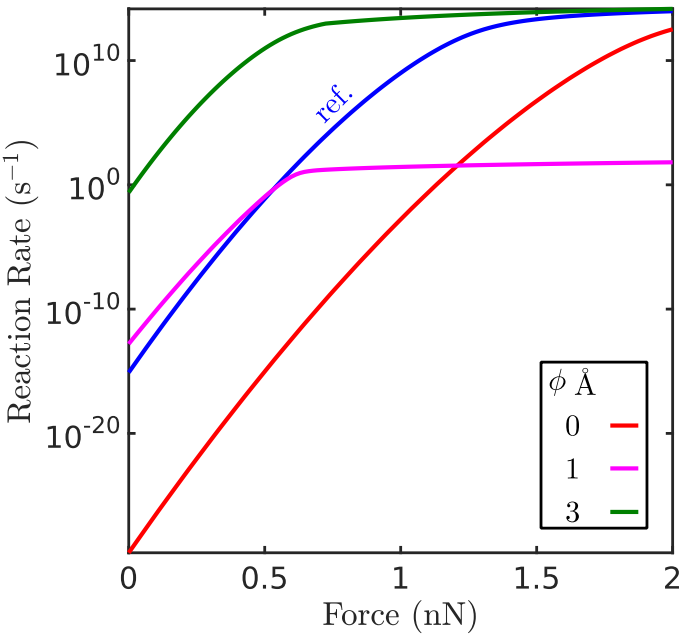

Fig. 4.3. Illustrative examples of the impact that the phase of the lattice potential can have on the rate of the mechanochemical reaction. All the lattice potentials used here have $A = 10$kcal/mol, $\tau = 3$Å.

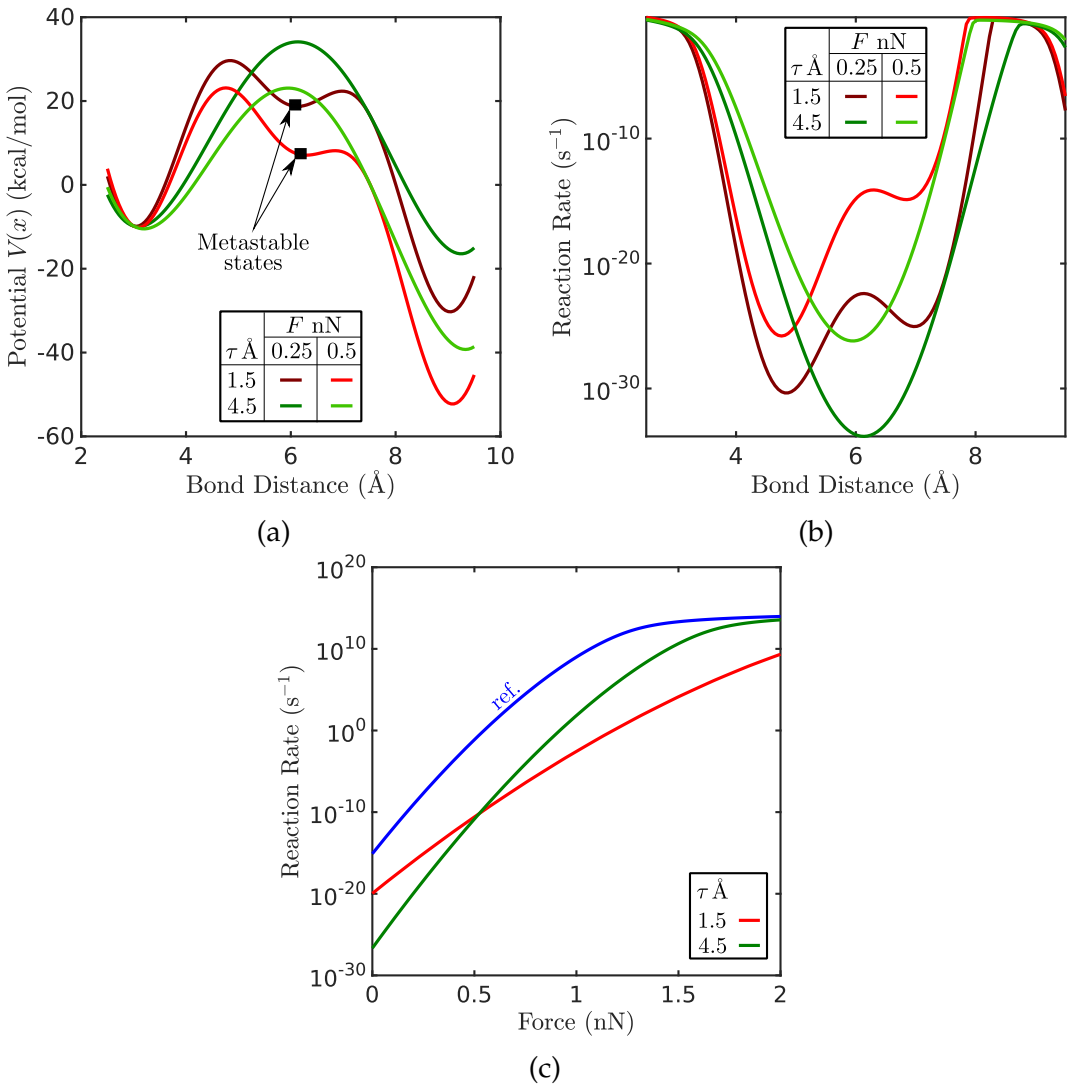

Fig. 4.4. Illustrative examples showing impact of period of the lattice potential: (a) Force modified potential energy surfaces.(b) Reaction rate as function of the bond distance. The minimum of each graph represents the rate limiting step and is considered as the rate of the reaction. (c) The rate of the reaction as a function of the applied force.

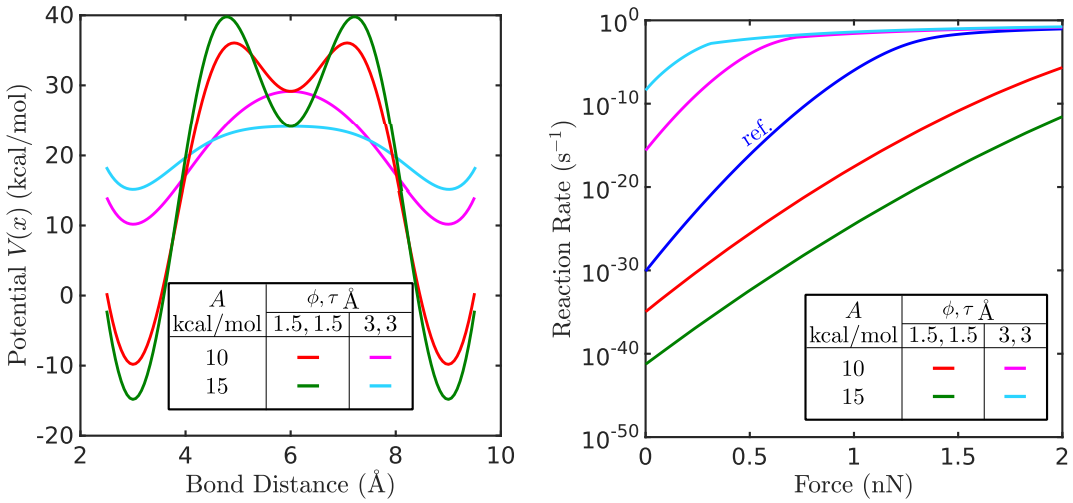

(a) (b)

Fig. 4.5. Illustrative examples showing impact of amplitude of the lattice potential: (a) Force modified potential energy surfaces. (b) Rate of the reaction as a function of the applied force.

4.4 Summary and Future Work

The simple one-dimensional system considered in this chapter shows two major effects of how mechanochemical reactions can be influenced by the environment - constructive/destructive addition to mechanophore potential energy surface and presence of metastable states. This change in potential energy landscape in turn affects the mechanochemical reaction rates. It also shows that the parameters defining the mechanophore reaction rate inferred from one environmental condition are not directly applicable for another environment unless augmented with environmental influencing potentials like in a molecular dynamics setup.

There are other complex scenarios that cannot be captured through a one-dimensional setup such as the impact of directionality of applied force, a metastable state becoming a stable state with applied force and different/multiple reaction pathways opening up with applied force. To analyse such systems one can compute the reaction pathway and then compute the rate of the reaction. In the literature, a popular approach to finding reaction pathways using molecular dynamics simulations is the Finite Temperature String (FTS) [83, 51, 79]. This approach involves dividing the configuration space into a set of voronoi cells, the centers of which are called as images. The collection of images describe the reaction pathway called as the string. The FTS method gives a recipe to converge to a string that approximates the reaction pathway using molecular dynamics simulation started at each image. From the converged string reaction pathways can be estimated by computing the residence probabilities in each voronoi cell.

Furthermore, in general a precise atomic placement of mechanophore in an

environment is quite difficult as the environment and the mechanophore influence one another. So, an ensemble of mechanophores can be considered in an environment and an ensemble averaged reaction rate for a given force can be evaluated.

CHAPTER 5

CONCLUSION AND FUTURE DIRECTIONS

In this dissertation we investigated interfaces augmented with force triggered chemical units (mechanophores) through multiscale modeling. Such mechanophore augmented interfaces are targeted towards self-healing or self-reporting polymer composites that fail through debonding; we refer to these composites as Interfacial Mechanophore Augmented Composites (IMACs).

We first explored the molecular scale in Chapter 2 by studying interfacial mechanophore activation using a molecular dynamics (MD) model of an idealized interface with covalently bonded mechanophores subjected to interfacial shear. Mutual mechanophore interactions were neglected in this idealized construct. The mechanophore attachments to the substrates of the interface have to be capable of withstanding the force required to effect mechanophore activation. If the attachments are strong enough, and nonbonded substrate-mechanophore and substrate-substrate interactions are negligible, then mechanophore activation evolves with respect to interfacial displacement and in accordance with the mechanophore orientation with respect to the shearing direction. Nonbonded interactions alter interface geometry and the strength of the mechanophore attachment required to effect activation.

In chapter 3 we developed a framework for modeling mechanophore activation of IMACs due to macroscopic loading. The framework used an extensible link model that had two lengths corresponding to the two states of the mechanochemical reaction - the smaller length represented the not activated state and the larger length represented the activated state. The extensible link mechanophore does not exert any tractions on the interface and deforms with

its attachment points on the composite. We demonstrated this framework in two classical mechanics model of IMACs: a circular filler particle in an infinite matrix and a disperse dilute volume fraction of spherical particles in a three dimensional matrix. The materials were linear elastic while the interface was governed by a cohesive zone law. Mechanophore activation is governed by mechanophore length scales relative to critical interfacial debonding length scales, interfacial strength relative to matrix stiffness, particle size, matrix Poisson's ratio, type and magnitude of loading and volume fraction of particles. Impact of each of these was analyzed in this dissertation. We developed design maps over two non-dimensional parameters: mechanophore length change required to activate relative to critical interface separation and interfacial strength relative to matrix stiffness, to select mechanophores that are promising for augmenting polymer composites with effective self-healing or self-reporting functionality.

Finally, we took a closer look at our inspiration for the MD model of the mechanophore that stems from quantum simulations in vacuum. In Chapter 4 we sought to understand its validity in any other environment. We did this by studying the rates of a one-dimensional system of a mechanophore activating through a superimposed lattice potential. The mechanophore potential energy surface changes by constructive/destructive superposition, changing magnitudes and location of potential energy extremas, and creating new extremas (metastable states). The rates of mechanochemical reactions reflect the change in potential energy surface and transferability to different environments depend upon the magnitude of the interactions. If amplitudes are low then the influence on rates of reactions can be neglected, but if amplitudes are high then the influence is significant and one must account for the environment.

There is ample scope for future extensions as this dissertation is only a first step towards modeling mechanophore activation in interfaces. The first portion of our work on MD simulations of mechanophore activation in interfaces can be extended for polymeric interfaces to capture the effects of the altered mobility at the interface, surface roughness. The second portion of our work on connecting mechanophore activation with continuum stress states in IMACs can be extended to nonlinear materials and complex geometries via a Finite Element framework. This will enable the capture of experimentally observed activation trends with load. In our work we assumed that mechanophores do not exert tractions on the interface. Relaxing this assumption offers another direction for extending the modeling framework. This approach would involve solving a coupled elasticity problem, where the interface traction law is a function of mechanophore extension and interface opening. Other than the aspect of improving the models, one can also look at post-mechanophore healing stress redistribution in polymer composites and identifying scenarios in which mechanophore healing will be effective and ineffective in damage management. The last portion of this dissertation describes a very fundamental direction, that of capturing the influence of environment on mechanochemical reaction rates. There is a scope for the development of a statistical mechanics theory of mechanochemical reaction rates in solids where one can account for the statistical variations arising from confinement of mechanophores in different parts of the polymeric system. A good tool for the investigation of these systems is the Finite Temperature String (FTS) approach [83, 51, 79] using a representative set of variables capturing the mechanophore reaction. This numerical approach built on MD simulations can be used to study the impact of complex environments on the reaction rate. This dissertation is a beginning towards the mod-

eling of IMACs and it reveals many theoretical and computational aspects that are quintessential to further the understanding of function and experimental realization of IMACs with effective damage management capabilities.

BIBLIOGRAPHY

[1] Amnaya P Awasthi, Dimitris C Lagoudas, and Daniel C Hammerand. Modeling of graphene–polymer interfacial mechanical behavior using molecular dynamics. *Modelling and Simulation in Materials Science and Engineering*, 17(1):015002, 2008.

[2] George I Bell et al. Models for the specific adhesion of cells to cells. *Science*, 200(4342):618–627, 1978.

[3] Luís FA Bernardo, Ana PBM Amaro, Deesy G Pinto, and Sérgio MR Lopes. Modeling and simulation techniques for polymer nanoparticle composites–a review. *Computational Materials Science*, 118:32–46, 2016.

[4] Martin K Beyer. The mechanical strength of a covalent bond calculated by density functional theory. *The Journal of Chemical Physics*, 112(17):7307–7312, 2000.

[5] Nico Bruns, Katarzyna Pustelny, Lisa M Bergeron, Timothy A Whitehead, and Douglas S Clark. Mechanical nanosensor based on fret within a thermosome: Damage-reporting polymeric materials. *Angewandte Chemie International Edition*, 48(31):5666–5669, 2009.

[6] Yulan Chen, AJH Spiering, S Karthikeyan, Gerrit WM Peters, EW Meijer, and Rint P Sijbesma. Mechanically induced chemiluminescence from polymers incorporating a 1, 2-dioxetane unit in the main chain. *Nature Chemistry*, 4(7):559–562, 2012.

[7] Shiwang Cheng, Vera Bocharova, Alex Belianinov, Shaomin Xiong, Alexander M Kisliuk, Suhas Somnath, Adam Prillaman Holt, Olga S Ovchinnikova, Stephen Jesse, Halie Martin, et al. Unraveling the mechanism of

nanoscale mechanical reinforcement in glassy polymer nanocomposites. *Nano letters*, 2016.

[8] Xu Cheng, Karl W Putz, Charles D Wood, and L Catherine Brinson. Characterization of local elastic modulus in confined polymer films via afm indentation. *Macromolecular rapid communications*, 36(4):391–397, 2015.

[9] J Cho, MS Joshi, and CT Sun. Effect of inclusion size on mechanical properties of polymeric composites with micro and nano particles. *Composites Science and Technology*, 66(13):1941–1952, 2006.

[10] Douglas A Davis, Andrew Hamilton, Jinglei Yang, Lee D Cremar, Dara Van Gough, Stephanie L Potisek, Mitchell T Ong, Paul V Braun, Todd J Martínez, Scott R White, et al. Force-induced activation of covalent bonds in mechanoresponsive polymeric materials. *Nature*, 459(7243):68–72, 2009.

[11] Charles E Diesendruck, Brian D Steinberg, Naoto Sugai, Meredith N Silberstein, Nancy R Sottos, Scott R White, Paul V Braun, and Jeffrey S Moore. Proton-coupled mechanochemical transduction: a mechanogenerated acid. *Journal of the American Chemical Society*, 134(30):12446–12449, 2012.

[12] M Elices, GV Guinea, J Gomez, and J Planas. The cohesive zone model: advantages, limitations and challenges. *Engineering fracture mechanics*, 69 (2):137–163, 2002.

[13] Henry Eyring. The activated complex in chemical reactions. *The Journal of Chemical Physics*, 3(2):107–115, 1935.

[14] J Ferrante, JR Smith, and JH Rose. Universal binding energy relations in metallic adhesion. *Tribology Series*, 7:19–30, 1981.

[15] Shao-Yun Fu, Xi-Qiao Feng, Bernd Lauke, and Yiu-Wing Mai. Effects of particle size, particle/matrix interface adhesion and particle loading on mechanical properties of particulate–polymer composites. *Composites Part B: Engineering*, 39(6):933–961, 2008.

[16] Gregory R Gossweiler, Gihan B Hewage, Gerardo Soriano, Qiming Wang, Garrett W Welshofer, Xuanhe Zhao, and Stephen L Craig. Mechanochemical activation of covalent bonds in polymers with full and repeatable macroscopic shape recovery. *ACS Macro Letters*, 3(3):216–219, 2014.

[17] Granta Design Ltd. Ces edupack, 2016. URL `https://www.grantadesign.com/education/`.

[18] Ramon Groote, Robert TM Jakobs, and Rint P Sijbesma. Mechanocatalysis: forcing latent catalysts into action. *Polymer Chemistry*, 4(18):4846–4859, 2013.

[19] Peter Hänggi, Peter Talkner, and Michal Borkovec. Reaction-rate theory: fifty years after Kramers. *Reviews of Modern Physics*, 62(2):251, 1990.

[20] N Aït Hocine, A Hamdi, M Naït Abdelaziz, P Heuillet, and Fahmi Zaïri. Experimental and finite element investigation of void nucleation in rubber-like materials. *International Journal of Solids and Structures*, 48(9):1248–1254, 2011.

[21] Soonsung Hong and Kyung-Suk Kim. Extraction of cohesive-zone laws from elastic far-fields of a cohesive crack tip: a field projection method. *Journal of the Mechanics and Physics of Solids*, 51(7):1267–1286, 2003.

[22] CO Horgan and AM Chan. The pressurized hollow cylinder or disk prob-

lem for functionally graded isotropic linearly elastic materials. *Journal of Elasticity*, 55(1):43–59, 1999.

[23] TH Hsieh, AJ Kinloch, K Masania, AC Taylor, and S Sprenger. The mechanisms and mechanics of the toughening of epoxy polymers modified with silica nanoparticles. *Polymer*, 51(26):6284–6294, 2010.

[24] Yi Hua, Linxia Gu, and Hidehiko Watanabe. Micromechanical analysis of nanoparticle-reinforced dental composites. *International Journal of Engineering Science*, 69:69–76, 2013.

[25] Farzana Hussain, Mehdi Hojjati, Masami Okamoto, and Russell E Gorga. Review article: polymer-matrix nanocomposites, processing, manufacturing, and application: an overview. *Journal of composite materials*, 40(17): 1511–1575, 2006.

[26] Keiichi Imato, Takeshi Kanehara, Tomoyuki Ohishi, Masamichi Nishihara, Hirofumi Yajima, Masayoshi Ito, Atsushi Takahara, and Hideyuki Otsuka. Mechanochromic dynamic covalent elastomers: Quantitative stress evaluation and autonomous recovery. *ACS Macro Letters*, 4(11):1307–1311, 2015.

[27] Robert TM Jakobs and Rint P Sijbesma. Mechanical activation of a latent olefin metathesis catalyst and persistence of its active species in romp. *Organometallics*, 31(6):2476–2481, 2012.

[28] LY Jiang. A cohesive law for carbon nanotube/polymer interface accounting for chemical covalent bonds. *Mathematics and Mechanics of Solids*, 15(7): 718–732, 2010.

[29] LY Jiang, Y Huang, H Jiang, G Ravichandran, H Gao, KC Hwang, and B Liu. A cohesive law for carbon nanotube/polymer interfaces based on

the van der waals force. *Journal of the Mechanics and Physics of Solids*, 54(11): 2436–2452, 2006.

[30] BB Johnsen, AJ Kinloch, RD Mohammed, AC Taylor, and S Sprenger. Toughening mechanisms of nanoparticle-modified epoxy polymers. *Polymer*, 48(2):530–541, 2007.

[31] Hope M Klukovich, Tatiana B Kouznetsova, Zachary S Kean, Jeremy M Lenhardt, and Stephen L Craig. A backbone lever-arm effect enhances polymer mechanochemistry. *Nature chemistry*, 5(2):110–114, 2013.

[32] Takahiro Kosuge, Keiichi Imato, Raita Goseki, and Hideyuki Otsuka. Polymer–inorganic composites with dynamic covalent mechanochromophore. *Macromolecules*, 49(16):5903–5911, 2016.

[33] Michael B Larsen and Andrew J Boydston. Flex-activated mechanophores: using polymer mechanochemistry to direct bond bending activation. *Journal of the American Chemical Society*, 135(22):8189–8192, 2013.

[34] Corissa K Lee, Brett A Beiermann, Meredith N Silberstein, Joanna Wang, Jeffrey S Moore, Nancy R Sottos, and Paul V Braun. Exploiting force sensitive spiropyrans as molecular level probes. *Macromolecules*, 46(10):3746–3752, 2013.

[35] J Lee and AF Yee. Inorganic particle toughening ii: toughening mechanisms of glass bead filled epoxies. *Polymer*, 42(2):589–597, 2001.

[36] AJ Levy. Decohesion at a circular interface. *Studies in Applied Mechanics*, 35: 173–173, 1994.

[37] AJ Levy. The affect of interfacial shear on cavity formation at an elastic inhomogeneity. *Journal of elasticity*, 50(1):49–85, 1998.

[38] Alan J Levy. The debonding of elastic inclusions and inhomogeneities. *Journal of the Mechanics and Physics of Solids*, 39(4):477–505, 1991.

[39] Jun Li, Tomohiro Shiraki, Bin Hu, Roger AE Wright, Bin Zhao, and Jeffrey S Moore. Mechanophore activation at heterointerfaces. *Journal of the American Chemical Society*, 136(45):15925–15928, 2014.

[40] Jun Li, Chikkannagari Nagamani, and Jeffrey S Moore. Polymer mechanochemistry: from destructive to productive. *Accounts of chemical research*, 48(8):2181–2190, 2015.

[41] Jun Li, Bin Hu, Ke Yang, Bin Zhao, and Jeffrey S Moore. Effect of polymer grafting density on mechanophore activation at heterointerfaces. *ACS Macro Letters*, 5:819–822, 2016.

[42] Meng Li, Qi Zhang, and Shiping Zhu. Photo-inactive divinyl spiropyran mechanophore cross-linker for real-time stress sensing. *Polymer*, 99:521–528, 2016.

[43] Y Li and GD Seidel. Multiscale modeling of functionalized interface effects on the effective elastic material properties of cnt–polyethylene nanocomposites. *Computational Materials Science*, 107:216–234, 2015.

[44] Zhong'an Li, Ryan Toivola, Feizhi Ding, Jeffrey Yang, Po-Ni Lai, Tucker Howie, Gary Georgeson, Sei-Hum Jang, Xiaosong Li, Brian D Flinn, et al. Highly sensitive built-in strain sensors for polymer composites: Fluorescence turn-on response through mechanochemical activation. *Advanced Materials*, 28(31):6592–6597, 2016.

[45] JZ Liang and RKY Li. Rubber toughening in polypropylene: a review. *Journal of Applied Polymer Science*, 77(2):409–417, 2000.

[46] Samuel Lörcher, Thomas Winkler, Katarzyna Makyła, Claudiane Ouellet-Plamondon, Ingo Burgert, and Nico Bruns. Mechanical unfolding of a fluorescent protein enables self-reporting of damage in carbon-fibre-reinforced composites. *Journal of Materials Chemistry A*, 2(17):6231–6237, 2014.

[47] Anatolii Isakievich Lure. *Three-dimensional problems of the theory of elasticity*. Interscience Publishers, 1964.

[48] JJ Magda, M Tirrell, and HT Davis. Molecular dynamics of narrow, liquid-filled pores. *The Journal of Chemical Physics*, 83(4):1888–1901, 1985.

[49] Katarzyna Makyła, Christoph Müller, Samuel Lörcher, Thomas Winkler, Martin G Nussbaumer, Michaela Eder, and Nico Bruns. Fluorescent protein senses and reports mechanical damage in glass-fiber-reinforced polymer composites. *Advanced Materials*, 25(19):2701–2706, 2013.

[50] Meenakshi Sundaram Manivannan and Meredith N Silberstein. Computational investigation of shear driven mechanophore activation at interfaces. *Extreme Mechanics Letters*, 2015.

[51] Luca Maragliano and Eric Vanden-Eijnden. On-the-fly string method for minimum free energy paths calculation. *Chemical physics letters*, 446(1):182–190, 2007.

[52] Stephen L Mayo, Barry D Olafson, and William A Goddard. Dreiding: a generic force field for molecular simulations. *Journal of Physical Chemistry*, 94(26):8897–8909, 1990.

[53] Ilyas Mohammed and Kenneth M Liechti. Cohesive zone modeling of crack nucleation at bimaterial corners. *Journal of the Mechanics and Physics of Solids*, 48(4):735–764, 2000.

[54] Justín Murín, Vladimir Kompiš, and Vladimír Kutiš. *Computational modelling and advanced simulations*, volume 24. Springer Science & Business Media, 2010.

[55] Chikkannagari Nagamani, Huiying Liu, and Jeffrey S Moore. Mechanogeneration of acid from oxime sulfonates. *J. Am. Chem. Soc*, 138(8):2540–2543, 2016.

[56] LD Nguyen, KL Baker, and DH Warner. Atomistic predictions of dislocation nucleation with transition state theory. *Physical Review B*, 84(2):024118, 2011.

[57] Elizabeth M Nofen, Jason Wickham, Bonsung Koo, Aditi Chattopadhyay, and Lenore L Dai. Dimeric anthracene-based mechanophore particles for damage precursor detection in reinforced epoxy matrix composites. *Materials Research Express*, 3(3):035701, 2016.

[58] Elizabeth M Nofen, Nicholas Zimmer, Avi Dasgupta, Ryan Gunckel, Bonsung Koo, Aditi Chattopadhyay, and Lenore L Dai. Stress-sensing thermoset polymer networks via grafted cinnamoyl/cyclobutane mechanophore units in epoxy. *Polymer Chemistry*, 7(47):7249–7259, 2016.

[59] GM Odegard, TC Clancy, and TS Gates. Modeling of the mechanical properties of nanoparticle/polymer composites. *Polymer*, 46(2):553–562, 2005.

[60] Mitchell T Ong, Jeff Leiding, Hongli Tao, Aaron M Virshup, and Todd J Martínez. First principles dynamics and minimum energy pathways for mechanochemical ring opening of cyclobutene. *Journal of the American Chemical Society*, 131(18):6377–6379, 2009.

[61] Evgeny Pidko, Ramon Groote, Emiel Hensen, Rint Sijbesma, et al. Dft study on mechanochemical bond breaking in cogef and molecular dynamics simulations. *Procedia Computer Science*, 4:1167–1176, 2011.

[62] Alessio Piermattei, S Karthikeyan, and Rint P Sijbesma. Activating catalysts with mechanical force. *Nature chemistry*, 1(2):133–137, 2009.

[63] Steve Plimpton. Fast parallel algorithms for short-range molecular dynamics. *Journal of computational physics*, 117(1):1–19, 1995.

[64] Andrea Pucci and Giacomo Ruggeri. Mechanochromic polymer blends. *Journal of Materials Chemistry*, 21(23):8282–8291, 2011.

[65] Wolfgang Quapp and Josep Maria Bofill. A contribution to a theory of mechanochemical pathways by means of newton trajectories. *Theoretical Chemistry Accounts*, 135(4):113, 2016.

[66] Wolfgang Quapp and Josep Maria Bofill. Reaction rates in a theory of mechanochemical pathways. *Journal of computational chemistry*, 37(27): 2467–2478, 2016.

[67] Ashley L Black Ramirez, Zachary S Kean, Joshua A Orlicki, Mangesh Champhekar, Sarah M Elsakr, Wendy E Krause, and Stephen L Craig. Mechanochemical strengthening of a synthetic polymer in response to typically destructive shear forces. *Nature chemistry*, 5(9):757–761, 2013.

[68] Jordi Ribas-Arino and Dominik Marx. Covalent mechanochemistry: theoretical concepts and computational tools with applications to molecular nanomechanics. *Chemical Reviews*, 112(10):5412–5487, 2012.

[69] Maxwell J Robb, Tae Ann Kim, Abigail J Halmes, Scott R White, Nancy R Sottos, and Jeffrey S Moore. Regioisomer-specific mechanochromism of

naphthopyran in polymeric materials. *Journal of the American Chemical Society*, 138(38):12328–12331, 2016.

[70] Roger Rothon. *Particulate-filled polymer composites*. iSmithers Rapra Publishing, 2003.

[71] Meredith N Silberstein, Kyoungmin Min, Lee D Cremar, Cassandra M Degen, Todd J Martinez, Narayana R Aluru, Scott R White, and Nancy R Sottos. Modeling mechanophore activation within a crosslinked glassy matrix. *Journal of Applied Physics*, 114(2):023504, 2013.

[72] Meredith N Silberstein, Lee D Cremar, Brett A Beiermann, Sharlotte B Kramer, Todd J Martinez, Scott R White, and Nancy R Sottos. Modeling mechanophore activation within a viscous rubbery network. *Journal of the Mechanics and Physics of Solids*, 63:141–153, 2014.

[73] Mahdi Takaffoli, Teng Zhang, David Parks, and Xuanhe Zhao. Mechanochemically responsive viscoelastic elastomers. *Journal of Applied Mechanics*, 83(7):071007, 2016.

[74] H Tan, Y Huang, C Liu, G Ravichandran, HM Inglis, and PH Geubelle. The uniaxial tension of particulate composite materials with nonlinear interface debonding. *International Journal of Solids and Structures*, 44(6):1809–1822, 2007.

[75] SC Tjong. Structural and mechanical properties of polymer nanocomposites. *Materials Science and Engineering: R: Reports*, 53(3):73–197, 2006.

[76] CP Tsui, CY Tang, and TC Lee. Finite element analysis of polymer composites filled by interphase coated particles. *Journal of Materials Processing Technology*, 117(1):105–110, 2001.

[77] MJ Van den Bosch, PJG Schreurs, and MGD Geers. An improved description of the exponential xu and needleman cohesive zone law for mixed-mode decohesion. *Engineering Fracture Mechanics*, 73(9):1220–1234, 2006.

[78] Eric Vanden-Eijnden and Fabio A Tal. Transition state theory: Variational formulation, dynamical corrections, and error estimates. *The Journal of chemical physics*, 123(18):184103, 2005.

[79] Eric Vanden-Eijnden and Maddalena Venturoli. Revisiting the finite temperature string method for the calculation of reaction tubes and free energies. *The Journal of chemical physics*, 130(19):05B605, 2009.

[80] F Verstraeten, Robert Göstl, and RP Sijbesma. Stress-induced colouration and crosslinking of polymeric materials by mechanochemical formation of triphenylimidazolyl radicals. *Chemical Communications*, 52(55):8608–8611, 2016.

[81] Qiming Wang, Gregory R Gossweiler, Stephen L Craig, and Xuanhe Zhao. Mechanics of mechanochemically responsive elastomers. *Journal of the Mechanics and Physics of Solids*, 82:320–344, 2015.

[82] Zhijian Wang, Zhiyong Ma, Yao Wang, Zejun Xu, Yiyang Luo, Yen Wei, and Xinru Jia. A novel mechanochromic and photochromic polymer film: When rhodamine joins polyurethane. *Advanced Materials*, 27(41):6469–6474, 2015.

[83] E Weinan, Weiqing Ren, and Eric Vanden-Eijnden. Finite temperature string method for the study of rare events. *J. Phys. Chem. B*, 109(14):6688–6693, 2005.

[84] Bernd Wetzel, Frank Haupert, and Ming Qiu Zhang. Epoxy nanocomposites with high mechanical and tribological performance. *Composites Science and Technology*, 63(14):2055–2067, 2003.

[85] Jeremiah W Woodcock, Ryan Beams, Chelsea S Davis, Ning Chen, Stephan J Stranick, Darshil U Shah, Fritz Vollrath, and Jeffrey W Gilman. Observation of interfacial damage in a silk-epoxy composite, using a simple mechanoresponsive fluorescent probe. *Advanced Materials Interfaces*, 4 (10), 2017.

[86] Yueping Ye, Haibin Chen, Jingshen Wu, and Lin Ye. High impact strength epoxy nanocomposites with natural nanotubes. *Polymer*, 48(21):6426–6433, 2007.

[87] Robert J Young and Peter A Lovell. *Introduction to polymers*. CRC press, 2011.

[88] Ning Yu and Andreas A Polycarpou. Adhesive contact based on the Lennard–Jones potential: a correction to the value of the equilibrium distance as used in the potential. *Journal of Colloid and Interface Science*, 278(2): 428–435, 2004.

[89] Huan Zhang, Arthur K Scholz, Jordan de Crevoisier, Fabien Vion-Loisel, Gilles Besnard, Alexander Hexemer, Hugh R Brown, Edward J Kramer, and Costantino Creton. Nanocavitation in carbon black filled styrene–butadiene rubber under tension detected by real time small angle x-ray scattering. *Macromolecules*, 45(3):1529–1543, 2012.

[90] Huan Zhang, Fei Gao, Xiaodong Cao, Yanqun Li, Yuanze Xu, Wengui Weng, and Roman Boulatov. Mechanochromism and mechanical-force-

triggered cross-linking from a single reactive moiety incorporated into polymer chains. *Angewandte Chemie*, 128(9):3092–3096, 2016.

[91] Yancheng Zhang, Junhua Zhao, Yue Jia, Tarek Mabrouki, Yadong Gong, Ning Wei, and Timon Rabczuk. An analytical solution on interface debonding for large diameter carbon nanotube-reinforced composite with functionally graded variation interphase. *Composite Structures*, 104:261–269, 2013.